

# Experimental Characterization and Physical Modeling of Resolution Limits in Proximity Printing X-Ray Lithography

by

**Kathleen Regina Early**

B.F.A. Cooper Union (1973)

B.E.E. The City College of the City University of New York (1985)

S.M. Massachusetts Institute of Technology (1987)

*submitted to the*

**Department of Electrical Engineering and Computer Science**

*in partial fulfillment  
of the requirements for the degree of*

**Doctor of Philosophy  
in Electrical Engineering and Computer Science**

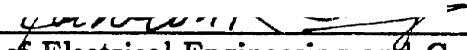
*at the*

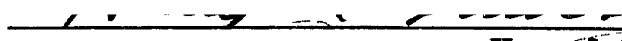
**Massachusetts Institute of Technology**

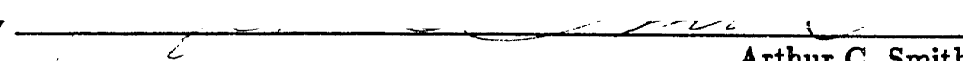
**22 May 1991**

©Massachusetts Institute of Technology 1991

All rights reserved.

Signature of Author   
Department of Electrical Engineering and Computer Science  
22 May 1991

Certified by   
Henry I. Smith, Thesis Supervisor

Accepted by   
Arthur C. Smith  
Chairman, Departmental Committee on Graduate Students

1

MASSACHUSETTS INSTITUTE  
OF TECHNOLOGY

JUL 24 1991

LIBRARIES  
ARCHIVES

# **Experimental Characterization and Physical Modeling of Resolution Limits in Proximity Printing X-Ray Lithography**

**Kathleen Regina Early**

**Submitted to the Department of Electrical Engineering and Computer Science  
on 22 May 1991 in partial fulfillment of the requirements for the Degree of  
Doctor of Philosophy in Electrical Engineering and Computer Science**

## **Abstract**

Image resolution in x-ray proximity printing is influenced by diffraction, photo and Auger electron range, and in some instances, shot noise. In this thesis each of these issues is addressed. For the first time, 30 nm-wide lines were replicated using  $Al_K$  radiation ( $\lambda = 0.8$  nm). No degradation in linewidth was seen for these lines as compared with lines imaged from the same mask with either  $C_K$  ( $\lambda = 4.5$  nm) or  $Cu_L$  ( $\lambda = 1.3$  nm) x-rays, indicating that, contrary to previous assumptions, photoelectron range is not an obstacle to resolution in the 50 nm linewidth regime for wavelengths as short as 0.8 nm. For reasons of process latitude and ease of mask fabrication slightly longer wavelengths are preferred. A chemically amplified resist, Ray-PF, was used to pattern 100 nm-wide lines in a 1  $\mu\text{m}$ -thick film with a dose of 5  $\text{mJ}/\text{cm}^2$ ; this dose corresponds to  $\sim 100$  photons/pixel where the pixel height is 100 nm and the pixel area is the linewidth squared. Based on image quality, 100 photon/pixel is taken as the shot-noise-limited minimum acceptable x-ray dose; higher doses are recommended for industrial processes. The question of maximum acceptable mask-to-substrate gap was explored by shadow casting a mask pattern onto a sloped wall. The pattern consisted of isolated lines, spaces, and gratings of nominal 0.2, 0.3, 0.4 and 0.5  $\mu\text{m}$  width. The smallest features, 0.17  $\mu\text{m}$ -wide spaces printed to gaps as large as 35  $\mu\text{m}$  with significant image degradation becoming apparent at  $\sim 18$   $\mu\text{m}$ . Exposures were compared to theoretical linewidth-gap plots, each of which contained a family of equi-irradiance contours of diffracted linewidth as a function of gap. Correlation was seen between image degradation and divergence of the equi-irradiance contours. A slow widening of linewidth with gap was seen; but, linewidth oscillations with changing gap, predicted by theory, were not detected in the exposures.

**Thesis Supervisor: Henry I. Smith**

**Title: Professor of Electrical Engineering and Computer Science**

*To my Parents*

# Acknowledgements

To do true justice to all those who have helped me along the way to getting my PhD would require a document as long as the thesis itself. I will begin by thanking my advisor, Professor Henry I. Smith, for his guidance, encouragement, and support. I've enjoyed working with him and learning from him. It has been a great pleasure being part of his research group, working in the Submicron Structures Laboratory (SSL), and experiencing the esprit de corps of the SSL mafia.

It is not unusual for a researcher to pick up much about the correct approach, or mind-set, for doing experiments from watching a pro at work. For me, Dr. Mark Schattenburg is that pro, the quintessential experimenter: Constantly looking for the next incremental improvement in technique, forever curious about failed experiments as well as successful ones, endlessly attentive to detail, and always generous in sharing credit. The SSL is such a lively place largely because of innovations introduced by Mark.

The fabrication of the micro-gap masks used in this thesis was a group effort involving many people besides myself: Mark Schattenburg created the original design; Yao-Ching Ku and the UROP's under him, Lisa Su and Flora Tsai, spent innumerable hours etching nitride and silicon to provide the lab with mask blanks; and Mark Shepard worked diligently on pattern writing with the focused ion beam (FIB). I am grateful to John Melngailis for many useful discussions about the FIB and to Chris Musil for his help with the doctored MAGIC software that was used for mask layout.

Charlie Doherty, at Lincoln Lab, did several needed oxidations and nitride depositions. Vince McNeil generously shared his knowledge of electrochemical etching, and Lisa Su worked with me on the membrane etching. Dan Olster was invaluable in implementing several *Numerical Recipes* routines and in generating interactive software for the diffraction calculations. I especially enjoyed working with Gee Rittenhouse on etching thin vertical walls in silicon, and I wish him every success with his superconducting device efforts.

The value of our lab manager, Jim Carter, can be estimated by how often it has been suggested that he should be cloned; the lab runs smoothly and safely because of his efforts, and many experiments would not get done were it not for his attentiveness to the needs of the lab users. I've really enjoyed working with him during my time at MIT. I would also like to thank Margaret Hamnett for teaching me so much about lab procedures when I first joined the group. The excellent SSL technicians, Jeanne Porter, Tim McClure, and Mark Mondol all

contributed to my thesis by doing evaporations, making sure the needed supplies were always in place, and keeping equipment in good repair. Thanks are due to Donna Martinez for her effective and cheerful administration. I am grateful too to Marilyn Pierce in the graduate office who is a warm and empathetic shepardess, nurturing her flock of EECS grad students.

So much of what one learns as a graduate student comes from those with whom one rubs shoulders. I count myself lucky to have worked with, and have been helped, in innumerable ways both large and small, by Bill Chu, Yao-Ching Ku, Alberto Moel, and Tony Yen. To them and to the all the students I have had the opportunity to know and work with during my time at MIT, both in the SSL and within the larger Microsystems Technology Laboratory (MTL) community, I extend my heartfelt thanks.

It is a pleasure to thank Professor Art Smith for being the very special person that he is, for listening and advising so well, for being a friend, and for including me at his elastic Sunday night supper table. I especially wish to thank Stefi Wise and Gene Tulchin for their friendship, hospitality, and encouragement, which has meant so much to me, as I followed my convoluted path from Cooper Union to MIT. I am indebted to my cousin, Andy Eccles, for sharing his apartment with me when I first came to MIT; and also to Lisa Kamishir and Wayne Koch, as well as Fran Davis and Mark Schattenburg, who made me welcome in their homes when I needed a place to stay. I appreciate the late night talk and comradeship of my housemates, Kate Piggot and Ken Wissoker, which provided a refreshing change from the grad school environment. Many thanks too to my dear friend, Barbara Yanni, for her visits, her patience, and her reminders that grad school only seems like forever. I would like to thank Joe Haritonidis for his love and support during the years we were together, and I wish him well in his new life at Ohio State. And last, but far from least, I thank my parents, Mary Agnes and Jim, and my siblings, Marybeth, Joan, Rhoda, Maureen, Rosemary, Jim, and Margot, for their love and affection.

This work was supported by the Joint Services Electronics Program (Contract DAAL03-89-C-0001) and the National Science Foundation (Grant ECS-8709806).

# Contents

<b>1</b>	<b>Introduction</b>	<b>15</b>
<b>2</b>	<b>Photoelectron Range and Resolution</b>	<b>22</b>
2.1	Previous Studies . . . . .	24
2.2	Experimental . . . . .	28
2.3	Results . . . . .	31
2.4	Discussion . . . . .	31
<b>3</b>	<b>X-Ray Resists</b>	<b>38</b>
3.1	Polymethyl Methacrylate Resist . . . . .	38
3.2	Chemically Amplified Resists . . . . .	41
<b>4</b>	<b>Shot Noise</b>	<b>54</b>
<b>5</b>	<b>Diffraction: Theory and Simulations</b>	<b>61</b>
5.1	The Angular Spectrum of Plane Waves . . . . .	63
5.2	Spatial Incoherence . . . . .	66
5.3	Simulations . . . . .	70
<b>6</b>	<b>Diffraction: Experimental</b>	<b>95</b>
6.1	Mask Fabrication . . . . .	95
6.2	Experimental Set-Up . . . . .	98
6.2.1	Etched Pits . . . . .	99
6.2.2	V-Grooves . . . . .	100
6.3	Results and Discussion . . . . .	102
<b>7</b>	<b>Summary and Future Work</b>	<b>134</b>

<b>A Ray-PF and Ray-PN Processing</b>	<b>138</b>
<b>B Polyimide Maskmaking</b>	<b>145</b>
<b>C KOH Etching</b>	<b>157</b>
C.1 Etching of (100) Silicon . . . . .	158
C.1.1 Electrochemical Etch Stop Experiment . . . . .	158
C.1.2 Etch Pits for Diffraction Experiment . . . . .	162
C.2 Anisotropic Etching of (110) Silicon . . . . .	163

# List of Figures

1.1	PPXRL configuration: An x-ray mask is held either in contact with or a small distance (4 to 100 $\mu$ m) from a resist-coated wafer and the assembly is exposed to x-rays. Essentially, the absorber pattern present on the semi-transparent x-ray mask membrane is shadow-cast onto the resist. When a gap is used between mask and substrate, each is protected from damage caused by the other or by particles that may come between the two. . . . .	17
2.1	At left a photon is absorbed by a carbon atom which emits a photoelectron; an outershell electron fills the vacancy and a C <sub>K</sub> photon is emitted. The cross section for the photon emission (fluorescence) from a low Z material such as carbon is nearly zero thus making this process unlikely. At right, through the process of internal conversion, the energy given up by the electron filling the vacancy is imparted to another electron allowing it to be emitted as an Auger. . . . .	23
2.2	Schematic depiction of x-ray photon absorption in resist in the vicinity of a single Au absorber line. The Au line is part of an absorber pattern on an x-ray mask that is in contact with the resist coated substrate. Photoelectrons have sufficient range to travel beneath the absorber. For many years it was thought that this would cause a shrinkage in linewidth shown here as an undercut in the resist profile. . . . .	24
2.3	Normalized energy distribution for absorbed (a) Cu <sub>L</sub> and (b) Al <sub>K</sub> x-rays from an infinitely thin line source. From Reference [33] . . . . .	27
2.4	Experimental set-up: The absorber lines are evaporated on the sidewall of the polyimide grating mask. For exposures with Cu <sub>L</sub> and Al <sub>K</sub> x-rays a 1 $\mu$ m -thick silicon nitride membrane (not shown) was placed between the mask and the x-ray source to filter out low energy electrons. . . . .	29
2.5	X-ray attenuation curves for Au, SiN, and polyimide. . . . .	30
2.6	Replication in PMMA of a 30nm-wide Au absorber line with (a) C <sub>K</sub> ( $\lambda = 4.5\text{nm}$ ), (b) Cu <sub>L</sub> ( $\lambda = 1.3\text{nm}$ ), (a) Al <sub>K</sub> ( $\lambda = 0.83\text{nm}$ ) x-rays. . . . .	34



2.7	Convolution of intensity for a 30-nm wide slit and a 30 nm-wide with the absorbed energy density function [33] for $Al_K$ x-rays (a) from an infinite contrast mask (b) from a 10 dB attenuating mask.	36
2.8	Convolution of intensity for a 30-nm wide slit and a 30 nm-wide with the absorbed energy density function [33] for $Cu_L$ x-rays (a) from an infinite contrast mask (b) from a 10 dB attenuating mask.	37
3.1	At left a photon is absorbed in the resist generating a number of acid molecules. At right a single acid molecule act as a catalyst at many cites causing chemical amplification. The volume associated with its influence is unknown. . . . .	42
3.2	PMMA [38] resist, 950K molecular weight, $0.25\mu\text{m}$ -thick, prebaked at $180^\circ\text{C}$ for 30 minutes, and exposed using the Hampshire instruments 10P x-ray plasma source with a $5\mu\text{m}$ mask-to-substrate gap. Dose to the resist was $200\text{mJ}/\text{cm}^2$ ; development time was one minute in 40:60 MIBK:IPA. . . . .	44
3.3	Ray-PN resist, $0.25\mu\text{m}$ -thick, softbaked at $80^\circ\text{C}$ for 30 minutes, and dosed with $18\text{mJ}/\text{cm}^2$ of 1.3nm x-rays ( $Cu_L$ ) at a $5\mu\text{m}$ mask-to-substrate gap. The wafer received a five minute post-exposure-bake at $105^\circ\text{C}$ on a vacuum chucked hotplate. Development time was five minutes in 1:1 AZ Developer and DI $H_2O$ . . . . .	46
3.4	Ray-PF resist, $0.4\mu\text{m}$ -thick, softbaked at $80^\circ\text{C}$ for 30 minutes, and exposed with $7.5\text{mJ}/\text{cm}^2$ of 1.3nm x-rays at a $5\mu\text{m}$ mask-to-substrate gap. The postexposure hold time was one hour, and was followed by a one minute $60^\circ\text{C}$ hotplate bake. Development time was two minutes in 1:1 AZ Developer and DI $H_2O$ . . . . .	48
3.5	Ray-PF resist, $1\mu\text{m}$ -thick, softbaked for one minute on a vacuum chucked hotplate at $120^\circ\text{C}$ , and exposed with $5\text{mJ}/\text{cm}^2$ of 1.3nm x-rays at a $5\mu\text{m}$ mask-to-substrate gap. The postexposure hold time was 1.5 hours, and was followed by a one minute $60^\circ\text{C}$ hotplate bake. Development time was 2.5 minutes in 1:1 AZ Developer and DI $H_2O$ . . . . .	50
3.6	Examples of surface induction layer effect in Ray-PN. This effect is usually only seen between closely spaced small features. . . . .	52
4.1	A single MR pixel of resist has height $h$ and surface area $(LW)^2$ , where $LW$ is the minimum resolvable linewidth. . . . .	55
4.2	An $\epsilon^2$ pixel with height $h$ and area $\epsilon^2$ where $\epsilon = LW/10$ . . . . .	57

4.3	The mean number of photons per pixel, $\bar{N}(x)$ , is proportional to intensity and varies with position as shown. The development band, $\delta N$ , is centered about $\bar{N}_m$ , the mean number of photons required to develop a pixel. For purpose of analysis, $\bar{N}_m$ is assumed to lie midway between $\bar{N}_{max}$ and $\bar{N}_{min}$ [65,66] . . . . .	58
5.1	Depiction of diffraction situation for x-ray proximity printing: $\Sigma_m$ is the mask plane; $\Sigma_{ss}$ is the image plane. . . . .	64
5.2	Illustration of the pathlength difference for two rays traced from a point on the extended source to a point on the image plane. For the experiment modeled here, $D = 50$ cm, $d = 1$ mm, and $5 \leq G \leq 100$ $\mu\text{m}$ . . . . .	67
5.3	Diffraction patterns for a 1 $\mu\text{m}$ -period grating with (a) vertical absorber walls and (b) 20° sloped walls are compared with an x-ray exposure in PMMA made using a mask with sloped wall absorber. Cross section and aerial views of the exposure are seen in (c) and (d). 75	75
5.4	Diffraction patterns for a 1 $\mu\text{m}$ -period grating with: (a) vertical absorber walls with a 2 mm source;(b) vertical absorber walls with a 3 mm source; (c) 20° sloped walls with a 2 mm source; (d) 20° sloped walls with a 3 mm source. . . . .	77
5.5	The convolution of a gaussian with FWHM = 60 $\mu\text{m}$ with a 90 $\mu\text{m}$ -wide slit. The data points are for the exposures listed in Table 5.2. The corresponding source has FWHM=2 mm. . . . .	78
5.6	SEM's (a) to (c) of nominal 0.2 $\mu\text{m}$ mask features. The actual dimensions are 0.17 $\mu\text{m}$ spaces and 0.23 $\mu\text{m}$ lines. The SEM in (d) is a cross section of the membrane that was used in diffraction experiments. . . . .	79
5.7	Equi-irradiance curves of the diffracted image of a 0.17 $\mu\text{m}$ -wide slit for gaps ranging from 5 to 50 $\mu\text{m}$ . The equi-irradiance curves vary from 0.15 (bottom curve) to 0.85 (top curve) in 0.05 increments. The absorber thickness is 0.25 $\mu\text{m}$ in (a) and 0.5 $\mu\text{m}$ in (b). . . . .	81
5.8	Equi-irradiance curves of the diffracted image of a 0.23 $\mu\text{m}$ -wide line for gaps ranging from 5 to 50 $\mu\text{m}$ . The equi-irradiance curves vary from 0.15 (top curve) to 0.85 (bottom curve) in 0.05 increments. The absorber thickness is 0.25 $\mu\text{m}$ in (a) and 0.5 $\mu\text{m}$ in (b). . . . .	82
5.9	Equi-irradiance curves of the diffracted image of a 0.4 $\mu\text{m}$ -period grating, with 0.17 $\mu\text{m}$ -wide spaces, for gaps ranging from 5 to 50 $\mu\text{m}$ . The equi-irradiance curves vary from 0.15 (bottom curve) to 0.85 (top curve) in 0.05 increments. The absorber thickness is 0.25 $\mu\text{m}$ in (a) and 0.5 $\mu\text{m}$ in (b). . . . .	83

5.10	Equi-irradiance curves of the diffracted image of a 0.25 $\mu\text{m}$ -wide slit for gaps ranging from 5 to 100 $\mu\text{m}$ . The equi-irradiance curves vary from 0.15 (bottom curve) to 0.85 (top curve) in 0.05 increments. The absorber thickness is 0.25 $\mu\text{m}$ in (a) and 0.5 $\mu\text{m}$ in (b). . . . .	84
5.11	Equi-irradiance curves of the diffracted image of a 0.35 $\mu\text{m}$ -wide line for gaps ranging from 5 to 100 $\mu\text{m}$ . The equi-irradiance curves vary from 0.15 (top curve) to 0.85 (bottom curve) in 0.05 increments. The absorber thickness is 0.25 $\mu\text{m}$ in (a) and 0.5 $\mu\text{m}$ in (b). . . . .	85
5.12	Equi-irradiance curves of the diffracted image of a 0.6 $\mu\text{m}$ -period grating, with 0.25 $\mu\text{m}$ -wide spaces, for gaps ranging from 5 to 100 $\mu\text{m}$ . The equi-irradiance curves vary from 0.15 (bottom curve) to 0.85 (top curve) in 0.05 increments. The absorber thickness is 0.25 $\mu\text{m}$ in (a) and 0.5 $\mu\text{m}$ in (b). . . . .	86
5.13	Equi-irradiance curves of the diffracted image of a 0.38 $\mu\text{m}$ -wide slit for gaps ranging from 5 to 100 $\mu\text{m}$ . The equi-irradiance curves vary from 0.15 (bottom curve) to 0.85 (top curve) in 0.05 increments. The absorber thickness is 0.25 $\mu\text{m}$ in (a) and 0.5 $\mu\text{m}$ in (b). . . . .	87
5.14	Equi-irradiance curves of the diffracted image of a 0.42 $\mu\text{m}$ -wide line for gaps ranging from 5 to 100 $\mu\text{m}$ . The equi-irradiance curves vary from 0.15 (top curve) to 0.85 (bottom curve) in 0.05 increments. The absorber thickness is 0.25 $\mu\text{m}$ in (a) and 0.5 $\mu\text{m}$ in (b). . . . .	88
5.15	Equi-irradiance curves of the diffracted image of a 0.8 $\mu\text{m}$ -period grating, with 0.38 $\mu\text{m}$ -wide spaces, for gaps ranging from 5 to 100 $\mu\text{m}$ . The equi-irradiance curves vary from 0.15 (bottom curve) to 0.85 (top curve) in 0.05 increments. The absorber thickness is 0.25 $\mu\text{m}$ in (a) and 0.5 $\mu\text{m}$ in (b). . . . .	89
5.16	Equi-irradiance curves of the diffracted image of a 0.48 $\mu\text{m}$ -wide slit for gaps ranging from 5 to 100 $\mu\text{m}$ . The equi-irradiance curves vary from 0.15 (bottom curve) to 0.85 (top curve) in 0.05 increments. The absorber thickness is 0.25 $\mu\text{m}$ in (a) and 0.5 $\mu\text{m}$ in (b). . . . .	90
5.17	Equi-irradiance curves of the diffracted image of a 0.52 $\mu\text{m}$ -wide line for gaps ranging from 5 to 100 $\mu\text{m}$ . The equi-irradiance curves vary from 0.15 (top curve) to 0.85 (bottom curve) in 0.05 increments. The absorber thickness is 0.25 $\mu\text{m}$ in (a) and 0.5 $\mu\text{m}$ in (b). . . . .	91
5.18	Equi-irradiance curves of the diffracted image of a 1.0 $\mu\text{m}$ -period grating, with 0.48 $\mu\text{m}$ -wide spaces, for gaps ranging from 5 to 100 $\mu\text{m}$ . The equi-irradiance curves vary from 0.15 (bottom curve) to 0.85 (top curve) in 0.05 increments. The absorber thickness is 0.25 $\mu\text{m}$ in (a) and 0.5 $\mu\text{m}$ in (b). . . . .	92
5.19	Diffraction patterns for a 0.4 $\mu\text{m}$ -period grating with 0.17 $\mu\text{m}$ -wide spaces with 0.5 $\mu\text{m}$ -thick Au absorber. . . . .	93

5.20	Diffraction patterns for a 0.4 $\mu\text{m}$ -period grating with 0.17 $\mu\text{m}$ -wide spaces with 0.25 $\mu\text{m}$ -thick Au absorber. . . . .	94
6.1	The six studs of the microgap mask rest on the resist coated wafer which sits on an optically-flat pin-chuck. An aluminum spacer sits on top of the mask. The assembly is clamped together with two spring arms. During exposure, the mask assemblage is inverted to face the x-ray source which will be below it. . . . .	96
6.2	Mask Fabrication Sequence . . . . .	106
6.3	Mask patterns used in the diffraction experiments. . . . .	107
6.4	The mask patterns shown here were used in the resist characterization work presented in Chapter 3. . . . .	109
6.5	Gap-extending methods for diffraction experiments. In (a), a pit is etched in the wafer. In (b), v-grooves, etched into the substrate, provide sloped walls onto which the mask patterns are shadowcast. . . . .	111
6.6	(a) Microgap measurement technique; (b) plot shows the number of fringes expected for a given gap for different membrane materials and thicknesses, from reference [27]. . . . .	112
6.7	Ray-PF resist exposed at a 25 $\mu\text{m}$ gap. . . . .	113
6.8	In v-groove experiment, gaps were calibrated by means of a grating which has a 1 $\mu\text{m}$ -period in the mask plane. The gap at any measurement point is $G = (\sqrt{2N} + 5)\mu\text{m}$ . . . . .	115
6.9	Measurement grating exposure in Ray-PN resist: (a) The grating is resolved over the full depth of $\sim 100 \mu\text{m}$ ; (b) One wall of the v-groove is only thinly coated with resist near the top. Compare this to the opposite wall shown in (b) of Figure 6.10. . . . .	116
6.10	SEMs of the measurement grating in Ray-PN: (a) At the bottom of the groove; and (b), at the top of the groove. . . . .	118
6.11	Mask pattern imaged, in Ray-PN resist, on a sloped wall. Dose = 24 $\text{mJ}/\text{cm}^2$ ; $5 \leq G \leq 100 \mu\text{m}$ . Nominal linewidths are: (a) 0.2; (b) 0.3; (c) 0.4; and (d) 0.5 $\mu\text{m}$ . . . . .	120
6.12	Mask pattern imaged, in Ray-PN resist, on a sloped wall. Dose = 26.4 $\text{mJ}/\text{cm}^2$ ; $5 \leq G \leq 100 \mu\text{m}$ . Nominal linewidths are: (a) 0.2; (b) 0.3; (c) 0.4; and (d) 0.5 $\mu\text{m}$ . . . . .	122
6.13	Images, on v-groove wall, of: 0.4 $\mu\text{m}$ -period grating with 0.17 $\mu\text{m}$ -wide spaces; a 0.17 $\mu\text{m}$ -wide space; and a 0.23 $\mu\text{m}$ -wide line. $5 \leq G \leq 22 \mu\text{m}$ . Dose = 24 $\text{mJ}/\text{cm}^2$ . . . . .	124
6.14	Images, on v-groove wall, of: 0.4 $\mu\text{m}$ -period grating with 0.17 $\mu\text{m}$ -wide spaces; a 0.17 $\mu\text{m}$ -wide space; and a 0.23 $\mu\text{m}$ -wide line. $22 \leq G \leq 42 \mu\text{m}$ . Dose = 24 $\text{mJ}/\text{cm}^2$ . . . . .	126

6.15	Images, on v-groove wall, of: 0.4 $\mu\text{m}$ -period grating with 0.17 $\mu\text{m}$ -wide spaces; a 0.17 $\mu\text{m}$ -wide space; and a 0.23 $\mu\text{m}$ -wide line. $5 \leq G \leq 20 \mu\text{m}$ . Dose = 26.4 $\text{mJ}/\text{cm}^2$ . . . . .	128
6.16	Images, on v-groove wall, of: 0.4 $\mu\text{m}$ -period grating with 0.17 $\mu\text{m}$ -wide spaces; a 0.17 $\mu\text{m}$ -wide space; and a 0.23 $\mu\text{m}$ -wide line. $20 \leq G \leq 37 \mu\text{m}$ . Dose = 26.4 $\text{mJ}/\text{cm}^2$ . . . . .	130
6.17	Calculated equi-irradiance contours and measured image widths for the 0.17 $\mu\text{m}$ -wide slit. Closed and open circles are for the 24 and 26.4 $\text{mJ}/\text{cm}^2$ doses, respectively. . . . .	132
6.18	Calculated equi-irradiance contours and measured image widths for the 0.23 $\mu\text{m}$ -wide line. Closed and open circles are for the 24 and 26.4 $\text{mJ}/\text{cm}^2$ doses, respectively. . . . .	133
6.19	Calculated equi-irradiance contours and measured image widths for the 0.4 $\mu\text{m}$ -period grating with 0.17 $\mu\text{m}$ -wide spaces. Closed and open circles are for the 24 and 26.4 $\text{mJ}/\text{cm}^2$ doses, respectively. . .	133
A.1	Process flow for Ray-PF and Ray-PN. In the Ray-PF diagram, branch A corresponds to the case of short vacuum time where the hold time can be set to zero; branch B indicates that the PEB is not strictly required for Ray-PF provided the hold time is sufficiently long (at least on hour). For Ray-PN no hold time is required the PEB is mandatory because the acid catalyzed reaction does not go forward at room temperature. . . . .	139
A.2	Spin curves for Ray-PF. Thicknesses were measured after solvent drive-off bake. Bottom curve is for resist diluted 1:1 with Type A Thinner. . . . .	143
A.3	Spin curves for Ray-PN. Thicknesses were measured after solvent drive-off bake. Bottom curve is for resist diluted 1:1 with Type A Thinner. . . . .	144
B.1	Mask fabrication steps. . . . .	146
B.2	Three stages in fabrication of polyimide mask making: At left, a (110), KOH etched wafer with masking nitride still in place. At center, the same sample after removal of the nitride. Note smoothness of the vertical sidewalls. At right, polyimide mask membrane made from silicon mold. . . . .	148
B.3	PVC pipe with mask wafer: The membrane side faces the pipe. Black wax is painted to completely coat the edges of the wafer, extending about 1/4 inch in from the edge and about 3/8 inch up the side of the pipe. The wax creates a leak-tight seal that will prevent the etchant from entering the pipe. . . . .	151
B.4	Membrane etching is carried out under a well ventilated hood. . .	152

B.5	The PVC pipe hangs over the etchant from a 6 inch cotton-tipped applicator. The wafer should just skim the surface of the etchant. The pipe is tilted slightly to allow bubbles to escape as etching evolves. A wafer carrier cover is place over the pipe to prevent fumes from filling the pipe. . . . .	153
B.6	Mask-frame-to-membrane bonding: The pipe is place wafer side down in a teflon wafer carrier. The epoxy-coated mask frame is lightly held to the bottle/slide assembly by double sided masking tape. A third arm is used to carefully lower the frame onto the membrane. The bottle serves as a weight to press the frame against the membrane while the epoxy cures. . . . .	155
C.1	(100) Silicon etched in 40% KOH, 60% DI at 60°: (a) was etched from the front and (b) from the back surface of the same wafer; (c) was etched from the front of the wafer with the addition of IPA to saturate the solution. . . . .	163
C.2	An electrochemically etched membrane fabricated from a doubleside polished wafer: (a) a Fizeau interferogram of the membrane; (b) a Linnik interferogram of the etched membrane; (c)the membrane has begun to passivate first in the bubble areas; (d) the membrane is completely passivated. . . . .	165
C.3	(a) A Fizeau interferogram of a 20 $\mu\text{m}$ -deep pit etched in a 4-inch (100) wafer; most of the pit lies within a single fringe. (b) A Linnik interferogram indicates that the etched surface is smooth to within 100nm. . . . .	167
C.4	Misalignment to the crystallographic plane causes jogs in the (111) wall. . . . .	172
C.5	Schematic illustration of triangular walls, or membranes, that can be formed by utilizing the nonperpendicular (111) planes as etch barriers. . . . .	173
C.6	First level patterning of a resonant tunneling device [91,92]. The "gate" of the device is a wall of silicon defined by vertical (111) planes. . . . .	174
C.7	A triangular membrane, thinner than 10 nm, that was etched in (110) silicon. The etch has terminated everywhere on {111} planes. . . . .	176

# Chapter 1

## Introduction

The invention of the bipolar transistor in 1948 [1] precipitated the computer age. Computing machines have been studied for centuries; the transistor was the technological breakthrough that made implementation possible on a grand scale. Mass production of computers became feasible with the introduction of the integrated circuit (IC) in 1958 and the planar process in 1959 [2]. The industry wide drive is today, as it has been for the past three decades, toward packing more and more computing capability on a single chip of silicon by shrinking transistor size and increasing transistor population density. This trend is quantified in Table 1.1. A key step used repeatedly in manufacturing very large scale integrated circuit (VLSI) chips is photolithographic patterning of silicon wafers. In the IC industry infancy, this was done by proximity printing with chromium coated glass masks and wavelengths in the visible and near UV spectrum. As device dimensions shrank, optical projection using a reduction camera gained ascendancy over proximity printing leading to reduced defects and increased alignment accuracy [4].

It had long been anticipated that the resolution limit of optical projection would be reached before any fundamental limits on transistor dimensions. In 1972, it was proposed and demonstrated that, when reached, the resolution barrier could be overcome by a return to proximity printing with a reduction in wavelength to

Memory Storage	Minimum Linewidth	Production Year
1Mbit	1.0 – 1.1 $\mu\text{m}$	1984
4Mbit	0.70 – 0.8 $\mu\text{m}$	1987
16Mbit	0.50 – 0.6 $\mu\text{m}$	1990
64Mbit	0.35 – 0.4 $\mu\text{m}$	1996
256Mbit	0.25 – 0.3 $\mu\text{m}$	?
1Gbit	0.18 – 0.22 $\mu\text{m}$	?

Table 1.1: Historical and projected figures for DRAM storage capacity, minimum device linewidth, and marketplace entry year[3].

the soft x-ray regime ( $0.7 \leq \lambda \leq 5\text{nm}$ ) [5]. In this technology, the glass mask is replaced by a thin membrane of silicon, silicon carbide, diamond or silicon nitride and the chromium mask pattern is replaced with gold or tungsten absorber less than  $0.5\mu\text{m}$ -thick as depicted in Figure 1. With an x-ray mask in contact with the substrate, lines as fine as 30 are easily replicated [6,7]; a record of 17.5nm lines and spaces has been reported [8].

Originally it was thought that proximity printing x-ray lithography (PPXRL) would take over from projection optics when linewidths shrank below  $\sim 0.7\mu\text{m}$ . The introduction of shorter wavelength light sources and the prospect of losing market share to x-ray lithography have spurred the optics industry to push their patterning capability below  $0.4\mu\text{m}$ . A number of research and development  $5\times$  reduction optical systems utilizing KrF excimer laser sources have demonstrated 0.25 to  $0.35\mu\text{m}$  resolution over at least a portion of their exposure fields [9-12]. These multiple element systems require high quality quartz lenses that accept only a narrow bandwidth ( $\lambda = 248 \pm 0.0015\text{nm}$ ) and have price tags running to several million dollars. Recently, sub- $0.2\mu\text{m}$ -wide lines have been imaged using a phase-shifting masks and a periodic structure, however this technique may not be applied to arbitrary patterns [13].



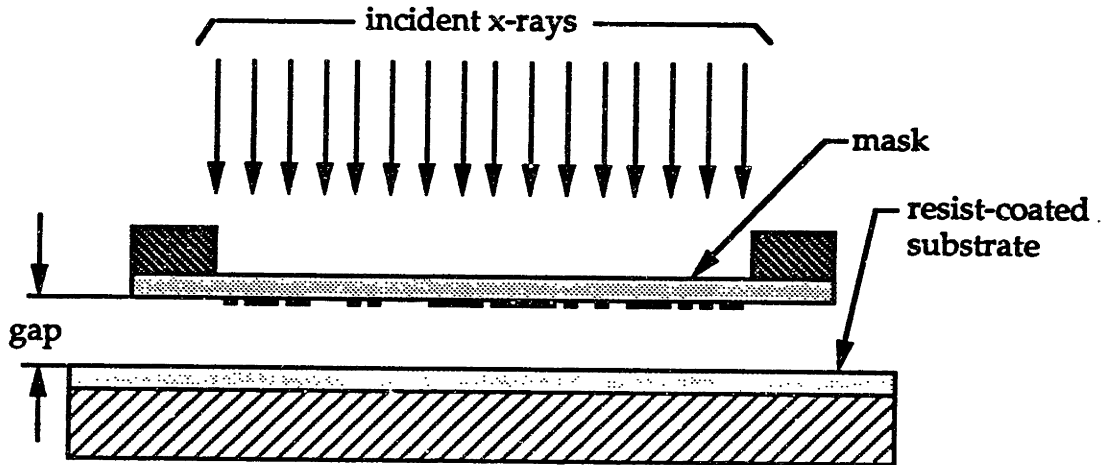


Figure 1.1: PPXRL configuration: An x-ray mask is held either in contact with or a small distance (4 to  $100\mu\text{m}$ ) from a resist-coated wafer and the assembly is exposed to x-rays. Essentially, the absorber pattern present on the semi-transparent x-ray mask membrane is shadow-cast onto the resist. When a gap is used between mask and substrate, each is protected from damage caused by the other or by particles that may come between the two.

These R&D efforts demonstrate that deep UV can probably enable industry to meet the  $0.25\mu\text{m}$  linewidth goal, but, further size reduction will require x-ray technology. To date, International Business Machines (IBM) has invested more than \$400 million in x-ray lithography; in Japan, upwards of a billion dollars has been slotted for x-ray lithography research and development [14]. Using PPXRL, researchers at IBM, led by A. D. Wilson, have fabricated a 64Kbit SRAM using an 11 mask process, all of which were patterned with x-rays [15]. At NTT, single NMOS transistors and 51-stage ring oscillators, fabricated using PPXRL for all 5 mask levels, have been successfully tested [16].

The way x-rays interact with matter differs significantly from the way the

visible spectrum affects matter, and understanding these differences is critical to understanding the issues involved in PPXRL. The index of refraction of materials is given by

$$\tilde{n} = n - i\beta = 1 - \delta - i\beta \quad (1.1)$$

In the x-ray regime the imaginary part is nonzero indicating absorption for all materials. In addition, the real part is less than but approximately equal to one:

$$n = 1 - \delta \approx 1 \quad (1.2)$$

Taken together, these two properties make refractive lenses impractical at x-ray wavelengths. This leaves essentially three choices: diffractive optics (zone plates); reflective optics (mirrors); or shadow casting as in PPXRL. Both reflective [17-20] and diffractive [21] cameras have been proposed. To date, no zoneplate camera has been implemented for x-ray lithography; and high light losses ( $\sim 40\%$ ) combined with lens aberrations make it an unlikely candidate for industry.

An experimental  $20\times$  reduction Schwarzschild objective system with multilayer-coated optics operating at 14nm has been used to image  $0.1\mu m$ -wide lines [19]. The image field is less than  $100\mu m$  across, much too small for commercial applications. For a viable commercial system, a peak-to-valley ratio of  $\lambda/300$  optical surface tolerance is required [20] for the multilayer mirrors, a condition that current technology cannot meet over large mirror areas. For practical through-put, masks as well as optics will have to be multilayer reflective surfaces. The fabrication, patterning and repair of these masks has yet to be developed.

In PPXRL the image field size is limited only by the mask size and the exposure field of the incident radiation. The biggest drawback in proximity printing is probably the one-to-one mask/image size ratio. Even with this drawback PPXRL remains, at this time, the only likely x-ray contender for widespread use in the semiconductor industry.

Sources of soft x-rays fall into three categories [22]. In increasing order of

brightness, these are: electron bombardment; laser produced plasma; and synchrotron. A typical synchrotron for lithography has sixteen beam lines and cost upwards of 120 million dollars. A commercial laser plasma source has brightness considerably lower than a synchrotron but costs only about two million; thus, it has the advantage of affordability. A simple, low brightness, electron bombardment point source was used for this thesis.

The partly-absorbing, partly-transmitting nature of x-rays sets limits on both materials and wavelengths suitable for lithographic use. The mask membrane must be mostly-transmitting, the "opaque" mask pattern must be mostly-absorbing, and the x-ray resist must be absorbing enough so that the required x-ray exposure time is not prohibitive and yet transmitting enough so that the entire thickness of resist is exposed. For typical wavelengths, between 0.8 and 5nm, attenuations in mask membranes, x-ray absorbers, and x-ray resist will range from 0.5–3, 6–128, and 0.4–2 dB/micron, respectively.

The best x-ray wavelength to use for a given application will depend upon the type of membrane used, the size of the mask-to-substrate gap, the required resist thickness, and the desired resolution. For a monochromatic or quasimonochromatic source, the amount of diffraction present in a microgap exposure depends upon the normalized parameter  $W/\sqrt{\lambda G}$  where  $G$  is the mask-to-substrate gap and  $W$  is the width of the feature. Diffraction can in theory always be reduced by reducing either the wavelength or the mask-to-substrate gap. In practice, the minimum gap will be constrained primarily by technological issues such as controllability and repeatability. Useful wavelengths are more fundamentally constrained. As the wavelength is reduced, more and more of the incident photons are transmitted both through the mask absorber and through the resist thus increasing the dose requirement and the absorber thickness requirement.

Resolution in x-ray lithography then is believed to be limited primarily by two effects: Photoelectron range and diffraction. It is primarily the experimental

exploration of these two effects that is the topic of this dissertation. Chapter 2 covers the way in which x-rays interact with matter and details an experiment which demonstrates that photoelectron range has negligible effect on resolution for linewidths down to 30nm for x-rays in the energy range  $0.28 \leq E_{\text{photon}} \leq 1.5\text{keV}$  ( $0.83 \leq \lambda \leq 4.5\text{nm}$ ). Chapter 3 outlines the mechanisms of exposure and development in the three x-ray resists used in the thesis. In particular, imaging of isolated  $\sim 0.1\mu\text{m}$ -wide lines and posts at a  $5\mu\text{m}$  gap is demonstrated in two new chemically amplified resists, the finest resolution for these materials to date [23]. In Chapter 4, I make use of these results to extrapolate the resolution limits for other resists, and estimate the effects of image contrast, field intensity fluctuations and shot noise on resolution degradation. Diffraction theory, modeling of source incoherence, and diffraction simulations for one dimensional mask patterns are presented in Chapter 5. Linewidth-gap diagrams are introduced in which families of equi-irradiance contours are plotted as a function of mask/substrate separation (gap). In Chapter 6 experimental conditions and results are detailed. The resolvability of three features, isolated lines, gratings and isolated spaces, of four sizes, is determined experimentally for  $\lambda = 1.34\text{nm}$  and gaps varying from 5 to  $100\mu\text{m}$ . The nominal linewidths investigated are 0.2, 0.3, 0.4, and  $0.5\mu\text{m}$ . The lines, spaces, and gratings were imaged on a sloped wall so that data for all gaps of interest was obtained in each exposure. These results are compared against the linewidth-gap diagrams from Chapter 5. Broad agreement is found between experiment and theory, though some important discrepancies are seen. Chapter 7 concludes with an analysis of results and their implications.

Three appendices have also been included. Appendix A spells out the process flow for the chemically amplified resists. Appendix B describes in detail polyimide maskmaking procedure for the type of mask used in the photoelectron experiment as well as for two-side patterned contact masks. A byproduct of the dissertation has been the acquisition of a wealth of experience in etching both (100) and (110)

silicon in potassium hydroxide (KOH), one example of which is a novel geometry for etching sub-10nm-thick vertical membranes in (110) material. All of this information is presented in Appendix C.

## Chapter 2

# Photoelectron Range and Resolution

When x-rays are absorbed in matter they release photoelectrons and lower energy Auger electrons; these in turn generate numerous secondaries. Photoelectron and Auger emission are illustrated schematically in Figure 2.1. The energy distribution of the photoelectrons is peaked near the difference between the photon energy,  $hc/\lambda$ , and the electron binding energy,  $E_B$ . Auger energies are determined by the chemical constituents of the target, in this case, photoresist which is composed of carbon, oxygen, and hydrogen. X-ray fluorescent yield for low  $Z$  materials such as these is negligible, so an Auger is generated for essentially every photoelectron. The energy of the Auger electron, which is lower than that of the photoelectron, depends solely on the chemical constituents of the target material and is independent of the photoelectron energy.

Since the earliest work in x-ray lithography [5,24] it has been assumed that it is the range of the emitted photoelectrons that ultimately limits image resolution. The reasoning behind this assumption is illustrated in Figure 2.2 which shows a single absorber line above a resist coated substrate. Photoelectrons associated with x-rays absorbed in the immediate vicinity of the mask feature have sufficient

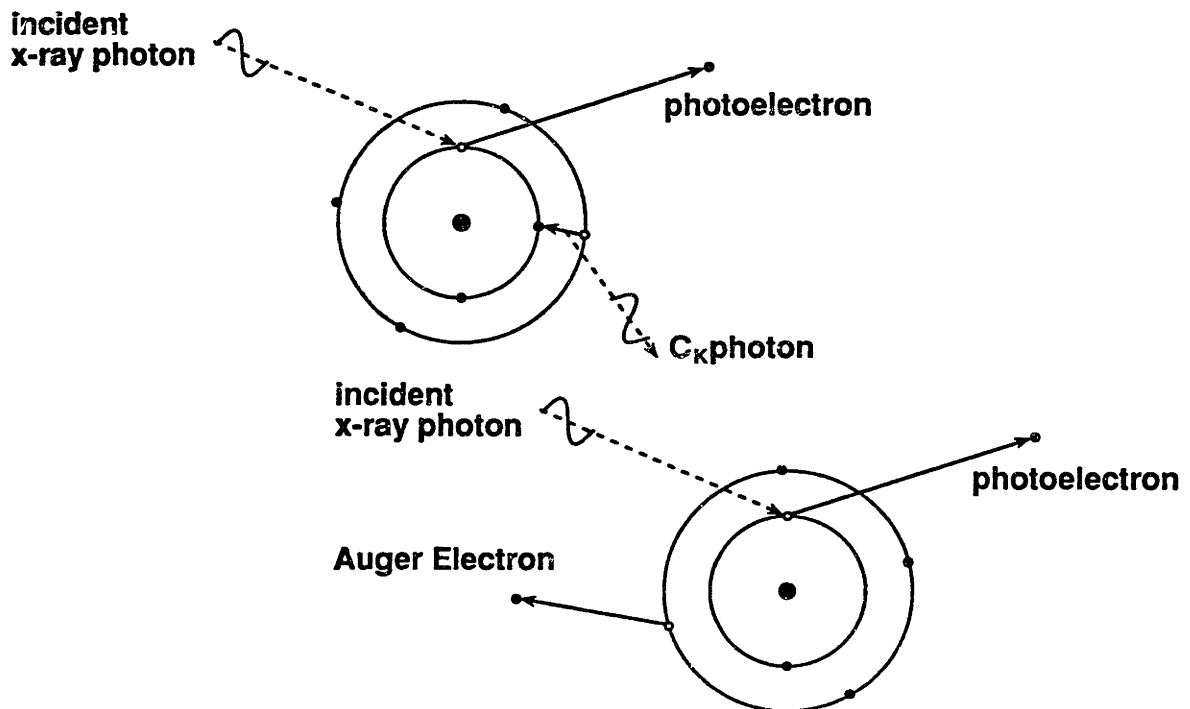


Figure 2.1: At left a photon is absorbed by a carbon atom which emits a photoelectron; an outershell electron fills the vacancy and a  $C_K$  photon is emitted. The cross section for the photon emission (fluorescence) from a low  $Z$  material such as carbon is nearly zero thus making this process unlikely. At right, through the process of internal conversion, the energy given up by the electron filling the vacancy is imparted to another electron allowing it to be emitted as an Auger.

energies to travel beneath the absorber line thus causing an edge undercut of  $\delta$  or a linewidth loss of  $\Delta L = 2\delta$ . Hence, to achieve higher resolution longer wavelengths have been used [8,25,26].

While the  $C_K$  x-ray ( $\lambda = 4.5\text{nm}$ ) has proven effective in reproducing sub-100nm features, shorter wavelengths, in the range of 1 to 1.4nm, are desirable [27] both to limit diffraction effects and to allow the use of nitride or silicon mask membranes which are virtually opaque to  $C_K$  radiation. To determine the effect of Auger and photoelectrons on resolution in a more direct experiment than has been reported to date [25,28], we fabricated a high-contrast mask with 30nm-wide absorber lines and used it to pattern PMMA resist with  $C_K$ ,  $Cu_L$ , and  $Al_K$  x-rays. The results

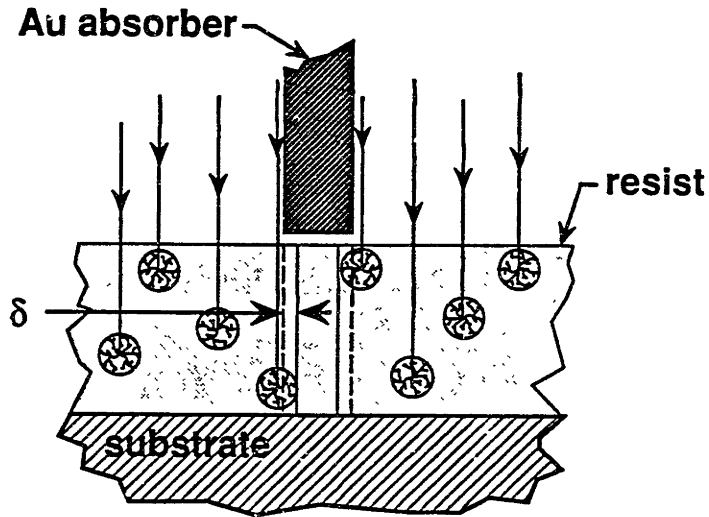


Figure 2.2: Schematic depiction of x-ray photon absorption in resist in the vicinity of a single Au absorber line. The Au line is part of an absorber pattern on an x-ray mask that is in contact with the resist coated substrate. Photoelectrons have sufficient range to travel beneath the absorber. For many years it was thought that this would cause a shrinkage in linewidth shown here as an undercut in the resist profile.

of this experiment show negligible difference in the lines replicated by the three x-ray wavelengths.

## 2.1 Previous Studies

The range of photoelectrons in a target material can be estimated using the empirical Grün range formula [29,30]

$$R_g = (0.046/\rho)E_p^{1.75}(\mu\text{m}) \quad (2.1)$$

where  $\rho$  is the target material density in  $\text{g}/\text{cm}^3$  ( $1.2\text{g}/\text{cm}^3$  for a typical x-ray resist) and  $E_p$  is the photoelectron energy in keV. Considering photoelectrons generated in carbon and oxygen atoms, Equation 2.1 yields ranges of 0, 8-18, and 35-53 nm



for  $C_K$ ,  $Cu_L$ , and  $Al_K$  x-ray energies, respectively. The use of Equation 2.1 is questionable though because the Grün range formula was extracted from data for electrons with  $5 \leq E \leq 25$  keV; its validity in the 1 keV range is undetermined.

To measure the range of electrons generated in resist, Feder *et al.* [25] added a 28 nm-thick layer of erbium to a PMMA coated substrate and exposed the sample to  $Al_K$  radiation ( $\lambda = 0.83$  nm). The idea was that the x-rays would be strongly absorbed in the erbium; the photo, Auger, and secondary electrons generated in the erbium layer would be emitted into the underlying PMMA. By plotting resist thickness versus development time the authors determined that the exposure range of electrons generated by  $Al_K$  x-rays is 40 nm and anticipated that this would be the minimum feature size replicable with  $Al_K$  x-rays. This experiment provides useful information on the maximum range in PMMA of electrons generated by  $Al_K$  x-rays in *erbium*, but it does not reflect true x-ray lithography exposure conditions where the development profile will be tied to the x-ray absorption in the *resist*. In this experiment a larger flux of electrons was generated than would be in a typical exposure situation and the electron energy distribution differed from that which would be caused by photon absorption in PMMA.

Rishton *et al.* [28] bombarded PMMA with electrons in narrow energy ranges between 100eV and 2.5keV and measured the maximum developed depth, which they called the exposure range. On the basis of these measurements one can estimate the exposure range of photoelectrons generated in PMMA. The major constituent atoms, C and O, have  $E_B = 283$ eV and  $E_B = 531$ eV, respectively. The photoelectron energies are calculated from

$$E_{pe} = E_{ph} - E_B \quad (2.2)$$

The exposure ranges for photoelectrons from 0.28, 0.93, and 1.5keV x-rays are given in Table 2.1.

These estimates, based on normal incidence measurements, cannot be used

X-ray Source	Wavelength (nm)	X-ray Energy (keV)	Photoelectron Energies (keV)	Expected Exposure Range (nm)
C <sub>K</sub>	4.5	0.28	~ 0	~ 0
Cu <sub>L</sub>	1.3	0.93	0.4 <sup>(a)</sup> , 0.65 <sup>(b)</sup>	20 - 30
Al <sub>K</sub>	0.83	1.48	0.95 <sup>(a)</sup> , 1.2 <sup>(b)</sup>	40 - 75

Table 2.1: Photoelectron ranges calculated from data in reference [28] for (a) carbon and (b) oxygen, the constituent species of interest in PMMA.

directly to predict changes in a patterned feature caused by lateral photoelectron scatter. The probability distribution of photoelectron emission is the well known doughnut-shaped dipole radiation pattern; the emitted photoelectron's path is further randomized by collisions within the resist. The emitted carbon and oxygen Auger electrons with energies of 270 and 507eV, respectively, have corresponding exposure ranges of ~ 16 and 18 nm. These Augers and the numerous low energy secondaries contribute to the distribution of the photon energy in the resist, thus influencing the exposure profile.

Most importantly, the doses used in reference [28] produce roughly two orders of magnitude more high energy electrons than would be generated in an x-ray exposure. For example, a developed depth, or exposure range, of 20 nm is given for a dose of 250  $\mu\text{C}/\text{cm}^2$  using 500eV electrons. This corresponds to  $\sim 10^{18}$  electrons/ $\text{cm}^3$ . A typical x-ray dose of 1 to 2kJ/ $\text{cm}^3$  corresponds to only  $\sim 10^{16}$  photoelectrons/ $\text{cm}^3$ . The experimental data of Rishton *et al.* has proven useful for verifying the accuracy of electron penetration simulations [31], but cannot be used directly to predict minimum feature sizes in x-ray lithography.

Murata [32] and Murata et al. [33] have done Monte Carlo calculations of the absorbed energy density in PMMA caused by Cu<sub>L</sub>-, Al<sub>K</sub>-, and Mo<sub>L</sub>-excited Auger and photoelectrons as a function of lateral distance. Plots for Cu<sub>L</sub> and Al<sub>K</sub> x-

rays, from Figure 5 of reference [33], which take account of photoelectron and Auger emission probability distribution and subsequent path randomization, are reproduced here in Figure 2.3. Figure 2.3 (b) shows that for  $Al_K$  excitation the absorbed energy falls off by 3dB at 8 nm from the point of x-ray absorption in the resist, and by 10dB at  $\sim 35$  nm.

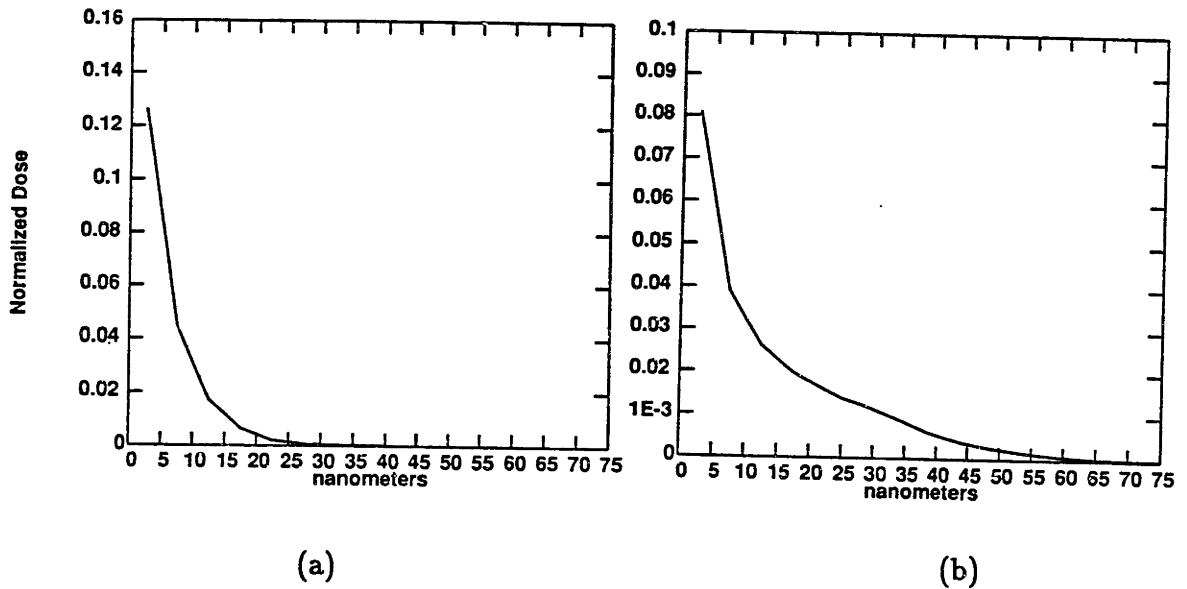


Figure 2.3: Normalized energy distribution for absorbed (a)  $Cu_L$  and (b)  $Al_K$  x-rays from an infinitely thin line source. From Reference [33].

Murata has defined two regions, one dominated by Augers, the other by photoelectrons. Curiously, the electron exposure ranges, measured by Rishton *et al.*, that correspond to the carbon and oxygen Augers are close to three times the HWHM of Murata's plot. This discrepancy is explained by the fact that, in their experiment, Rishton *et al.* used a 3 minute development time since they found that longer times produced "no detectable change in (developed) depth." Thus, they essentially measured the tail of the energy distribution.

Murata's Monte Carlo simulation utilizes the screened Rutherford equation to model angular scattering; energy loss as a function of distance is calculated with

the aid of the Bethe equation. Thus, the generation of secondaries, their energy distribution, and quantity are not explicitly included, though their cumulative effect is accounted for.

In considering the dose (absorbed energy per unit volume) required to expose resist a question of interest is how the number of secondaries generated per absorbed photon changes with x-ray energy. Typically, secondaries make up from 50 to 90% of an x-ray photoemission spectrum from a solid target excited with photons in the 100eV to 10keV range [34]. Secondaries are generated by four types of interactions [34]: (1) through weak coupling to high velocity primaries (i.e. photo and Auger electrons); (2) by collisions with low velocity primaries; (3) by plasmon decay; and (4) by cascading (i.e. secondaries generating secondaries). This last category, cascaded secondaries, is underrepresented in photoemission spectrum measurements as compared to the number believed to be generated in the bulk by as much as a factor of 3, though the correction factor will depend on the specific target material [34]. We can estimate then that the number of secondaries per photon is  $\sim 10$  to 50. While it is known that the number of generated secondaries is a decreasing function of primary electron energy for excitation by 50 to 100keV electrons [35], we will assume that the number of secondaries per photon is a slowly varying function of incident x-ray energy in the comparatively low energy range from 0.28 to 1.5keV.

## 2.2 Experimental

Figure 2.4 depicts the experimental set-up that was used to replicate a single mask pattern with three different x-ray wavelengths. The mask was held in electrostatic contact with a PMMA-coated wafer at 10.5cm distance from an x-ray point source whose diameter was approximately 1mm. For the  $\text{Cu}_L$  and  $\text{Al}_K$  exposures, a 1.2  $\mu\text{m}$ -thick silicon nitride membrane was placed between the source and the mask

to filter any carbon or oxygen x-rays that may have been generated from surface contaminants on the x-ray source. As can be seen from the enlarged view, the x-ray absorber consists of a thin gold coating on the sidewalls of a grating molded into a polyimide mask membrane [36,37].

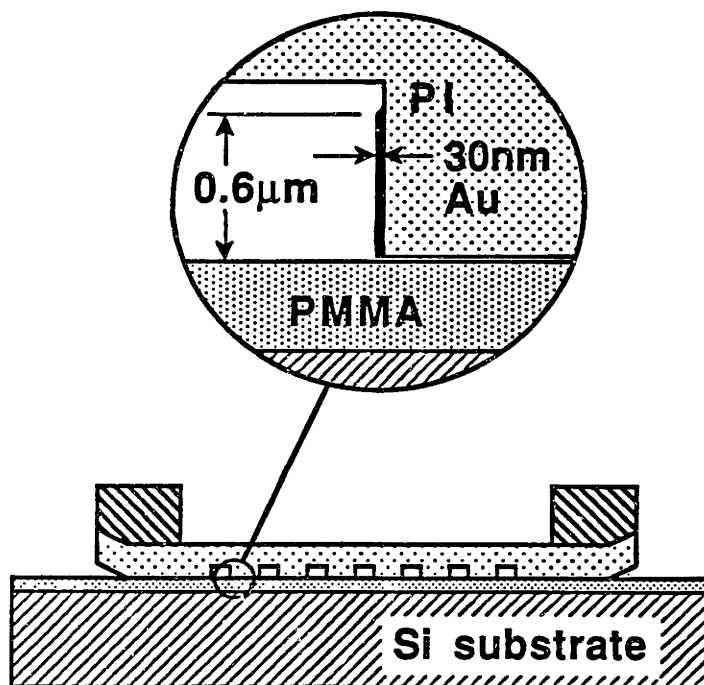


Figure 2.4: Experimental set-up: The absorber lines are evaporated on the side-wall of the polyimide grating mask. For exposures with  $\text{Cu}_L$  and  $\text{Al}_K$  x-rays a 1  $\mu\text{m}$ -thick silicon nitride membrane (not shown) was placed between the mask and the x-ray source to filter out low energy electrons.

The mask was fabricated by first anisotropically etching in KOH a (110) silicon wafer that had a 5  $\mu\text{m}$ -period grating patterned in  $\text{Si}_3\text{N}_4$  on its surface. The resulting relief grating was 0.75  $\mu\text{m}$ -deep with sidewalls that are Si {111} planes, perpendicular to the wafer surface, and nearly atomically smooth. After the KOH etch, the  $\text{Si}_3\text{N}_4$  was stripped and polyimide spun on so that it conformally filled the grating. The silicon was then etched away and a ring bonded to the polyimide membrane to provide mechanical support. Next, 5nm of chromium and 25nm of

gold were evaporated onto the grating sidewalls from a steep angle. With the mask in contact with a wafer, the evaporated Cr-Au is only 30nm in the direction parallel to the wafer surface but more than 0.6  $\mu\text{m}$ -thick parallel to the exposing x-rays. As can be seen from Figure 2.5, a 0.6  $\mu\text{m}$ -thick absorber provides attenuations of 12, 30, and 77 dB for  $\text{Al}_K$ ,  $\text{Cu}_L$ , and  $\text{C}_K$  x-rays, respectively. The final step in mask fabrication was the deposition of 30nm of aluminum on the back side of the mask to form an electrical contact. The complete details of mask fabrication and illustrations of processing steps are given in Appendix A.

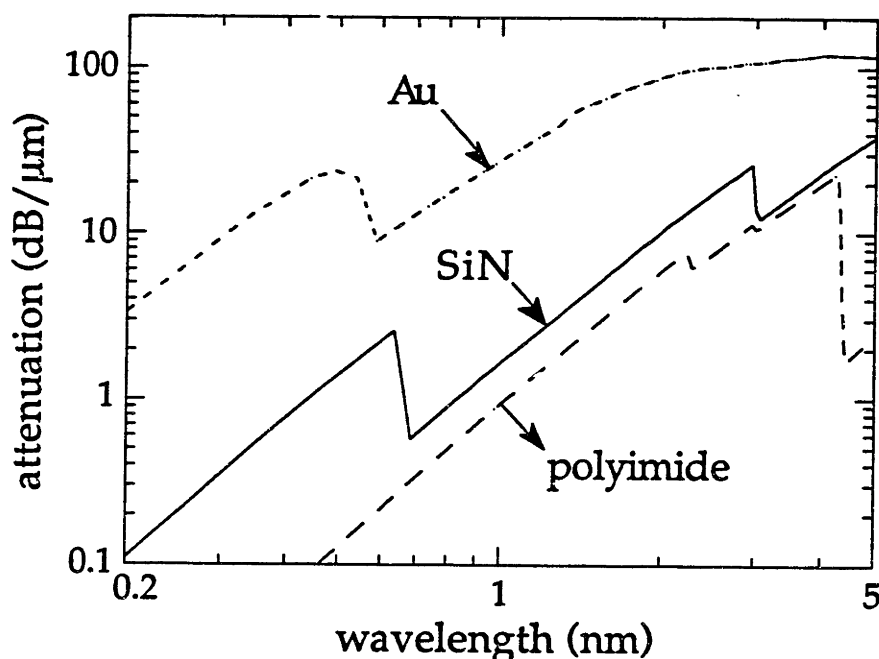


Figure 2.5: X-ray attenuation curves for Au, SiN, and polyimide.

The mask was used to pattern substrates coated with  $\sim 30$  nm of 950,000 molecular weight PMMA [38]. The PMMA was then developed in a 2:3 mixture of MIBK (methyl isobutyl ketone):IPA (isopropyl alcohol). Exposure and development conditions are given in Table 2.2 along with calculated doses [39].

X-ray Source	Accelerating Voltage (keV)	Power (Watts)	Exposure Time (hrs)	Dose <sup>(a)</sup> (kJ/cm <sup>3</sup> )	Development Time (sec)
C <sub>K</sub>	6.0	300	16	~ 1.0 <sup>(b)</sup>	80
Cu <sub>L</sub>	8.0	600	8	~ 0.8	60
Al <sub>K</sub>	5.0	300	20	~ 1.0	60

Table 2.2: (a) Doses calculated from data in reference [39]. (b) Calculated for thickest PI and assumes 30 nm of Au on horizontal mask surface.

## 2.3 Results

Figure 2.6 shows scanning electron micrographs of lines developed in PMMA after exposure to C<sub>K</sub>, Cu<sub>L</sub>, and Al<sub>K</sub> x-rays. These were taken from a region of the wafer where the exposing x-ray flux was perpendicular to the mask plane. Because the aspect ratio of the absorber is 20:1, we considered the possibility that our results, especially for the Al<sub>K</sub> exposure, were spurious by virtue of the absorber being tilted, thereby making the absorber effectively wider than 30nm. However, any tilt-induced widening would be much greater in the Cu<sub>L</sub> and C<sub>K</sub> results because of the much greater attenuation. Since linewidths in PMMA are virtually the same for all three sources, and since the same mask was used in all three cases, we conclude that the absorber was not significantly tilted.

## 2.4 Discussion

For all three wavelengths the replicated linewidth matched the absorber linewidth to within 5nm. The 30nm-wide lines are narrower than the exposure ranges given in Table 2.1 for photoelectrons generated by either Cu<sub>L</sub> or Al<sub>K</sub> x-rays. These results, which are at variance with a number of previous calculations, predictions,

and assumptions about the impact of photoelectron range on resolution in PMMA [5,24,25,27,40,41], can be explained with the aid of the absorbed energy density data of Murata et al. shown in Figure 2.3. For a 2:3 MIBK:IPA mixture, the development rate is proportional to the cube of the dose [42,43]. The absorbed energy has fallen to 75% of the maximum 5 nm from the point of photon absorption. The resist at this point will take 2.5 times as long to develop as the resist at the origin. It is worth noting that lines such as the ones shown in Figure 2.6 are virtually impossible to pattern using e-beam lithography where proximity effects, caused by both forward and backscattered electrons, limit fine line patterning to clear lines in a dark field, the reverse polarity of that shown here.

The 30nm-wide lines shown here are the finest ever replicated with  $Al_K$  x-rays ( $\lambda = 0.83\text{nm}$ ); it is unlikely that such fine features will be routinely patterned using this wavelength because the required high aspect ratio masks are difficult to fabricate and image contrast is low. This last point is made clear by Figure 2.7 which shows convolutions of the  $Al_K$  absorption data from reference [33] with a 30 nm-wide line and a 30 nm-wide slit for (a) an infinite contrast mask and (b) a 10dB contrast mask. As can be seen from Figures 2.8 (a) and (b), wavelengths near the  $Cu_L$  line ( $\lambda = 1.3\text{nm}$ ), which requires only 200nm gold absorber for 10dB attenuation, are more suitable for sub-100nm features.

Though this experiment involved only contact exposures, diffraction effects, caused by the resist thickness and the absorber height, may not be negligible. Diffraction is neglected in this analysis because modeling it requires complete electromagnetic finite element analysis of the high aspect ratio features [44], which is beyond the scope of this thesis.

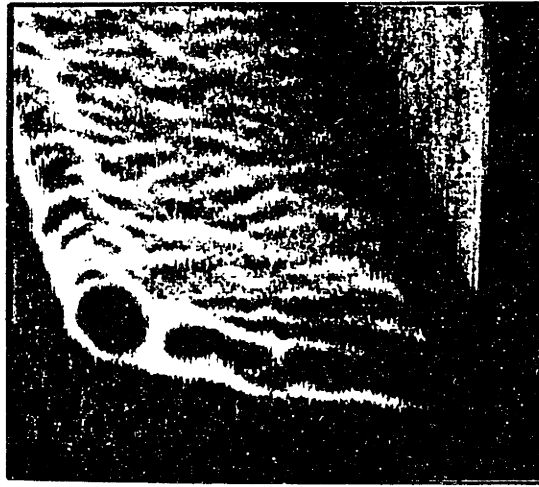
Aside from the issue of electrons generated in the resist, another issue of concern is photoelectrons and Augers generated in the mask or in the substrate which can cause spurious resist exposure [25,29,45-48]. Photoelectrons ejected from the mask have been shown to cause crosslinking of the top surface of negative resist im-



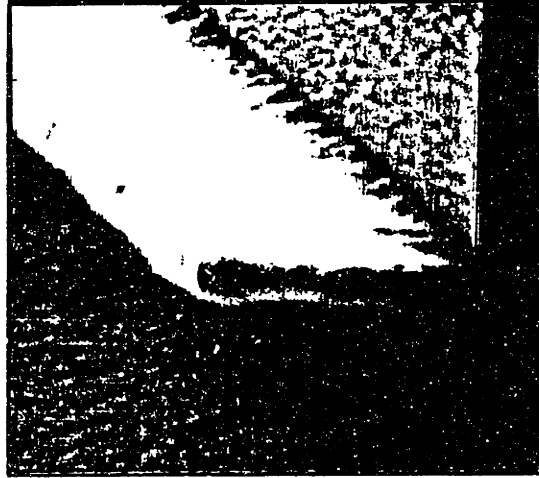
mediately below the mask absorber [47]. Electrons ejected from molybdenum [29], gold [25], and silicon [45] substrates have been shown to add to the exposure dose of the bottom layer of resist thus causing adhesion problems for positive PMMA. With the exclusion of reference [25], these effects have all been seen for x-rays wavelengths in the 0.2 to 0.5nm range, shorter than those used here. The  $\text{Cu}_L$  line is routinely used in our Submicron Structures Laboratory at M.I.T. to pattern wafers with gold plating base; for this wavelength no loss of adhesion is seen. In Chapter 6 we will see clear evidence of contributions to the developed profile from electrons emitted from a Au coated substrate for the case of a low contrast image. As will be discussed in Chapter 3, we have seen some crosslinking of the surface layer of negative Ray-PN for sub-100nm features though it is uncertain at present whether this is a photoelectron or a chemical effect. It has been shown that if a polymer coating is added to the front mask surface, surface crosslinking by photoelectrons can be eliminated and thus is not of fundamental concern [47].

**Figure 2.6: Replication in PMMA of a 30nm-wide Au absorber line with (a)  $C_K$  ( $\lambda = 4.5\text{nm}$ ), (b)  $Cu_L$  ( $\lambda = 1.3\text{nm}$ ), (a)  $Al_K$  ( $\lambda = 0.83\text{nm}$ ) x-rays.**

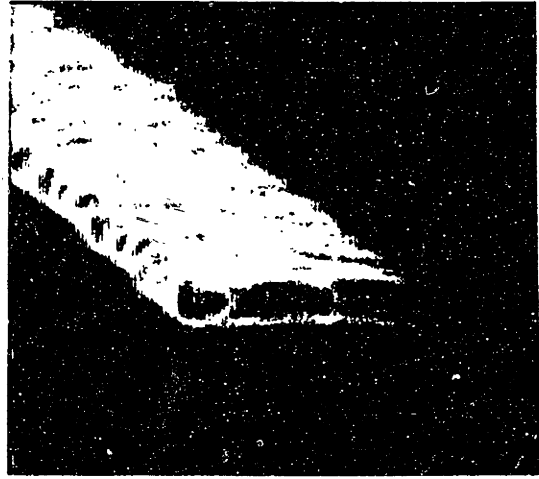
# Replication in PMMA of 30nm Wide Au Absorber



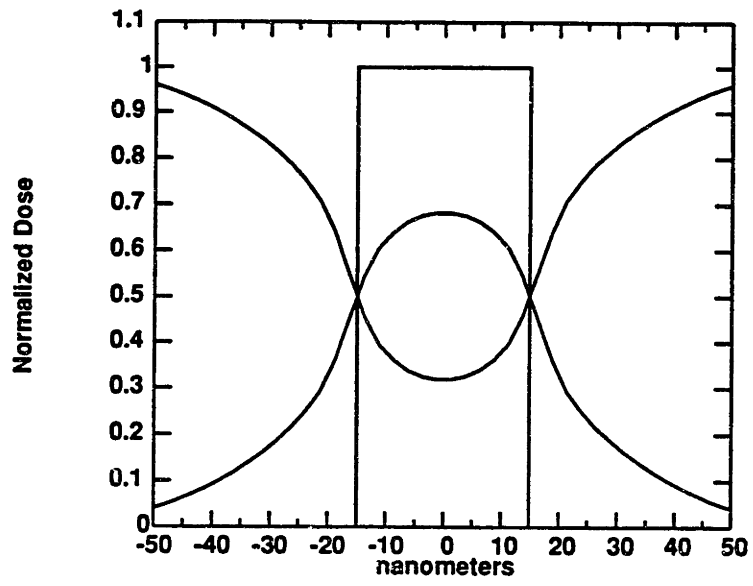
**C<sub>K</sub> X-Ray**  
 $\lambda = 4.4\text{nm}$



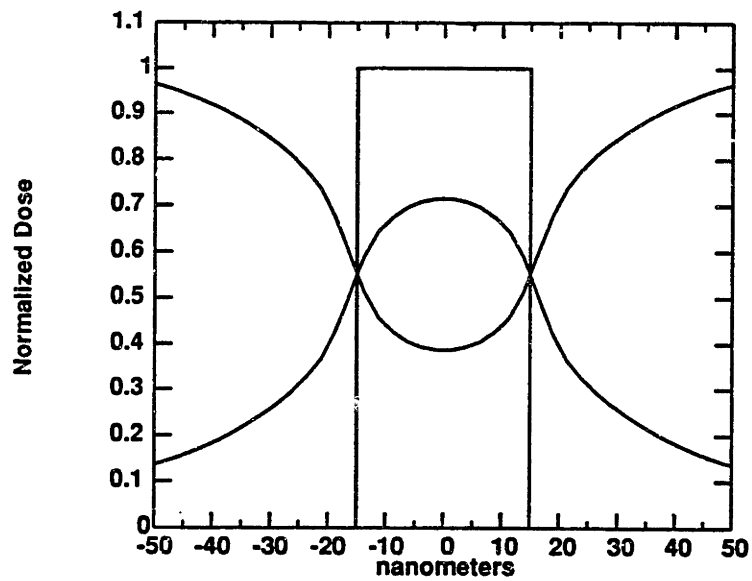
**Cu<sub>L</sub> X-Ray**  
 $\lambda = 1.3\text{nm}$



**Al<sub>K</sub> X-Ray**  
 $\lambda = 0.8\text{nm}$

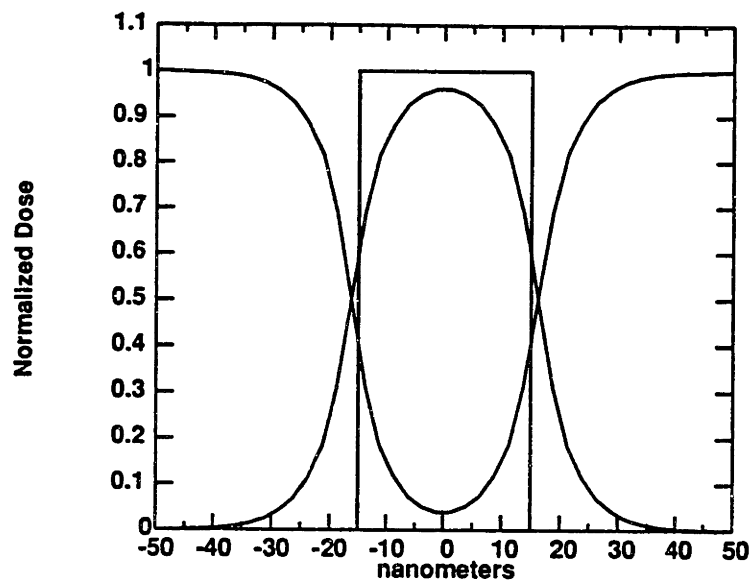


(a)

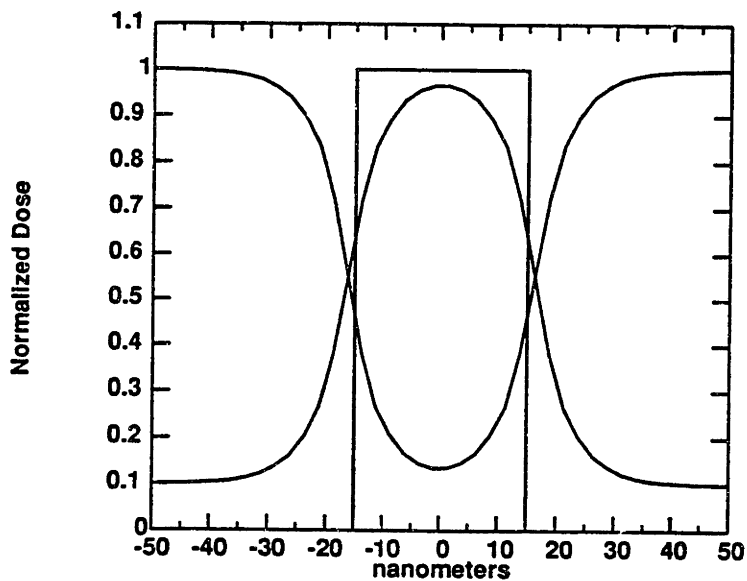


(b)

Figure 2.7: Convolution of intensity for a 30-nm wide slit and a 30 nm-wide with the absorbed energy density function [33] for  $Al_K$  x-rays (a) from an infinite contrast mask (b) from a 10 dB attenuating mask.



(a)



(b)

Figure 2.8: Convolution of intensity for a 30-nm wide slit and a 30 nm-wide slit with the absorbed energy density function [33] for  $\text{Cu}_L$  x-rays (a) from an infinite contrast mask (b) from a 10 dB attenuating mask.

# Chapter 3

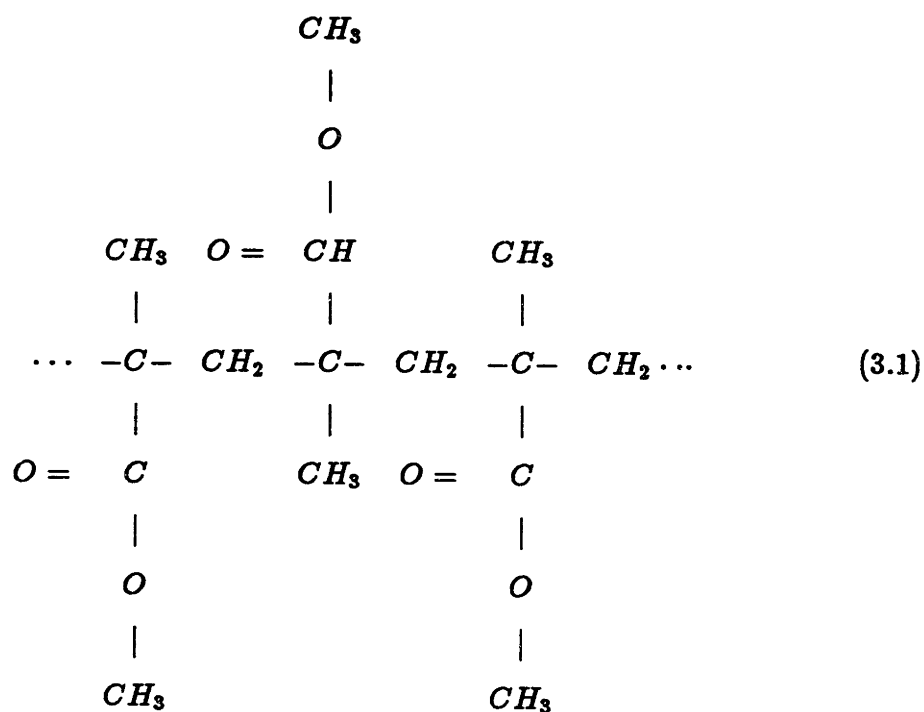
## X-Ray Resists

Micro and nanolithographic resists can be roughly divided into categories as one, two, three component system. PMMA is an example of a one component system (1CS); typical UV novolak resists are two component systems (2CS). The new chemically amplified x-ray resists (CARs) are three component systems (3CS). PMMA was introduced in Chapter 2 in the photoelectron range experiment and is discussed in greater detail in Section 3.1 below. The 3CS CARs are introduced in section 3.2.

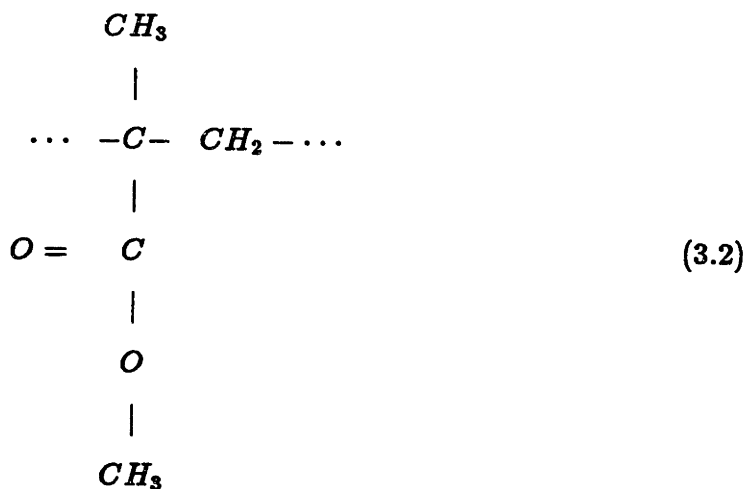
### 3.1 Polymethyl Methacrylate Resist

PMMA was first used as a resist at IBM Watson Research Center in the late sixties [49]. It exhibits the highest resolution ( $\sim 10\text{nm}$ ) of any organic resist to date. Other virtues include extremely high contrast and well understood, consistent, stable behavior. Its stability comes from its one component nature and is manifest in its virtually infinite shelf life both before and after spinning. PMMA can be developed immediately after exposure or it can be developed a few days later; the result will be the same in either case in marked contrast to 2CS and 3CS novolak resists.

PMMA consists of high-molecular-weight (20K to 1M), longchain, intertwined molecules which have isotactic, actactic, and syndiotactic forms with  $T_g$ s of approximately 40°C, 117°C, and 170°C, respectively [50]. The syndiotactic structure, which has the lowest solubility rate of the three forms and which corresponds to SSL processing conditions, is given below [50]:



The basic unit cell is [51]:



The best explanation of exposure and development mechanisms of PMMA are given by Ouano [50,52]. Exposure of PMMA, whether by electrons or photons, causes main chain scissioning as well as the removal of side groups from the molecules. This reduces both the molecular weight and the resist density. The removed side groups outgas from the PMMA thus greatly increasing the resist porosity and hence developer diffusivity. Indirect evidence of this outgassing behavior is commonly seen in the SSL in that a mask placed in electrostatic contact with a PMMA coated substrate will come out of contact during exposure unless the mask surface is patterned with a relief structure that provides escape channels for the outgassing species [53]. Direct evidence is seen prior to development of the resist in that the latent image is clearly visible indicating a difference in refractive index between exposed and unexposed regions.

Ouano has shown, using his own data and that of Greeneich [54] and Hirakawa [55], that dissolution of PMMA in a solvent developer is a weak function of resist molecular weight and a strong function of resist density. By using a variety of solvents, with different size molecules, as developers, Ouano was able to determine a characteristic size of the micropores in the exposed PMMA to be  $\sim 1$  nm. Experimental data [42,43] has shown the dissolution rate of syndiotactic PMMA vs. dose to be an approximately cubic response for a developer mixture of 40% methyl isobutyl ketone (MIBK) and 60% isopropyl alcohol (IPA).

PMMA's strongest point is synonymous with its greatest drawback: The cost of its phenomenal resolution is insensitivity. Typical x-ray doses are in the range from 1 to  $2 \text{ kJ/cm}^2$ , and, for industry, this leads to prohibitively long exposure times. Another major drawback which makes PMMA unsuitable for the IC industry is its poor plasma etch resistance. Chemically amplified resists, the subject of the next section, get around these two drawbacks at the cost of reduced resolution and reduced process stability. Nevertheless, it is PMMA which has allowed the fields of e-beam, focused-ion-beam, and x-ray lithography to move forward.



## 3.2 Chemically Amplified Resists

Intense effort over the last few years has led to the development and marketing of a new class of novolak resists that are sensitive to x-rays; two of these, Ray-PF, a positive resist, and Ray-PN, a negative resist, are the subject of this section [26,41,56-63]. The term novolak refers to the binder matrix component of the resist which is soluble in an aqueous base developer and which gives the resist its good dry etch resistance. This last is a property which is crucial for IC manufacturing. Two component novolak positive UV resists have been standard in the microcircuit industry for decades. The second component in these resists is a dissolution inhibitor which is converted upon exposure to a dissolution enhancer.

In the new chemically amplified x-ray resists (CARs), the radiation induced differentiation, i.e. conversion of the resist from indissolvable (or dissolvable) to dissolvable (or indissolvable) upon photon absorption, which is performed by a single component in UV resists, is separated into two distinct functions which are each handled by separately optimized components [57,58]. When a photon is absorbed, an acid is generated in the resist which acts as a catalyst in what is called a dark reaction. The term, dark reaction, is used to indicate that the reaction takes place during some time interval after exposure. For the positive Ray-PF, the dark reaction consists of hydrolysis of the dissolution inhibitor [58]; for negative Ray-PN, the acid catalyzed reaction is the crosslinking of the phenolic matrix resin [58]. The three components of CARs then are: the novolak binder matrix; a photosensitive acid generator; and an acid catalyzed converter.

Like PMMA, these resists have extremely high contrast, and they overcome its two major drawbacks. Acid catalysis increases sensitivities of CARs more than an order of magnitude above that of PMMA, and they have the requisite dry etch resistance. These gains do not come without costs; the major two are increased processing complexity and reduced resolution. The effect of chemical

amplification is illustrated schematically in Figure 3.1. The absorption of a single photon will generate some unknown number of acid molecules. Each acid molecule will catalyse reactions at many different sites. Oertel et al. [26] have estimated the average acid range to be  $\sim 16$  nm for Ray-PF. The volume associated with an absorbed photon is larger in this case than in the case of PMMA and is influenced by resist processing conditions.

The chemically amplified resist response is influenced by softbake and post-exposure-bake times and temperatures as well as by the surrounding chemical environment. For example, chemical neutrality of the wafer surface prior to spinning is required to achieve good adhesion and prevent wafer surface scum after development [63].

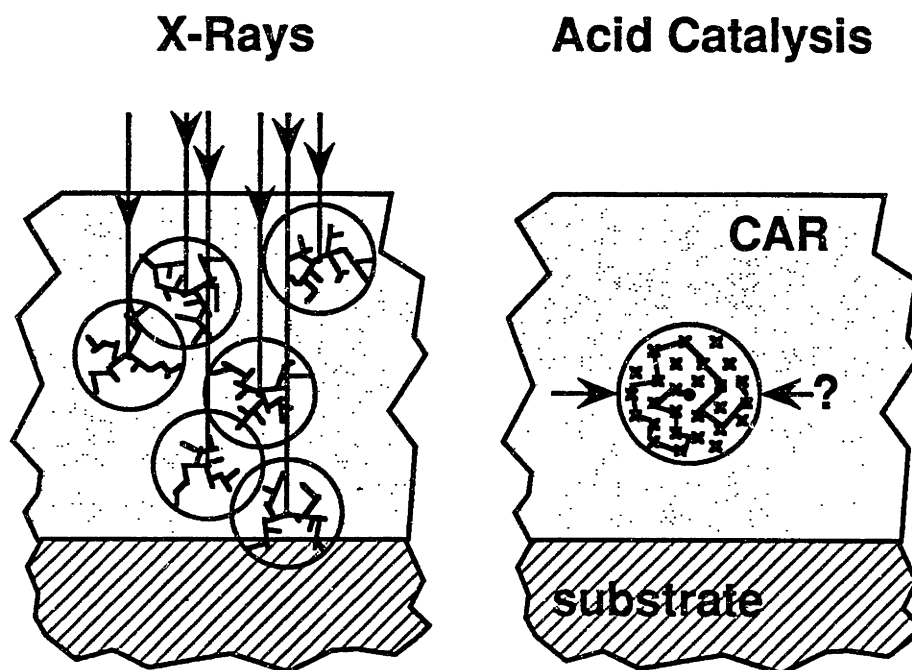


Figure 3.1: At left a photon is absorbed in the resist generating a number of acid molecules. At right a single acid molecule act as a catalyst at many sites causing chemical amplification. The volume associated with its influence is unknown.

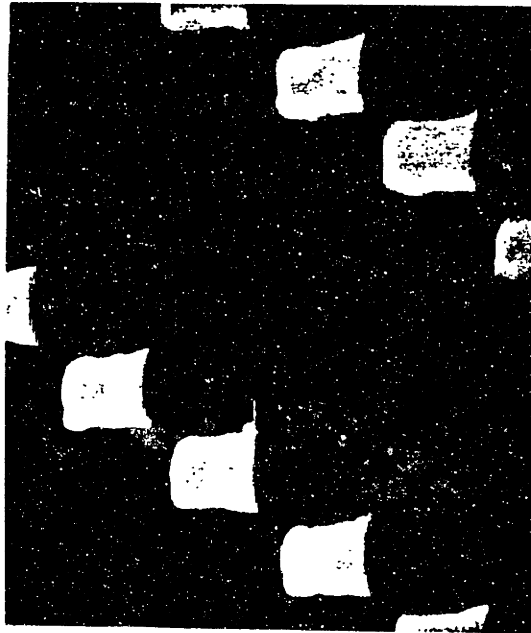
Additional difficulties are a pronounced loss of sensitivity at the rate of 4% per

hour in vacuum for Ray-PF [63] and a surface induction layer which sometimes prevents complete development of the top 50nm of resist [23]. The surface induction layer has been seen with both Ray-PF and with Ray-PN but is not necessarily attributable to the same cause in both instances. Possible causes are a reaction of the surface layer of resist with the room ambient, or, in the case of Ray-PN, crosslinking of the surface by photoelectrons generated in the x-ray mask absorber.

Exposures made in PMMA, Ray-PN, and Ray-PF, all from the same mask, are shown in Figures 3.2 through 3.6 [23]. Note the hourglassing in the Ray-PF exposure shown in Figure 3.4. This hourglassing is caused by overexposure as can be seen by a comparison with the vertical profiles in Figure 3.5 which shows a thicker film exposed with a lower dose and different processing conditions. The scum that remains on the wafer surface is probably an artifact of wafer surface preparation prior to resist spinning; this is discussed in detail in Appendix A. Examples of a surface induction layer effect can be seen in the lacy film that remains in some exposed areas in the Ray-PN films shown in Figure 3.6. Processing conditions for each exposure are given in the figure captions; Appendix A details process flow for Ray-PN and Ray-PF. The examples shown here were all done as part of resist processing development. Because of the many parameters influencing the developed profile, in subsequent diffraction experiments all controllable conditions other than exposure time and gap were kept constant. The Ray-PF exposures show the smallest features yet imaged in this resist; 50nm-size defects in the mask have been duplicated in Ray-PN (not shown here) and 80nm-wide lines have been imaged by others [62].

Figure 3.2: PMMA [38] resist, 950K molecular weight,  $0.25\mu\text{m}$ -thick, prebaked at  $180^\circ\text{C}$  for 30 minutes, and exposed using the Hampshire instruments 10P x-ray plasma source with a  $5\mu\text{m}$  mask-to-substrate gap. Dose to the resist was  $200\text{mJ}/\text{cm}^2$ ; development time was one minute in 40:60 MIBK:IPA.

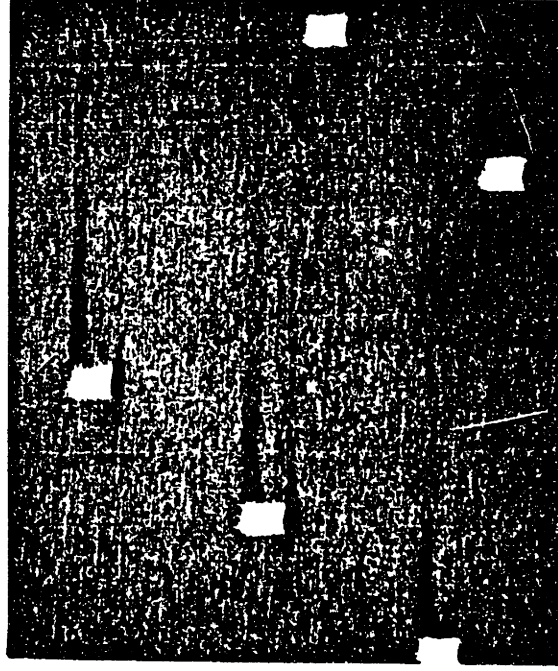
# PMMA exposed using Hampshire 10P Source



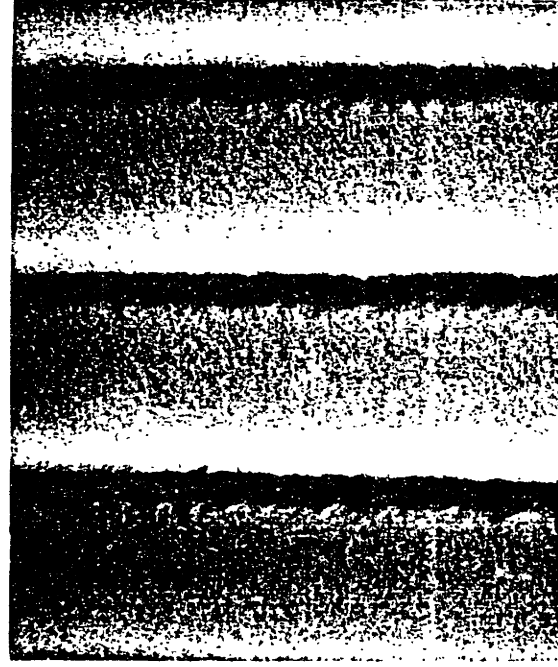
**Dose: 200mJ/cm<sup>2</sup>**

**Figure 3.3: Ray-PN resist, 0.25 $\mu$ m-thick, softbaked at 80°C for 30 minutes, and dosed with 18mJ/cm<sup>2</sup> of 1.3nm x-rays (Cu<sub>L</sub>) at a 5 $\mu$ m mask-to-substrate gap. The wafer received a five minute post-exposure-bake at 105°C on a vacuum chucked hotplate. Development time was five minutes in 1:1 AZ Developer and DI H<sub>2</sub>O.**

# Ray-PN exposed with $\text{Cu}_L$ ( $\lambda=1.3\text{nm}$ )



→ || ← 0.15 $\mu\text{m}$



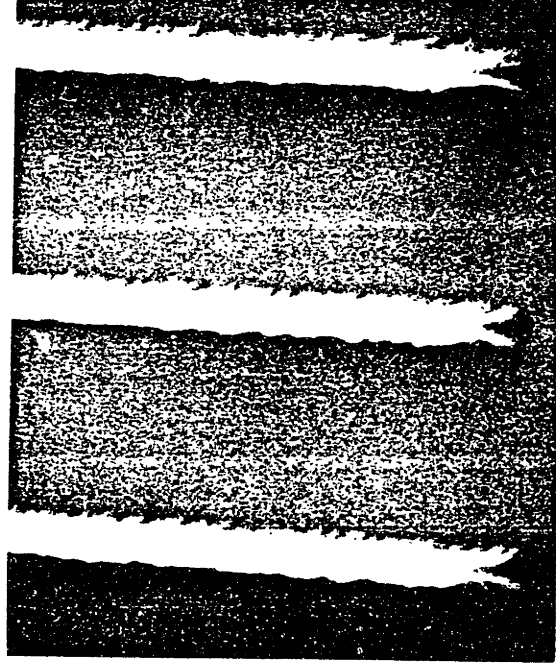
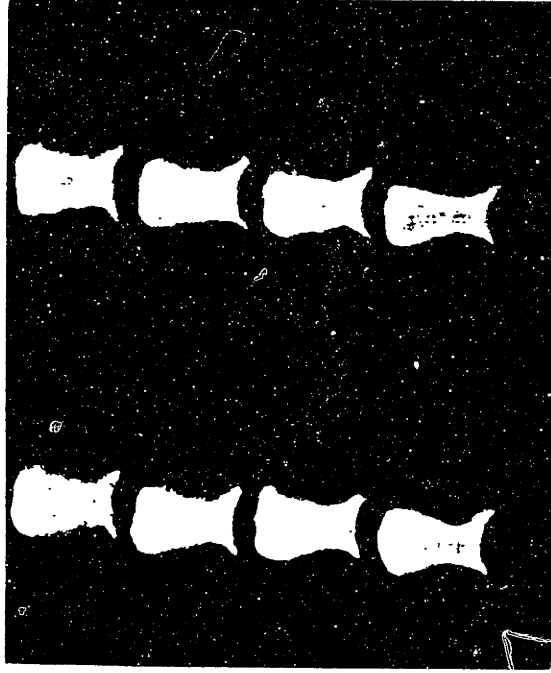
→ || ← 0.1 $\mu\text{m}$

**Dose: 18mJ/cm<sup>2</sup>**

Figure 3.4: Ray-PF resist, 0.4 $\mu$ m-thick, softbaked at 80°C for 30 minutes, and exposed with 7.5mJ/cm<sup>2</sup> of 1.3nm x-rays at a 5 $\mu$ m mask-to-substrate gap. The postexposure hold time was one hour, and was followed by a one minute 60°C hotplate bake. Development time was two minutes in 1:1 AZ Developer and DI H<sub>2</sub>O.



# Ray-PF exposed with $\text{Cu}_L$ ( $\lambda=1.3\text{nm}$ )



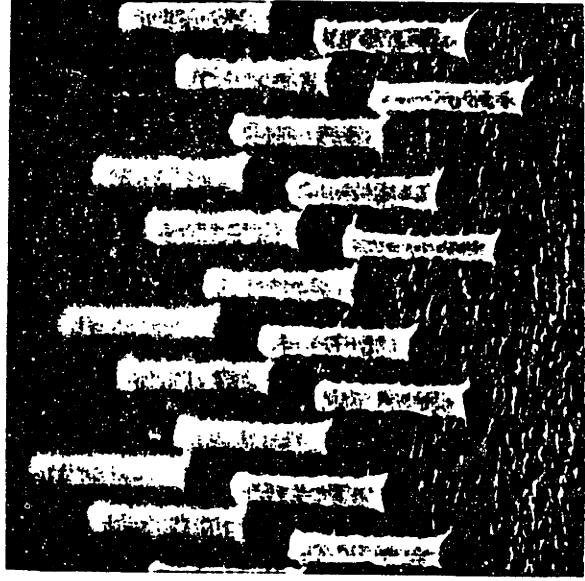
→ | | ← 0.15 $\mu\text{m}$

→ | | ← 0.1 $\mu\text{m}$

**Dose: 7.5mJ/cm<sup>2</sup>**

Figure 3.5: Ray-PF resist,  $1\mu\text{m}$ -thick, softbaked for one minute on a vacuum chucked hotplate at  $120^\circ\text{C}$ , and exposed with  $5\text{mJ}/\text{cm}^2$  of  $1.3\text{nm}$  x-rays at a  $5\mu\text{m}$  mask-to-substrate gap. The postexposure hold time was 1.5 hours, and was followed by a one minute  $60^\circ\text{C}$  hotplate bake. Development time was 2.5 minutes in 1:1 AZ Developer and DI  $\text{H}_2\text{O}$ .

# Ray-PF exposed with $\text{Cu}_L$ ( $\lambda=1.3\text{nm}$ )



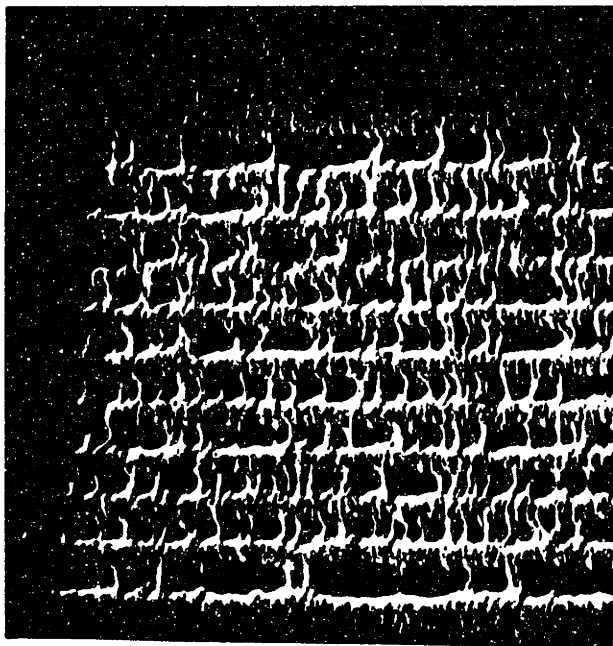
0.15 μm

0.1 μm

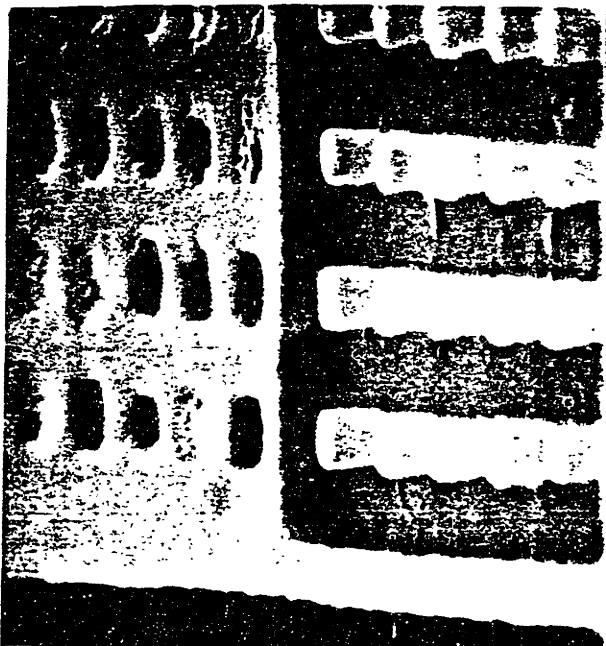
**Dose: 5.0mJ/cm<sup>2</sup>**  
**Film Thickness: 1.0 μm**

**Figure 3.6: Examples of surface induction layer effect in Ray-PN. This effect is usually only seen between closely spaced small features.**

# Surface Effect



↑ | ↓ 0.2μm  
pitch



↑ | ↓ 0.25μm

Observed in Ray-PN, Ray-PF,  
and SAL-601.

# Chapter 4

## Shot Noise

An interesting and important question to consider in assessing resolution limits is the effect of shot noise. A diffracted intensity pattern is arrived at via the classical description of light as a wave phenomenon. From the quantum mechanical viewpoint, the intensity pattern is proportional to the time averaged probability distribution of photons per unit area [64]. Shot noise is caused by the statistical nature of photons both emitted from the source and absorbed in the resist. The higher the sensitivity of the resist the more likely it is that the diffracted intensity will be inaccurately recorded due to the granularity of light. Thus, a lowering of image resolution is anticipated with increase in resist sensitivity. In this chapter resolution as a function of absorbed photon density is empirically determined. The minimum resolvable feature is then distinguished from the minimum *practical* feature size for manufacturing by fitting experimental data to the process latitude model developed by Smith [65,66].

I define a minimum resolvable (MR) pixel as having volume  $(LW)^2 \times h$  where  $LW$  is the minimum resolvable linewidth and  $h$  is the pixel height. This is shown schematically in Figure 4.1.

A  $1\mu\text{m}$ -thick film of Ray-PF, exposed with  $\text{Cu}_L$  x-rays ( $\lambda = 1.3\text{nm}$ ), has a calculated sensitivity of  $5\text{mJ}/\text{cm}^2$ . This is the most sensitive resist studied in this

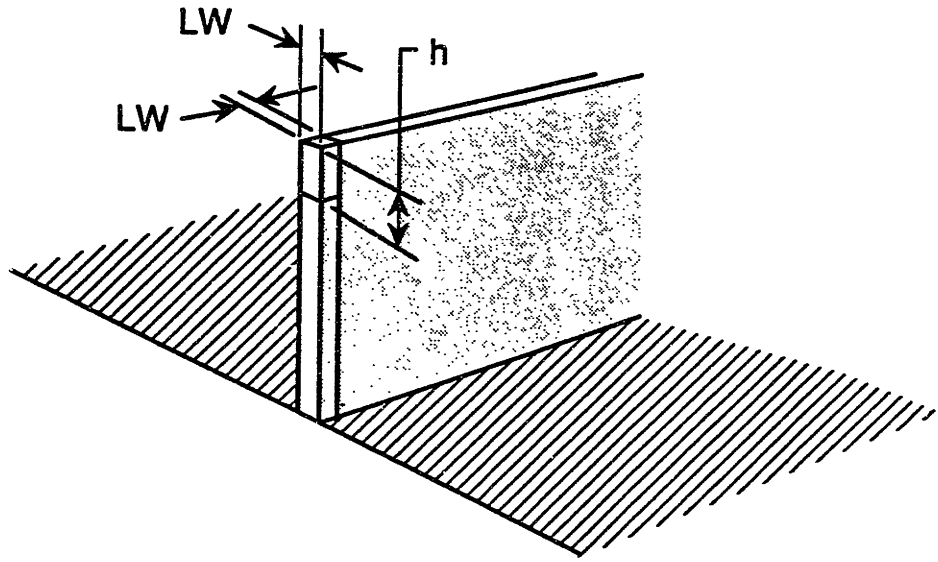


Figure 4.1: A single MR pixel of resist has height  $h$  and surface area  $(LW)^2$ , where  $LW$  is the minimum resolvable linewidth.

thesis and, using it,  $0.1\mu\text{m}$ -wide lines were patterned. The exposed lines, shown in Figure 3.5, are ragged as compared to the  $30\text{nm}$ -wide lines of PMMA in Figure 2.6. Close inspection of the Ray-PF lines shows that the noise in the vertical direction is of the order of  $\sim 20\text{nm}$  for each edge (i.e. a total of 40% of the linewidth) strongly suggesting that these are the finest lines resolvable in this resist. The number of photons per pixel is calculated as follows:

$$N = S \frac{(1 - T) A_{\text{pixel}}}{n_{\text{layers}} E_{\text{photon}}} \quad (4.1)$$

where  $S$  is the resist sensitivity (dose per unit area),  $E_{\text{photon}}$  is the photon energy,  $T$  is the fraction of x-rays transmitted through the resist,  $A_{\text{pixel}}$  is the pixel area, and  $n_{\text{layers}}$  is the number of layers of pixels in the resist film. For the exposure shown in Figure 3.5,  $S = 5\text{mJ}/\text{cm}^2$ ,  $E_{\text{photon}} = 925\text{eV}$ ,  $T=0.66$  ( $1.8\text{dB}/\mu\text{m}$ ),

$A = (100\text{nm})^2$ , and, assuming a pixel height of  $h=100\text{nm}$ ,  $n_{\text{layers}} = 10$  which yields 115 photons/pixel. Taking 115 photons/pixel as the empirical resolution limit based on shot noise, MR pixels for Ray-PN and PMMA can be calculated. These values are given in Table 4.1.

X-ray resist	Dose $\text{kJ/cm}^3$	linewidth, LW (nm)	photons per MR pixel
Ray-PF	0.017	100	115
Ray-PN	0.061	53	115
PMMA	1	13	115

Table 4.1: The calculated minimum resolvable linewidths for various doses of  $\text{Cu}_L$  x-rays.

In manufacturing of VLSI or ULSI memories, circuit reliability depends critically on uniformity of device performance which in turn is strongly influenced by uniformity of device dimensions. The maximum allowable lithographic tolerance for MOS gate widths is  $\pm 10\%$ . For this reason Smith [65], in quantifying process latitude, defines a pixel as having area  $\epsilon^2$  and height  $h$  where  $\epsilon$  is one tenth the minimum linewidth as shown in Figure 4.2. To distinguish this pixel from the MR pixel I will call it a  $\epsilon^2$  pixel.

Because the volume influenced by a single absorbed photon should be roughly spherical, it is tempting to define both MR and  $\epsilon^2$  pixels as cubes, but the developer percolates through the resist so that a pixel will be removed even if the energy dose is unevenly distributed within the pixel volume. Consequently, the pixel is defined as a parallelepiped with  $h$  chosen independent of  $\epsilon$ .

An expression for the minimum number of photons per  $\epsilon^2$  pixel required to insure that the pixel develops has been derived [66] as follows: The mean number of photons per pixel,  $\bar{N}(x)$  (considered in one dimension for simplicity), varies as a



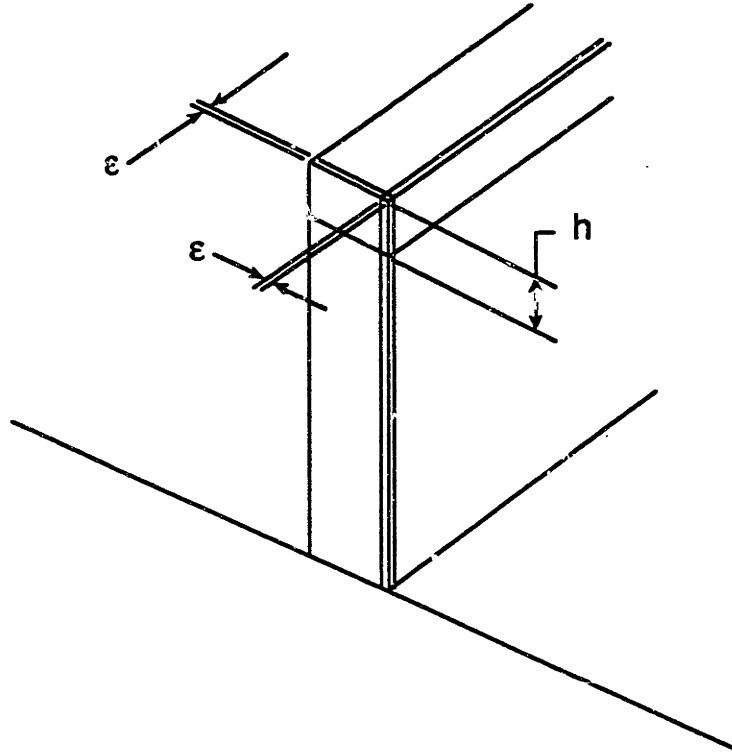


Figure 4.2: An  $\epsilon^2$  pixel with height  $h$  and area  $\epsilon^2$  where  $\epsilon = LW/10$ .

function of position due to fluctuations in intensity as shown in Figure 4.3.  $\bar{N}_{\max}$  and  $\bar{N}_{\min}$  are the maximum and minimum mean numbers of photons per pixel.  $\bar{N}_m$  corresponds to the mean number of photons that will cause a pixel to develop and  $\delta N$  is the development band. All pixels with doses that lie within  $\delta N$  will partially develop; pixels with higher doses will fully develop; and pixels with lower doses will be undeveloped.

Using the contrast function [67]

$$K = \frac{I_{\max} - I_{\min}}{I_{\max} + I_{\min}} \quad (4.2)$$

and assuming that

$$\bar{N}_m = \frac{1}{2}(\bar{N}_{\max} + \bar{N}_{\min}) \quad (4.3)$$

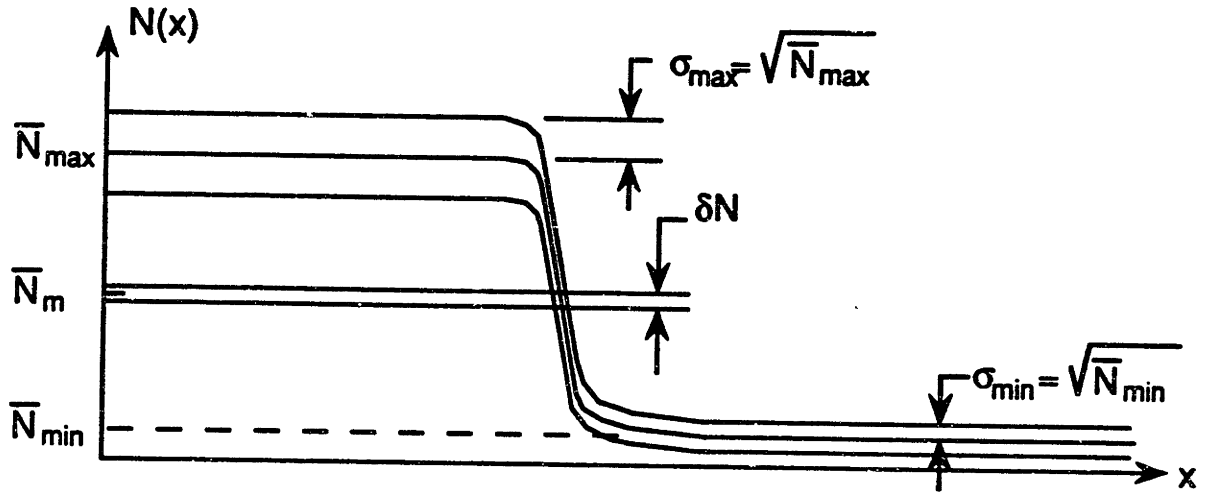


Figure 4.3: The mean number of photons per pixel,  $\bar{N}(x)$ , is proportional to intensity and varies with position as shown. The development band,  $\delta N$ , is centered about  $\bar{N}_m$ , the mean number of photons required to develop a pixel. For purpose of analysis,  $\bar{N}_m$  is assumed to lie midway between  $\bar{N}_{max}$  and  $\bar{N}_{min}$  [65,66].

the requirement on  $\bar{N}_{max}$  is found to be [66]

$$\bar{N}_{max} > \frac{n^2(1+K)^2}{K^2 [1 - \delta N / (2K\bar{N}_m)]^2} \quad (4.4)$$

For Ray-PF the quantity  $\delta N / \bar{N}_m$  can be calculated from e-beam data in Figure 2 of reference [60]. An abrupt transition from no development to complete development of a 100nm film thickness occurs for a  $0.5\mu\text{C}/\text{cm}^2$  change in dose at a dose of  $\sim 9.5\mu\text{C}/\text{cm}^2$ . Based on these numbers  $\delta N / \bar{N}_m = 0.05$ . With  $K=0.82$ , which corresponds to 10dB mask absorber attenuation, Ray-PF requires  $\bar{N}_{max} \geq 5.3n^2$ . Keeping  $h=100\text{nm}$ , for a dose of  $5\text{mJ}/\text{cm}^2$  and  $n=1$  the  $\epsilon^2$  pixel dimension is 21nm which is in good agreement with the visual estimate of edge roughness from Figure 3.5. Since we have assumed a high value of contrast and have assumed that  $\bar{N}_m$

falls at the mean between  $\bar{N}_{\max}$  and  $\bar{N}_{\min}$ , the calculated  $\bar{N}_{\max}$  must be understood as an optimistic estimation of minimum manufacturing linewidth.

The minimum acceptable contrast for manufacturing is  $K=0.5$  and, for proximity printing, local contrast will vary as a function of position due to diffraction. In addition, the field intensity incident on the mask will not be perfectly uniform. The result is that  $\bar{N}_m$  can be above or below the mean value assumed in Equation 4.3. The effect of variation in position of  $\bar{N}_m$  can be included by taking a larger value for  $\delta N$  where  $\delta N$  is now understood to include the development band plus the tolerance on  $\bar{N}_m$ . Calculated values for minimum manufacturing linewidth ( $LW = 10 \times \epsilon$ ) are given in Table 4.2 for  $\delta N/\bar{N}_m = 0.05$  and  $0.25$  and for  $K=0.82$  and  $0.5$ . Note that tightening the tolerance by requiring a confidence level of two standard deviations (i.e.  $n=2$ ) will quadruple the minimum linewidth. But due to action of the developer  $n=1$  is considered sufficient.

X-Ray Resist	Minimum Linewidth for Manufacturing, nm			
	$\delta N/\bar{N}_m = 0.05$		$\delta N/\bar{N}_m = 0.25$	
	$K=0.82$	$K=0.5$	$K=0.82$	$K=0.5$
Ray-PF	210	290	240	370
Ray-PN	110	160	130	200
PMMA	28	38	32	48

Table 4.2: Calculated minimum linewidths for manufacturing for Ray-PF, Ray-PN, and PMMA.

From this analysis we find that to image 50nm lines for a ULSI chip with a wavelength of 1.3nm will require a resist that is as insensitive as PMMA. The sensitivity can be increased while maintaining an acceptably low level of shot noise only by lowering the photon energy. This might be done by using a diamond mask membrane which transmits  $C_K$  radiation ( $E_{\text{photon}} = 283\text{eV}$ ,  $\lambda = 4.5\text{nm}$ ). But this

increase in wavelength would require approximately halving the gap between the mask and wafer, essentially requiring true contact printing.

# Chapter 5

## Diffraction: Theory and Simulations

The prime contributor to loss of resolution in proximity printing is diffraction. The experiment presented in Chapter 2 showed that, contrary to previously held view on the effect of photoelectron range, resolution down to 30 nm is achievable for  $0.8 \leq \lambda \leq 4.5$  nm. In this chapter, we utilize diffraction theory to explore resolution as a function of gap for linewidths in the range of  $\sim 0.2 \leq W \leq 0.5$   $\mu\text{m}$ . For monochromatic illumination, the gap at which a linewidth is imaged can be written as [27,68,69]

$$G = \alpha W^2 / \lambda \quad (5.1)$$

where  $\alpha$  can be recognized as the inverse of the more familiar Fresnel number

$$1/\alpha = W^2 / (\lambda G) \quad (5.2)$$

Using qualitative criteria, various researchers have estimated the maximum acceptable  $\alpha$  for proximity printing to be  $0.22 \leq \alpha_{\text{max}} \leq 0.54$  [27,68,70,71].

Lin [72] attempts to identify useful gaps, or working distances, for proximity printing, each with an associated depth of focus, through a comparison of the irradiance patterns of five different features (lines, spaces, gratings, islands, and

lakes). The criteria used is that the irradiances in the diffracted images of the five features, calculated at the object linewidth  $\pm 10\%$ , must provide a region of overlap. Put more simply, he asks that all mask features be reproducible in the image plane to within  $\pm 10\%$  of the object size. His simulations, and also those of Guo et al. [73], of log of exposure versus gap for the five features, indicate that  $\alpha_{\max} = 0.2$ . For the more restricted case of just the three long features (lines, spaces, and gratings), Lin's simulations suggest that  $\alpha_{\max}$  can be increased to 0.4. Guo et al. [73] have done simulations for a mask biasing scheme whereby mask dimensions are uniformly changed to provide a degree of compensation for diffraction effects. Their study indicates that  $\alpha_{\max} = 0.3$  is acceptable if all five features are considered.

In a more recent study [74], Guo and Cerrina show that source spatial incoherence plays an important role in increasing the maximum usable gap. They show that by properly engineering the effect of source blurring  $\alpha_{\max}$  can be increased to 0.5 for unbiased features or to 0.9 for biased features, a dramatic improvement over the previous 0.2 to 0.3 estimates.

The criteria introduced by Lin, of reproducibility of five features to within  $\pm 10\%$  of the mask dimensions, is useful in that it provides a figure of merit for comparing different systems as he has done with DUV and x-ray, but it is quite conservative. While it is true that manufacturing processes cannot tolerate more than  $\pm 10\%$  linewidth variation, the five features chosen for comparison do not correspond to a normal manufacturing situation. Typically, the minimum dimension corresponds to only one feature, for example, the gate length in MOS circuitry.

In the theoretical studies in references [72-75], the effect of diffraction on linewidth is quantified with gap-exposure diagrams in which log of exposure is plotted along the abscissa and gap is plotted along the ordinate. A plot for a given feature shows a family of curves each corresponding to the diffracted linewidth plus or minus some percentage of its width. The maximum acceptable gap, or  $\alpha_{\max}$ , is

determined by an overlap of plots for the various features that include a tolerance of  $\pm 10\%$ .

Gap variation as a function of irradiance is difficult to measure experimentally because it requires many separate exposures. An experiment which is both efficient and effective is to measure linewidth variation as a function of gap for a given x-ray dose. This can be done by exposing a pattern onto a sloped wall so that data for all gaps of interest is obtained in a single exposure. The absorbed dose corresponds to a particular irradiance clipping level. Difficulties that plague multiple exposure experiments, such as variation in resist processing and development, and possible source intensity drift between exposures, are eliminated. A single exposure, multiple gap experiment cannot directly answer the question of the correct gap to use; rather, it provides a wealth of data for calibrating a simulator and can give an indication of how well standard diffraction theory, utilizing Kirchhoff boundary conditions models the case of near field x-ray diffraction through a lossy dielectric. Such an experiment is presented in Chapter 6. With this in mind, we have generated linewidth-gap plots where the abscissa is gap, the ordinate is diffracted linewidth, and the family of curves are for various irradiance clippings.

Among the approaches that have been used to model near field diffraction effects are the exact Kirchhoff integral [72,75,76], the Fresnel paraxial approximation [70,77,78], and the angular spectrum of plane waves (ASPW) [73,79,80]. Since it is amenable to fast Fourier transform (FFT) methods, and because it is more precise than the Fresnel approximation, the ASPW was chosen for use in this thesis.

## 5.1 The Angular Spectrum of Plane Waves

The proximity printing set-up for which we wish to simulate diffraction is depicted in Figure 5.1 where the mask plane is labeled  $\Sigma_m$  and the image plane (the

substrate) is called  $\Sigma_{ss}$ . We assume Kirchhoff boundary condition; i.e. both the scalar field and its derivative are assumed to be zero outside the aperture area. In the plane immediately downstream of the mask, the field beneath the absorber is phase shifted and exponentially attenuated in accordance with the attenuation curve give in Figure 2.5.

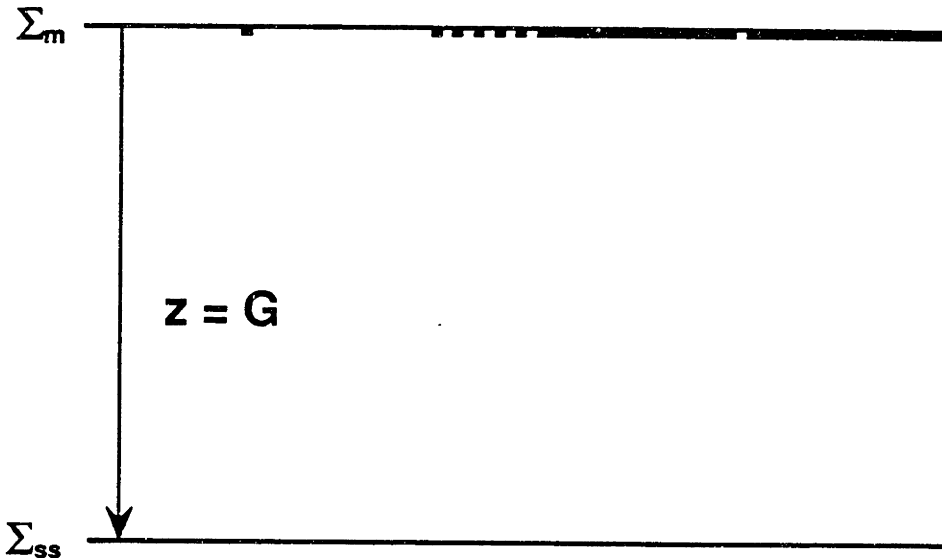


Figure 5.1: Depiction of diffraction situation for x-ray proximity printing:  $\Sigma_m$  is the mask plane;  $\Sigma_{ss}$  is the image plane.

Use of Kirchhoff boundary conditions, which are heuristic and are known to violate Maxwell's equations, has proved satisfactory in predicting diffraction patterns in a wide variety of problems [81]. Nevertheless, they may be inadequate for correctly modeling proximity printing where the mask absorber is a lossy dielectric, hundreds of wavelengths thick, and where the absorber thickness is comparable to the width of the diffracting feature. Using full electromagnetic vector theory and finite element analysis on a Cray-2 supercomputer, Schattenburg et al. [44] have investigated diffraction in the vicinity of a 30 nm-wide line for 50 to 80 nm-



thick absorbers for  $\lambda = 4.5$  nm. For these small structures, strong fringing fields are seen in the shadow of the absorber immediately downstream of the mask, in violation of the Kirchhoff boundary conditions. Solutions for larger structures and shorter wavelengths are unknown at present. For this reason we use the Kirchhoff formalism in spite of its possible inadequacy for our problem.

If the field at the mask plane is  $U_0(x_m, y_m)$ , from the Fourier transform pair

$$\mathcal{F}(g(x, y)) = G(f_x, f_y) \quad (5.3)$$

$$g(x, y) \longleftrightarrow G(f_x, f_y) \quad (5.4)$$

the angular spectrum of plane waves is given by [79]

$$A_0(f_x, f_y) = \int \int_{-\infty}^{\infty} U_0(x, y, 0) \exp[-j2\pi(f_x x + f_y y)] dx dy \quad (5.5)$$

where  $f_x$  and  $f_y$  are the spatial frequencies (i.e. components of the  $\mathbf{k}$  vector) in the  $x$  and  $y$  directions. The diffracted scalar field is obtained from [79]

$$U(x, y, z) = \int \int_{-\infty}^{\infty} A_0(f_x, f_y) \exp\left(j2\pi \frac{z}{\lambda} \sqrt{1 - (\lambda f_x)^2 - (\lambda f_y)^2}\right) \times \exp[j2\pi(f_x x + f_y y)] df_x df_y \quad (5.6)$$

where

$$H(f_x, f_y) = \exp\left[j2\pi \frac{z}{\lambda} \sqrt{1 - (\lambda f_x)^2 - (\lambda f_y)^2}\right] \quad (5.7)$$

is the transfer function which describes propagation through free space for values of  $f_x^2 + f_y^2 < 1/\lambda$ . We are sufficiently far from the mask so that evanescent waves are inconsequential, so for  $f_x^2 + f_y^2 > 1/\lambda$ ,  $H_0(f_x, f_y) = 0$ .

For the case of lines, spaces, and gratings, Equations 5.5 and 5.6 reduce to

$$A_0(f_x) = \int_{-\infty}^{\infty} U_0(x, 0) \exp[-j2\pi(f_x x)] dx \quad (5.8)$$

and

$$U(x, G) = \int \int_{-\infty}^{\infty} A_0(f_x) \exp\left(j2\pi \frac{G}{\lambda} \sqrt{1 - (\lambda f_x)^2}\right) \exp[j2\pi f_x x] df_x \quad (5.9)$$

where  $G$  is the mask to substrate gap.

Line	Energy (eV)	$\lambda$ (nm)	intensity
$L_{\alpha_{1,2}}$	927.9	1.336	100
$L_{\beta_1}$	949.8	1.3053	75
$L_{\beta_{3,4}}$	1022.8	1.2122	4
$L_{\alpha_{1,2}}$	811.1	1.5286	3

Table 5.1: The lines of the  $\text{Cu}_L$  spectrum with their relative intensities from references [85,86].

## 5.2 Spatial Incoherence

The x-ray source to be simulated is the  $\text{Cu}_L$  line, which actually consists of several lines with energies, wavelengths, and relative intensities given in Table 5.1. A single line will typically have a bandwidth of  $\sim 1$  eV [82,83]. The coherence length, calculated from the two main lines which are separated by 22 eV, is approximately 60 nm. The x-rays are generated from an electron bombardment point source where the focal spot size is unknown but is crudely estimated to have a diameter between 1 and 2 mm. While the source is both temporally and spatially incoherent, spatial incoherence dominates. The discussion of source incoherence presented below closely follows the treatment given by Goodman in reference [84].

Mathmatically, temporal and spatial incoherence effects are described by the mutual coherence function. For quasimonochromatic spatially incoherent light, the mutual coherence function can be replaced by the time independent mutual intensity function provide the following two conditions are met [84]:

$$\Delta\nu \ll \bar{\nu} \tag{5.10}$$

where  $\bar{\nu}$  is the mean optical frequency and  $\Delta\nu$  is the bandwidth. Also, all image

points of interest and all source points must satisfy

$$|[(r_2 + r'_2) - (r_1 + r'_1)]/c| \ll \tau_c \quad (5.11)$$

where  $\tau_c$  is the coherence time and  $r_1$ ,  $r'_1$ ,  $r_2$ , and  $r'_2$  are defined in Figure 5.2.

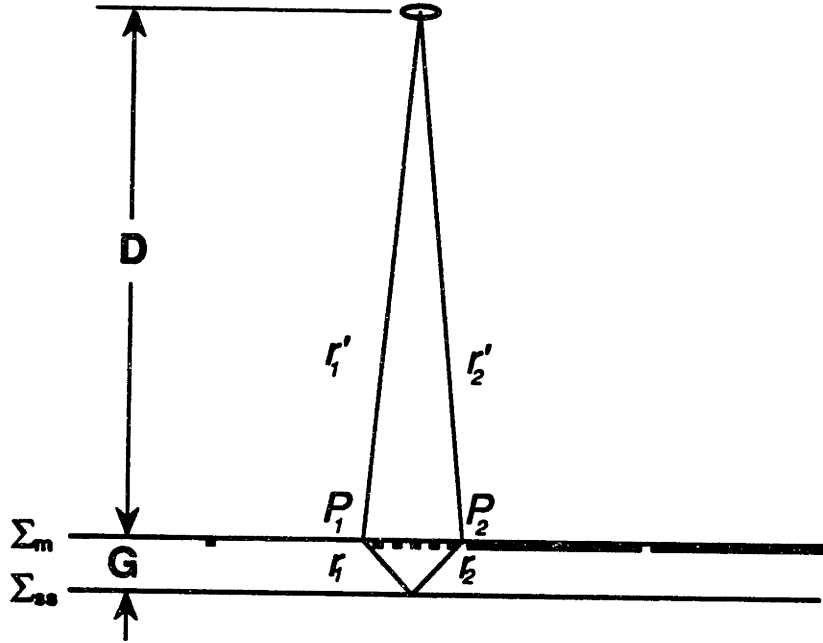


Figure 5.2: Illustration of the pathlength difference for two rays traced from a point on the extended source to a point on the image plane. For the experiment modeled here,  $D = 50$  cm,  $d = 1$  mm, and  $5 \leq G \leq 100$   $\mu\text{m}$ .

Equation 5.10 is satisfied by the  $\text{Cu}_L$  line source. In considering the requirement expressed in Equation 5.11, we first note that the source to mask distance is 50cm so that  $r'_1 \simeq r'_2$  and Equation 5.11 reduces to  $|(r_1 - r_2)/c| \ll \tau_c$ . The widest linewidth simulated is  $0.5$   $\mu\text{m}$ . For isolated lines or spaces, the diffraction area of interest is contained within a  $1$   $\mu\text{m}$  width on the substrate. With a source coherence length of only  $\sim 60$  nm, Equation 5.11 is not satisfied. Nevertheless, we model the source as quasimonochromatic throughout the gap range  $5 \leq G \leq 100$   $\mu\text{m}$  for all feature sizes.

Propagation of the mutual intensity is described by the Van Cittert-Zernike theorem [84]:

$$\mathbf{J}(x_{m_1}, y_{m_1}; x_{m_2}, y_{m_2}) = \frac{\kappa e^{-j\psi}}{(\lambda z)^2} \int_{-\infty}^{\infty} I(x_s, y_s) \exp \left[ j \frac{2\pi}{\lambda z} (\Delta x_m x_s + \Delta y_m y_s) \right] dx_s dy_s \quad (5.12)$$

where  $I(x_s, y_s)$  is the intensity at the source,  $\kappa$  is a scaling factor. The terms in the exponent under the integral in Equation 5.12 are defined as

$$\Delta x_m = x_{m_2} - x_{m_1} \quad \text{and} \quad \Delta y_m = y_{m_2} - y_{m_1} \quad (5.13)$$

and

$$\psi = \frac{\pi}{\lambda z} [(x_{m_2}^2 + y_{m_2}^2) - (x_{m_1}^2 + y_{m_1}^2)] \quad (5.14)$$

where  $(x_{m_1}, y_{m_1})$  and  $(x_{m_2}, y_{m_2})$  correspond to points  $P_1$  and  $P_2$  in Figure 5.2. Neglecting scaling constants and a phase factor, the propagated mutual intensity is found to be simply the Fourier transform of the intensity distribution across the source. If, for example, our source intensity distribution can be described by a gaussian, then, neglecting the scaling and phase factor, the mutual intensity at the mask plane,  $\Sigma_m$ , will also be a gaussian:

$$\frac{1}{2\pi\sigma_s^2} \exp \left[ -\frac{(x_s^2 + y_s^2)}{\sigma_s^2} \right] \longleftrightarrow \exp \left[ -2\pi^2\sigma_s^2 (f_{\Delta x_m} + f_{\Delta y_m}) \right] \quad (5.15)$$

where

$$f_{\Delta x_m} = \frac{\Delta x_m}{\lambda D} \quad \text{and} \quad f_{\Delta y_m} = \frac{\Delta y_m}{\lambda D} \quad (5.16)$$

For the case of a gaussian source, the normalized mutual intensity, called the complex coherence factor, is

$$\begin{aligned} \mu(x_{m_1}, y_{m_1}; x_{m_2}, y_{m_2}) &= e^{-j\psi} \exp \left[ -2\pi^2\sigma_s^2 (f_{\Delta x_m} + f_{\Delta y_m}) \right] \\ &= e^{-j\psi} \mu(\Delta x_m, \Delta y_m) \end{aligned} \quad (5.17)$$

In the Fraunhofer limit, propagation of partially coherent light is governed by Schell's theorem [84]

$$I(x_{ss}, y_{ss}) \simeq \frac{I_0}{(\lambda z)} \int \int_{-\infty}^{\infty} \mathcal{P}(\Delta x_m, \Delta y_m) \mu(\Delta x_m, \Delta y_m) \times \exp \left[ j \frac{2\pi}{\lambda z} (x_s \Delta x_m + y_s \Delta y_m) \right] d\Delta x_m d\Delta y_m \quad (5.18)$$

where

$$\mathcal{P} = \int \int_{-\infty}^{\infty} \mathbf{P} \left( \bar{x}_m - \frac{\Delta x_m}{2}, \bar{y}_m - \frac{\Delta y_m}{2} \right) \times \mathbf{P}^* \left( \bar{x}_m + \frac{\Delta x_m}{2}, \bar{y}_m + \frac{\Delta y_m}{2} \right) d\bar{x}_m d\bar{y}_m \quad (5.19)$$

The function  $\mathcal{P}$ , called the complex pupil function, is simply the angular spectrum of plane waves in the mask plane. The terms in the argument of  $\mathbf{P}$  are defined as

$$\bar{x}_m = \frac{1}{2}(x_{m_2} + x_{m_1}) \quad \text{and} \quad \bar{y}_m = \frac{1}{2}(y_{m_2} + y_{m_1}) \quad (5.20)$$

$$\Delta x_m = x_{m_2} - x_{m_1} \quad \text{and} \quad \Delta y_m = y_{m_2} - y_{m_1} \quad (5.21)$$

Note that to simplify the problem, the phase term,  $e^{-j\psi}$ , from the complex coherence factor has been dropped in Equation 5.18. Only the modulus is retained. If  $\mu(\Delta x_m, \Delta y_m) = 1$ , then Equation 5.18 is equivalent to the monochromatic diffracted intensity pattern in the Fraunhofer regime. Thus, partial incoherence is modeled as a convolution of the monochromatic intensity pattern with the Fourier transform of the modulus of the complex coherence factor.

In x-ray proximity printing, we are not operating in the Fraunhofer regime. Nevertheless, we model the effect of our source as a convolution of the transform of  $\mu(\Delta x_m, \Delta y_m)$  with the monochromatic Fresnel regime diffracted intensity. This is heuristic rather than rigorous.

We model our source, in one dimension, as having a gaussian profile with FWHM = 1 mm so that at the mask plane,  $\Sigma_m$ , we have

$$\mu(\Delta x_m) = \exp \left[ -2\pi^2 \sigma_s^2 f \Delta x_m \right] \quad (5.22)$$

where

$$f_{\Delta x_m} = \frac{\Delta x_m}{\lambda D} \quad (5.23)$$

and  $\sigma_s^2$  is the variance of the source gaussian. The Fourier transform of  $\mu(\Delta x_m)$  is

$$\mathcal{F}[\mu(\Delta x_m)] = \frac{1}{\sqrt{2\pi\sigma_m^2}} \exp[-2\pi^2\sigma_s^2 f_{x_{ss}}] \quad (5.24)$$

where

$$f_{x_{ss}} = \frac{\Delta x_m}{\lambda G} \quad (5.25)$$

It is this function, Equation 5.24, that is convolved with the calculated intensity pattern.

The standard deviation of  $\mu(\Delta x_m)$  at the substrate is related to the standard deviation of the assumed source profile by

$$\sigma_{ss} = \lambda G \sigma_m = \sigma_s \frac{G}{D} \quad (5.26)$$

The size relationship between  $\sigma_m$  and  $\sigma_{ss}$  is the same as that found between the source and the penumbral blur using ray tracing

$$\delta = d \frac{G}{D} \quad (5.27)$$

where  $d$  is the source size and  $\delta$  is the penumbral blur at the image plane. What is commonly called penumbral blur in x-ray lithography is simply a crude measure of the spatial incoherence of the source.

### 5.3 Simulations

Diffraction simulation programs, written in C, were put together by a UROP student, Dan Olster, under my supervision, utilizing FFT subroutines from *Numerical Recipes* [87]. Irradiance distributions were calculated using 2048 data points along the  $x$ -axis. Lines and spaces were simulated with 40 data points within the feature; a single grating period was modeled with 128 points. In all simulations, the

irradiance is normalized to the irradiance at the substrate in the absence of a mask absorber pattern.

To gauge the ability of the simulator to model diffraction effects for proximity printing, we compare calculated irradiance patterns with an x-ray exposure in Figure 5.3. The x-ray exposure, in PMMA resist, was made using a  $1\ \mu\text{m}$ -period grating at a  $30\ \mu\text{m}$ -gap. The dip seen in the intensity pattern is manifest in the developed image. In the high intensity region where the resist is partially developed away, the resist at the middle has developed more slowly. Two simulations are shown. The diffraction pattern for a vertical walled absorber shows a substantial dip in intensity at  $x = 0$ ; for the case of an absorber with  $20^\circ$  sloped-walled absorber, the dip is substantially reduced. The mask used in this exposure was made by Mark Schattenburg using a lift-off technique for patterning the  $\sim 0.5\ \mu\text{m}$ -thick gold absorber; this technique leads to nonvertical sidewalls. Thus, the simulation for a sloped-wall absorber more closely matches the exposure conditions.

Direct evidence of coherent effects such as the bump seen in this exposure are generally not seen in x-ray exposures. The reason for this is that the x-ray dose for an exposure like the one shown in Figure 5.3 is usually targeted to clip the intensity pattern below the dip. To record the intensity dip, the sample was underexposed and developed for 3 minutes in pure MIBK developer. This has the effect of reducing the contrast of the resist. Even so, the effect is weak. In the simulations shown in Figure 5.3, the gaussian source was modeled as having a FWHM of 1 mm; the source-to-substrate distance,  $D$ , was 50 cm, the same distance as was used during the exposure. The source size is typically based on a visual estimate of the visible radiation focal spot seen when focusing the x-ray target. The relation of the visible source size to the x-ray source size is unknown. In Figure 5.4, the effect of increasing the source size is illustrated for the vertical and sloped walled absorbers. The diffraction patterns in (a) and (c) of Figure 5.4, appear to be in better agreement with the exposure shown in Figure 5.3; for this

reason, a FWHM of 2 mm was used for the simulations. The arguments for using a source with FWHM = 2 mm was further bolster by an experiment discussed below.

The effect of source incoherence can be made to completely dominate image formation at the substrate plane by setting  $\delta = dG/D$  to a large value. Because exposure time is inversely proportional to image intensity, and since the edge of a developed resist line corresponds to a fixed x-ray dose, a number of exposures of different time durations can be used to reconstruct an intensity pattern [88]. If the mask pattern is a slit and  $\delta = dG/D$  is large enough so that diffraction is negligible compared to the effect of source incoherence, then the reconstructed intensity profile will correspond to the modulus of the complex coherence factor convolved with the intensity through the slit.

Figure 6.5 shows experimental data superimposed on a convolution of the intensity from a 90  $\mu\text{m}$ -wide slit with a gaussian. The gaussian FWHM was calculated for the experimental source-to-mask distance of 5.45 cm, a gap of 0.15 cm, and an assumed one-dimensional source FWHM=2 mm. The 90  $\mu\text{m}$ -wide slit was an opening in a TEM grid that was glued to a nitride membrane. The data points are the measured width of the slit image, in PMMA resist, for the exposure times listed in Table 5.2. For each exposure, developer temperature and strength, as well as development time, were kept constant. To normalize the intensity values, it was assumed that an image width equal to the mask slit width corresponded to the 0.5 value of intensity. Even though the true source is two dimensional, the experimental data lends credence to the simple one dimensional model used in the diffraction calculations.

Figures 5.7 through 5.18 are plots of equi-irradiance curves for lines, spaces, and gratings of nominal 0.2, 0.3, 0.4, and 0.5  $\mu\text{m}$ -linewidth. The simulations are for the actual line and space widths measured from the mask used in the experiment rather than for the nominal widths. The measured widths are listed



Exposure Time (min)	$C_0$ /Time	Resist Image Width ( $\mu\text{m}$ )
25	0.50	86
29	0.43	104
40	0.31	116
67	0.19	130
100	0.13	142

Table 5.2: Exposure times and measured image width, in PMMA resist, of a 92  $\mu\text{m}$ -wide slit exposed at a 1.5 mm gap and a 5.45  $\mu\text{m}$  source-to-mask separation.  $C_0$  is a scaling constant used to normalize the intensity.

in Table 5.3. Figure 5.6 shows SEMs of the nominal 0.2  $\mu\text{m}$  mask features along with a cross section of the mask which was broken after the last exposure. The rough, gold absorber is  $\sim 0.25 \mu\text{m}$ -thick. In the simulations, which include effects of both attenuation and phase shift, plots are shown for both 0.25 and 0.5  $\mu\text{m}$ -thick absorbers.

Breaks in equi-irradiance curves, seen in Figure 5.7 through 5.18, occur for gaps at which constructive interference effects cause the diffraction pattern to have multiple crossings and also at gaps for which no crossing is found. For example, in Figure 5.3 (b), for a normalized intensity value of 1 the diffraction pattern has multiple crossings within the symmetric half-period (0 to 500 nm), and, for a normalized intensity value of 0.1, the diffraction pattern has no crossings.

Important differences are seen in the linewidth-gap plots for the two absorber thickness. The 0.5  $\mu\text{m}$ -thick absorber provides 24 dB attenuation; 0.25  $\mu\text{m}$  of Au provides 12dB attenuation and a phase shift of  $-162^\circ$ . In Figures 5.19 and 5.20, diffraction patterns for the 0.4  $\mu\text{m}$ -period grating with 0.17  $\mu\text{m}$ -wide spaces are shown for the two gold thicknesses at a number of gaps. Note that, due to the

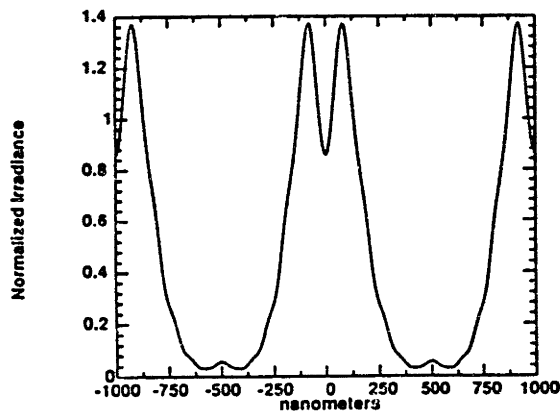
Nominal Linewidth ( $\mu\text{m}$ )	Actual Spacewidth ( $\mu\text{m}$ )	Actual Linewidth ( $\mu\text{m}$ )
0.2	0.17	0.23
0.3	0.25	0.35
0.4	0.38	0.42
0.5	0.48	0.52

**Table 5.3:** The listed linewidths and spacewidth, measured in the SEM on the x-ray mask, were used in generating the plots shown in Figures 5.6 through 5.17.

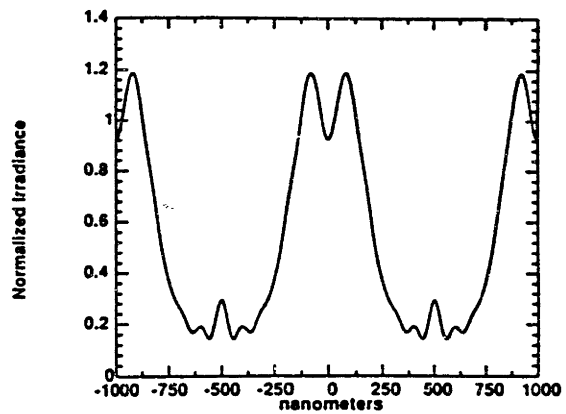
partial transmission and phase shift through the absorber, interference effects are much stronger for the 0.25  $\mu\text{m}$  Au thickness. At a 40  $\mu\text{m}$ -gap, the pattern for the thinner absorber has reached spatial frequency doubling.

For the 12 dB absorber, the number of plottable equi-irradiance curves is reduced and the number of breaks in the curves is increased, indicating reduced process latitude and reduced maximum usable gap. This is due to the increased transmission through the absorber and the associated phase shift which leads to the build up of lobes in the low intensity portions of the diffraction pattern. A greater percentage change in linewidth with change in gap is seen for the the thinner absorber. At small gaps, the equi-irradiance curves are more tightly bunched and, at large gaps, diverge more than in the case of the thicker 24 dB absorber. For both absorber thicknesses, oscillations in linewidth with gap are pronounced for small features; for large features, the oscillations represent a smaller fraction of the total linewidth and are further washed out, at large gaps, by the source spatial incoherence. In Chapter 6, these simulations will be compared, both qualitatively and quantitatively, to experimental measurements.

Figure 5.3: Diffraction patterns for a 1  $\mu\text{m}$ -period grating with (a) vertical absorber walls and (b) 20° sloped walls are compared with an x-ray exposure in PMMA made using a mask with sloped wall absorber. Cross section and aerial views of the exposure are seen in (c) and (d).



(a)

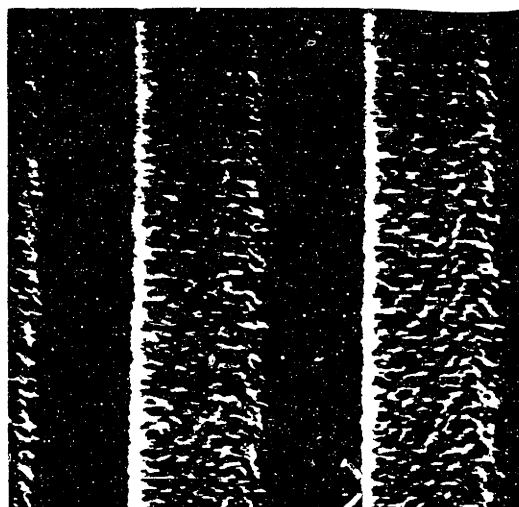


(b)



→ | ← 1.0 μm

(c)



← 1.0 μm →

(d)

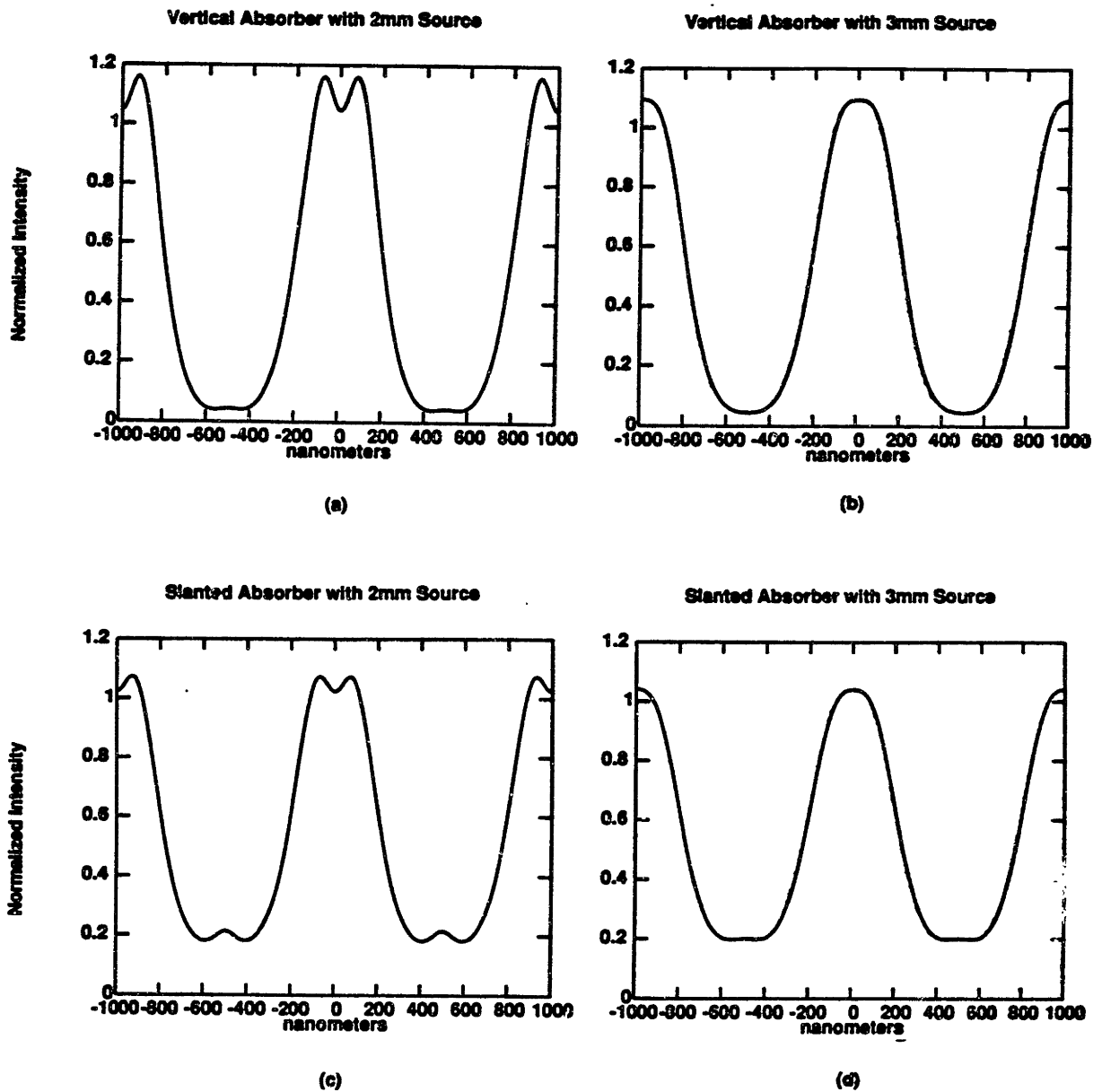


Figure 5.4: Diffraction patterns for a  $1\ \mu\text{m}$ -period grating with: (a) vertical absorber walls with a 2 mm source; (b) vertical absorber walls with a 3 mm source; (c)  $20^\circ$  sloped walls with a 2 mm source; (d)  $20^\circ$  sloped walls with a 3 mm source.

Penumbra! Blur, FWHM=60mu

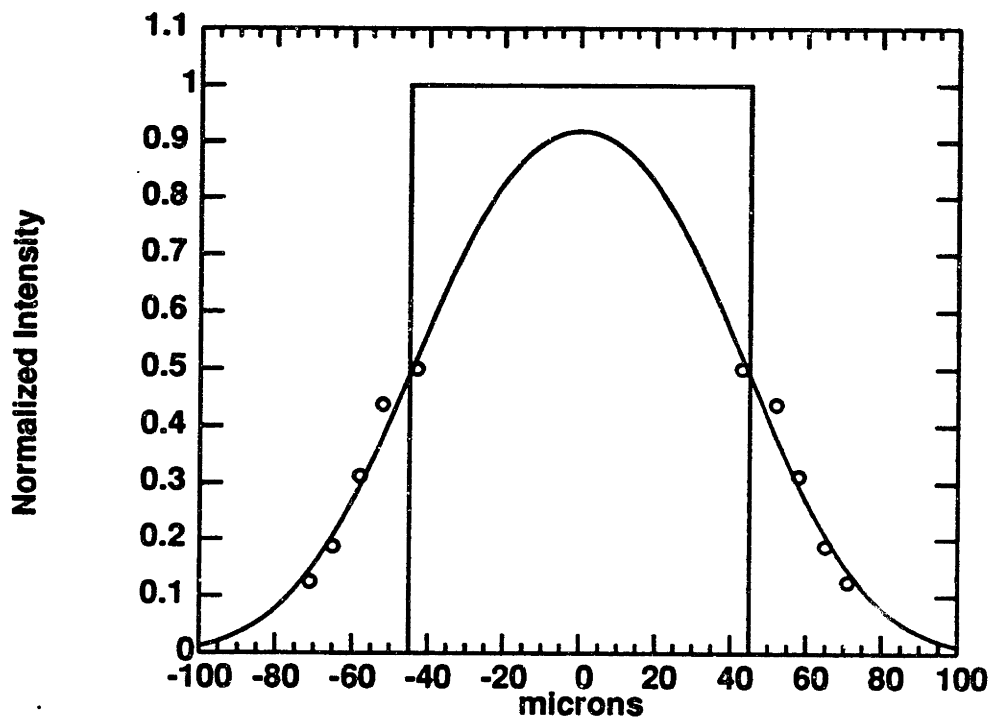
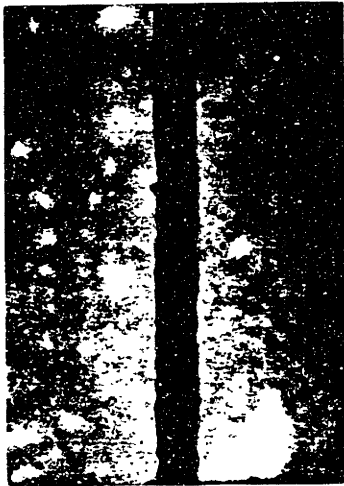


Figure 5.5: The convolution of a gaussian with FWHM = 60  $\mu\text{m}$  with a 90  $\mu\text{m}$ -wide slit. The data points are for the exposures listed in Table 5.2. The corresponding source has FWHM=2 mm.

**Figure 5.6: SEM's (a) to (c) of nominal  $0.2\ \mu\text{m}$  mask features. The actual dimensions are  $0.17\ \mu\text{m}$  spaces and  $0.23\ \mu\text{m}$  lines. The SEM in (d) is a cross section of the membrane that was used in diffraction experiments.**



→ | | ← 0.17  $\mu\text{m}$

(a)



→ | | ← 0.4  $\mu\text{m}$

(b)



→ | | ← 0.23  $\mu\text{m}$

(c)



↓  
0.25  $\mu\text{m}$   
↑  
1.6  $\mu\text{m}$   
↓

(d)



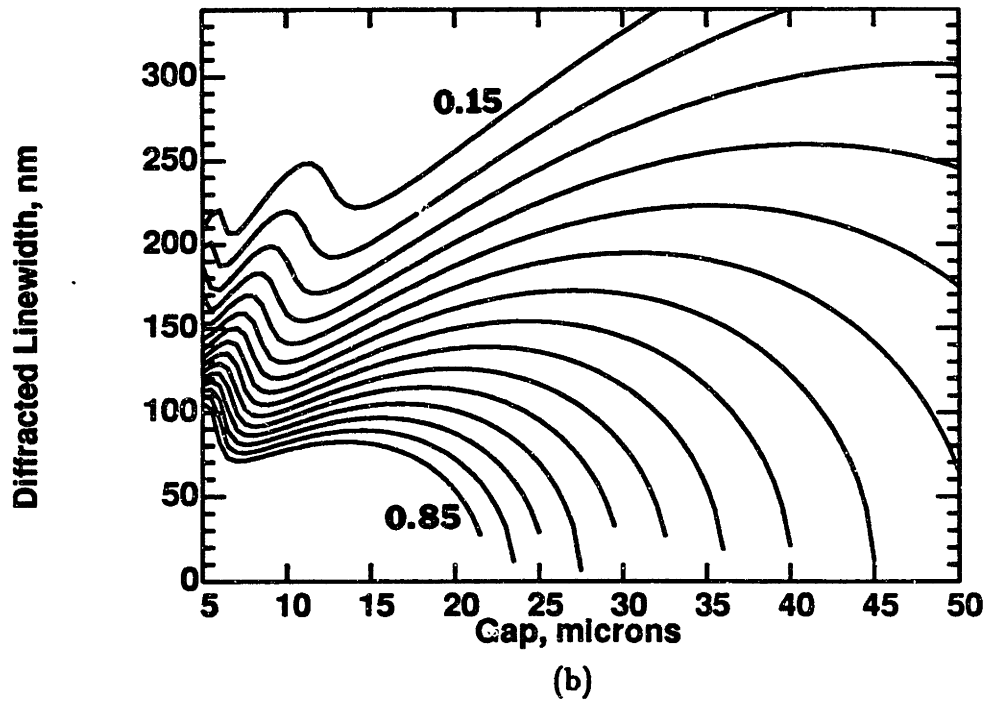
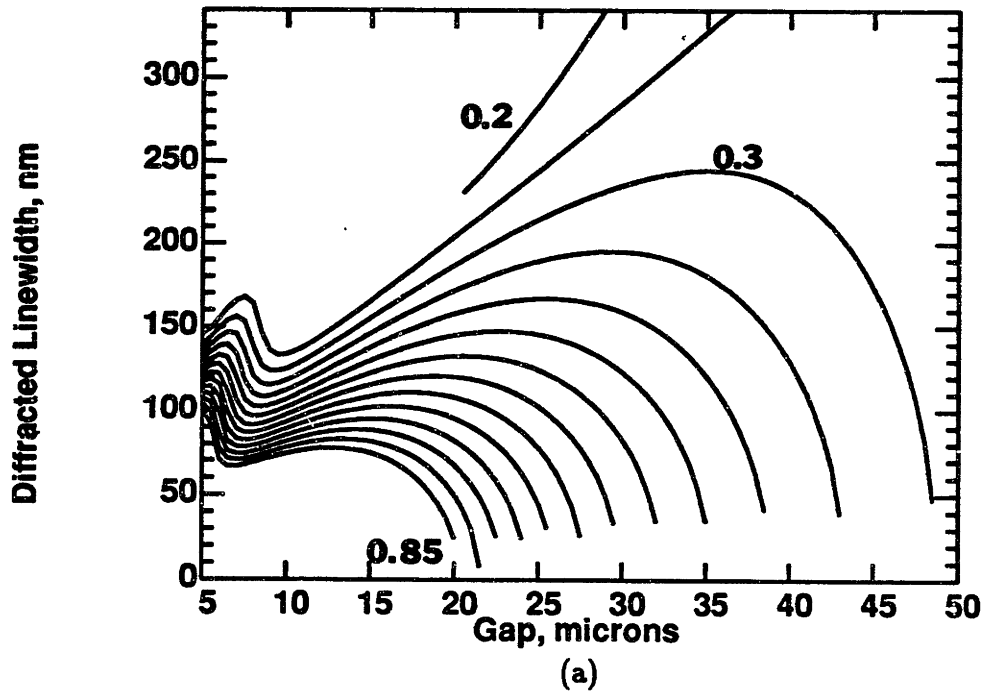


Figure 5.7: Equi-irradiance curves of the diffracted image of a  $0.17 \mu\text{m}$ -wide slit for gaps ranging from 5 to  $50 \mu\text{m}$ . The equi-irradiance curves vary from 0.15 (bottom curve) to 0.85 (top curve) in 0.05 increments. The absorber thickness is  $0.25 \mu\text{m}$  in (a) and  $0.5 \mu\text{m}$  in (b).

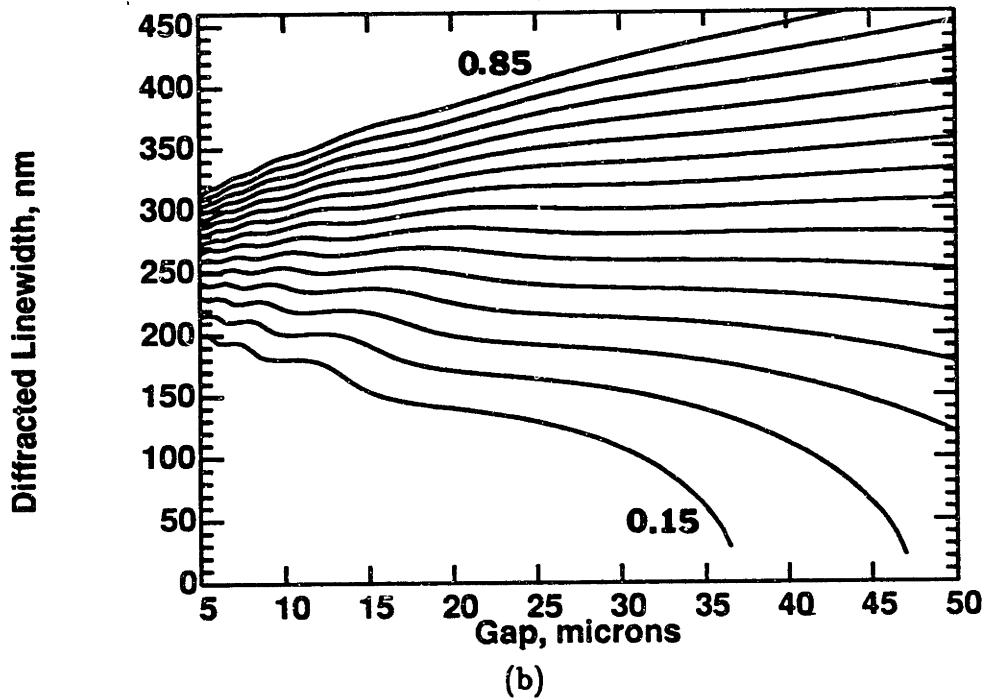
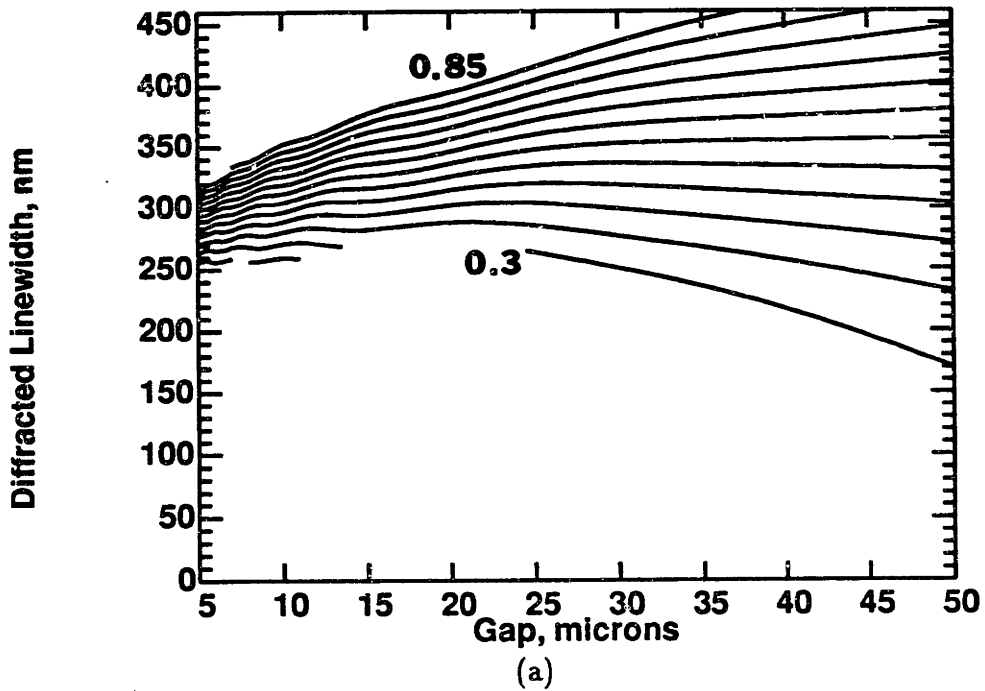
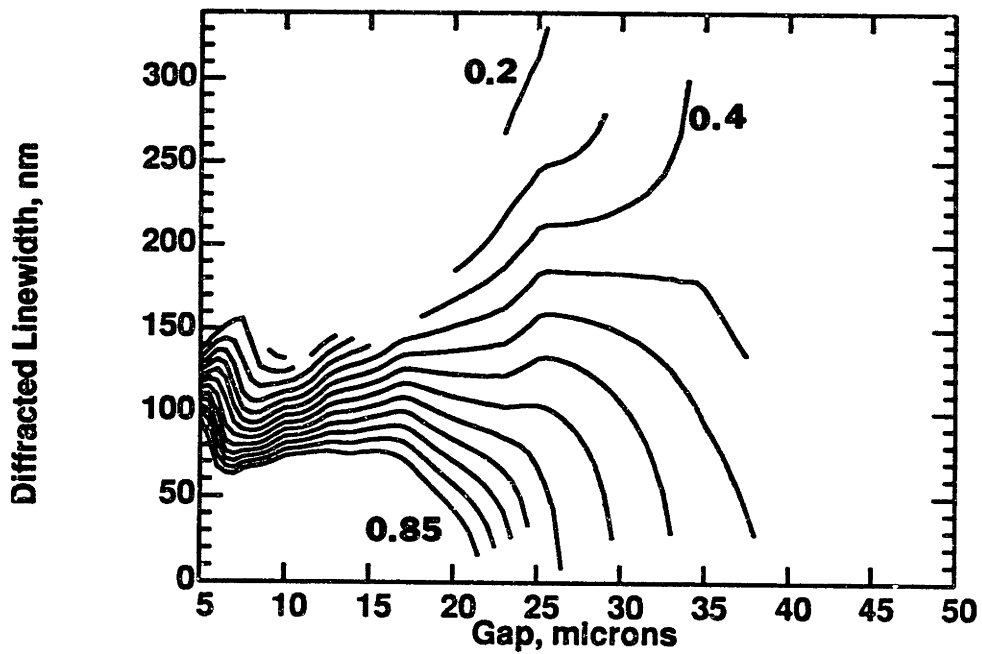
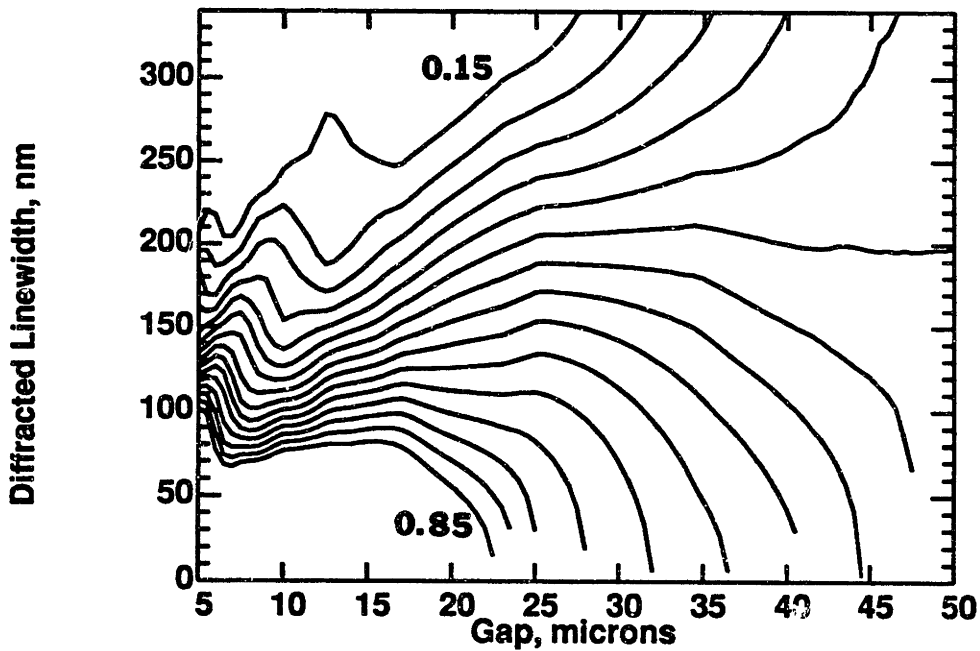


Figure 5.8: Equi-irradiance curves of the diffracted image of a  $0.23 \mu\text{m}$ -wide line for gaps ranging from 5 to  $50 \mu\text{m}$ . The equi-irradiance curves vary from 0.15 (top curve) to 0.85 (bottom curve) in 0.05 increments. The absorber thickness is  $0.25 \mu\text{m}$  in (a) and  $0.5 \mu\text{m}$  in (b).

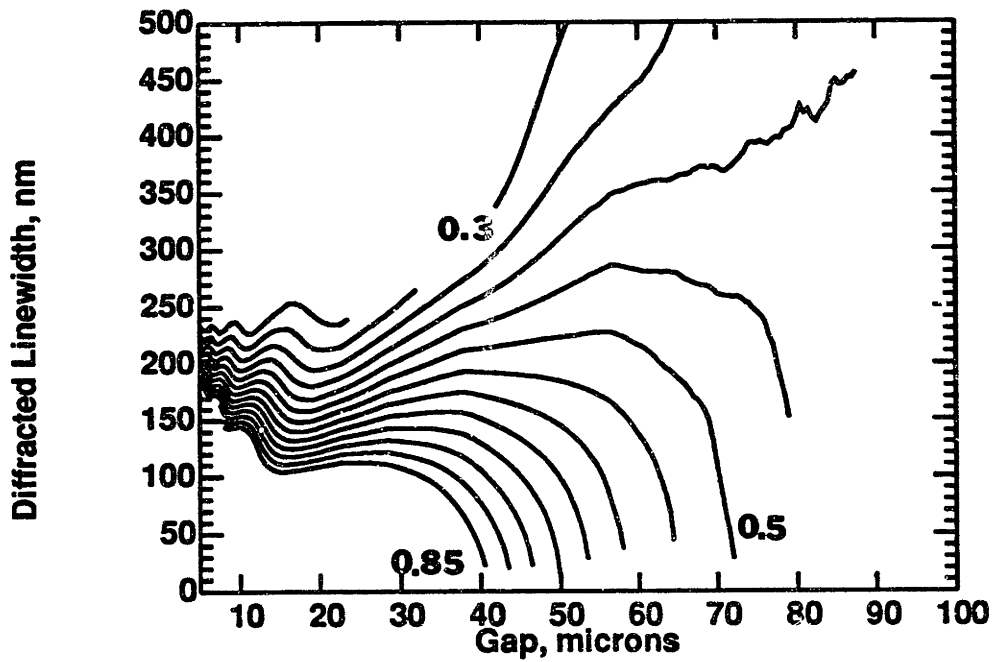


(a)

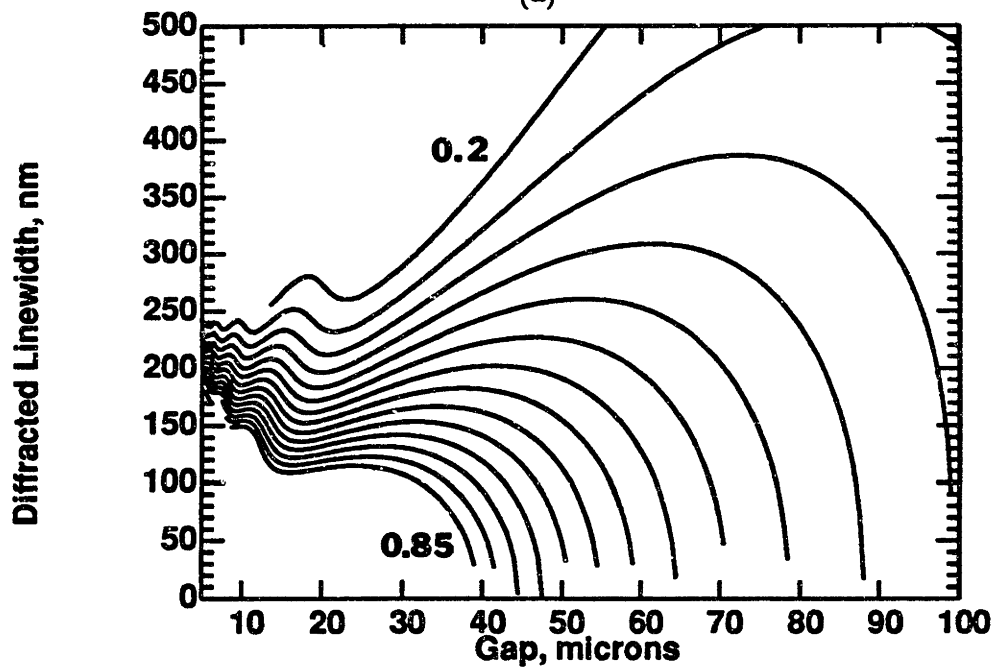


(b)

Figure 5.9: Equi-irradiance curves of the diffracted image of a  $0.4 \mu\text{m}$ -period grating, with  $0.17 \mu\text{m}$ -wide spaces, for gaps ranging from 5 to  $50 \mu\text{m}$ . The equi-irradiance curves vary from 0.15 (bottom curve) to 0.85 (top curve) in 0.05 increments. The absorber thickness is  $0.25 \mu\text{m}$  in (a) and  $0.5 \mu\text{m}$  in (b).

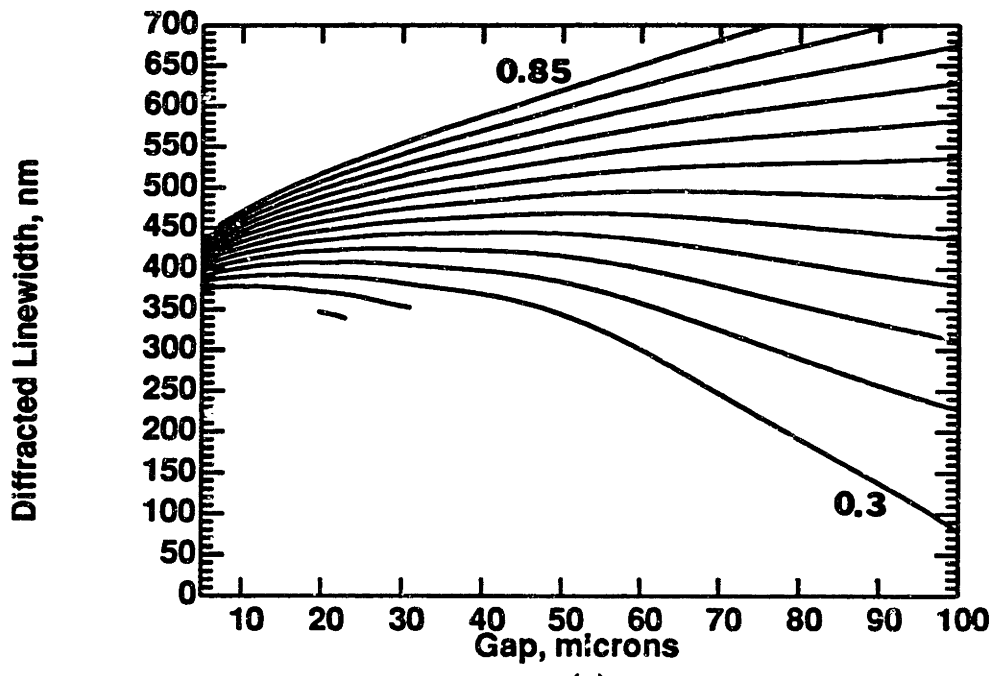


(a)

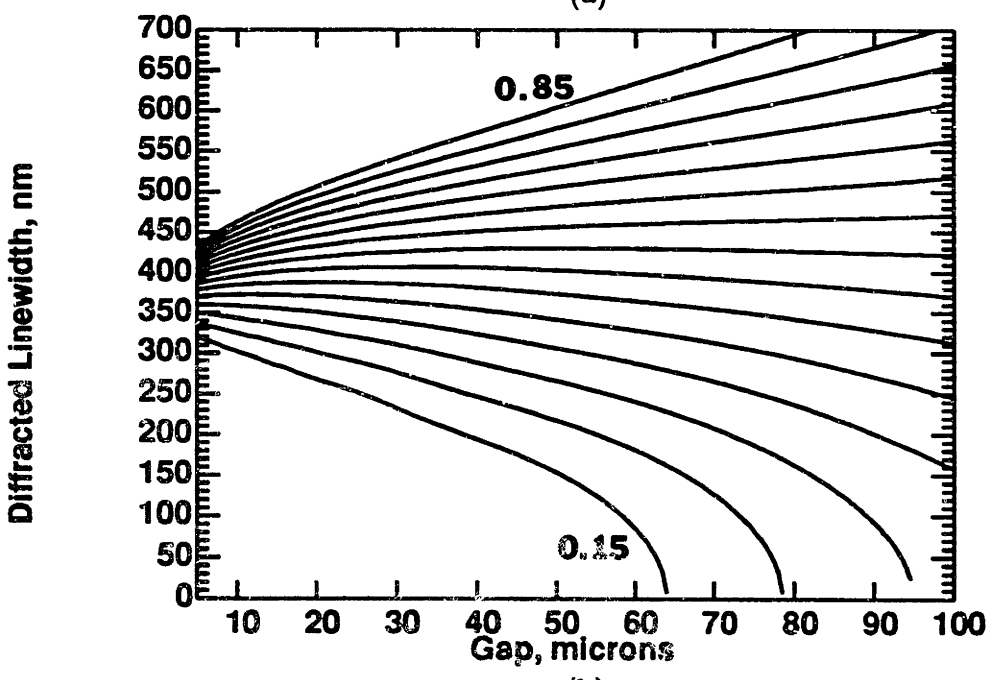


(b)

Figure 5.10: Equi-irradiance curves of the diffracted image of a  $0.25 \mu\text{m}$ -wide slit for gaps ranging from 5 to  $100 \mu\text{m}$ . The equi-irradiance curves vary from 0.15 (bottom curve) to 0.85 (top curve) in 0.05 increments. The absorber thickness is  $0.25 \mu\text{m}$  in (a) and  $0.5 \mu\text{m}$  in (b).

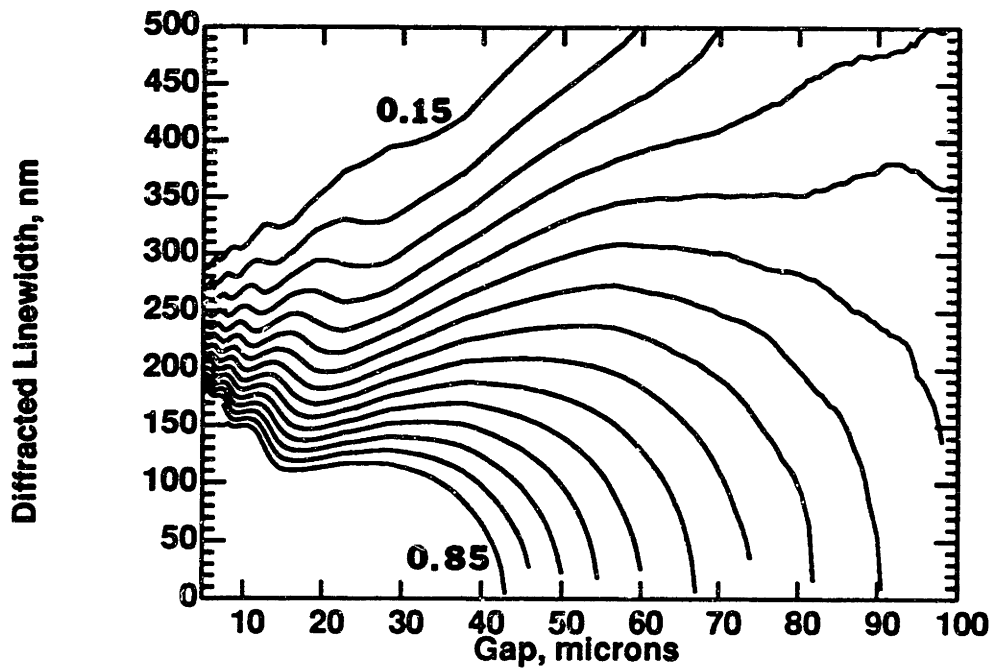


(a)

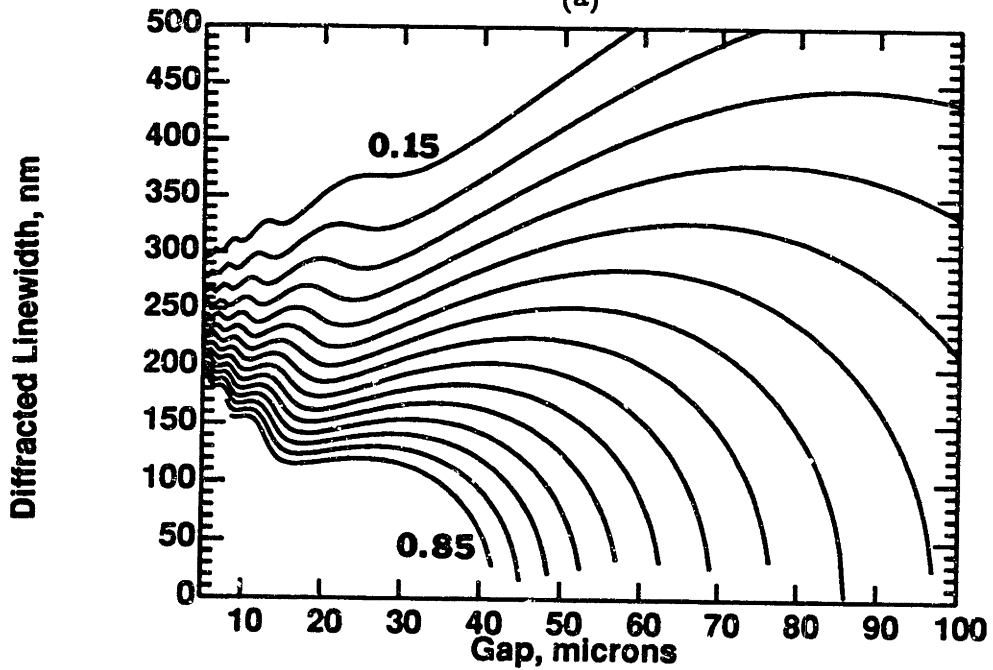


(b)

Figure 5.11: Equi-irradiance curves of the diffracted image of a  $0.35 \mu\text{m}$ -wide line for gaps ranging from  $5$  to  $100 \mu\text{m}$ . The equi-irradiance curves vary from  $0.15$  (top curve) to  $0.85$  (bottom curve) in  $0.05$  increments. The absorber thickness is  $0.25 \mu\text{m}$  in (a) and  $0.5 \mu\text{m}$  in (b).



(a)



(b)

Figure 5.12: Equi-irradiance curves of the diffracted image of a  $0.6 \mu\text{m}$ -period grating, with  $0.25 \mu\text{m}$ -wide spaces, for gaps ranging from 5 to  $100 \mu\text{m}$ . The equi-irradiance curves vary from 0.15 (bottom curve) to 0.85 (top curve) in 0.05 increments. The absorber thickness is  $0.25 \mu\text{m}$  in (a) and  $0.5 \mu\text{m}$  in (b).

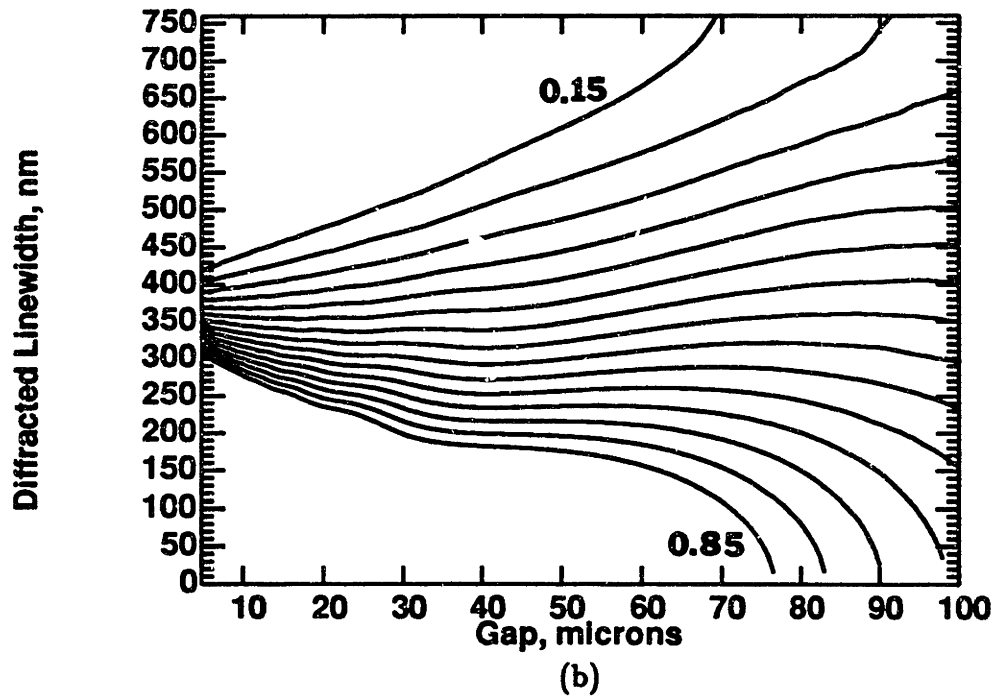
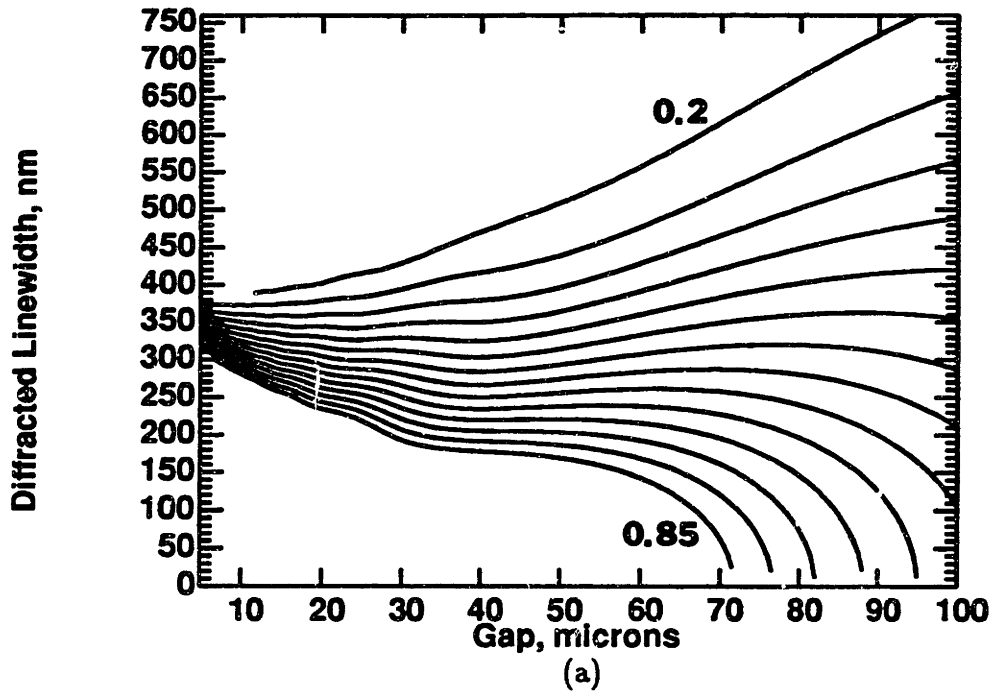
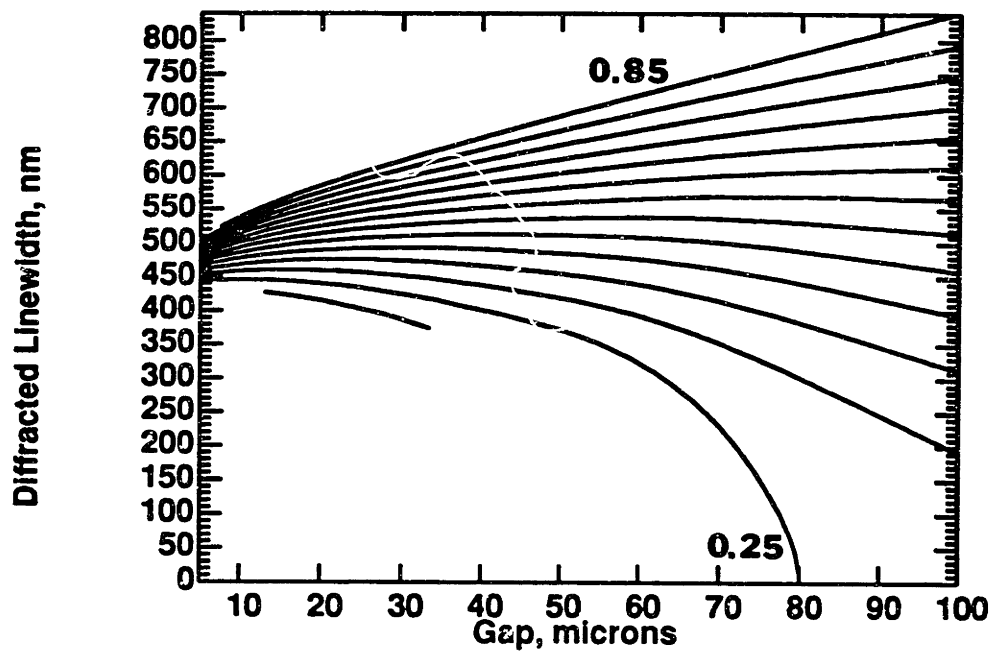
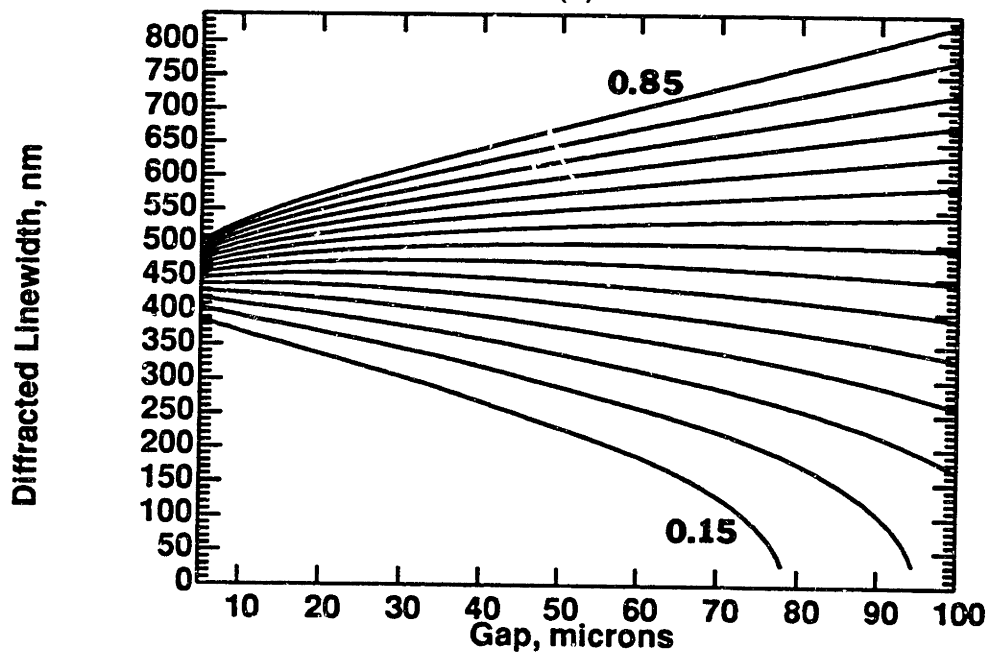


Figure 5.13: Equi-irradiance curves of the diffracted image of a  $0.38 \mu\text{m}$ -wide slit for gaps ranging from 5 to  $100 \mu\text{m}$ . The equi-irradiance curves vary from 0.15 (bottom curve) to 0.85 (top curve) in 0.05 increments. The absorber thickness is  $0.25 \mu\text{m}$  in (a) and  $0.5 \mu\text{m}$  in (b).



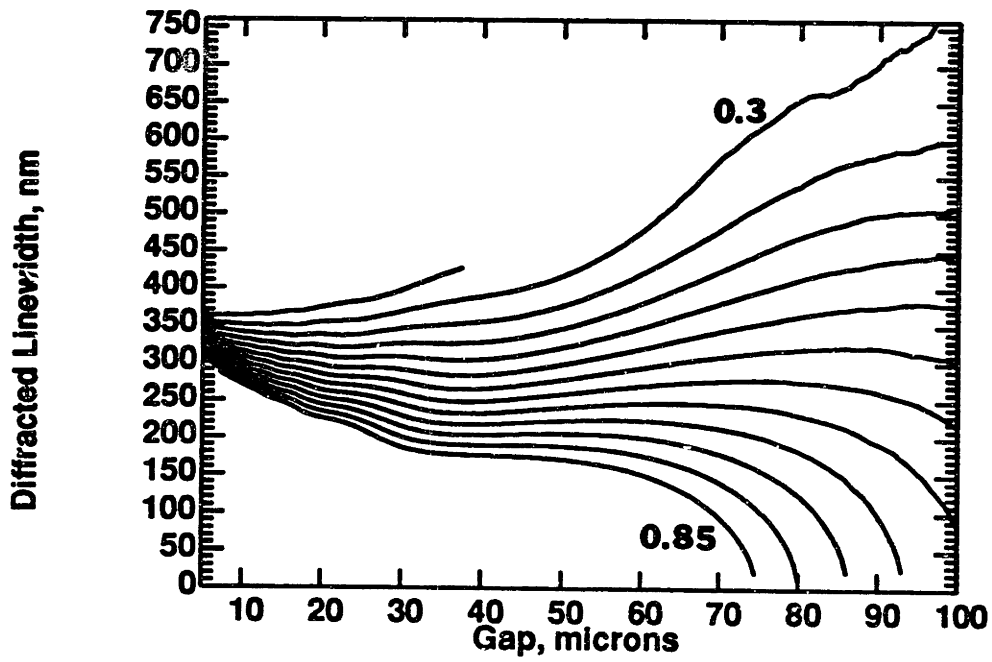
(a)



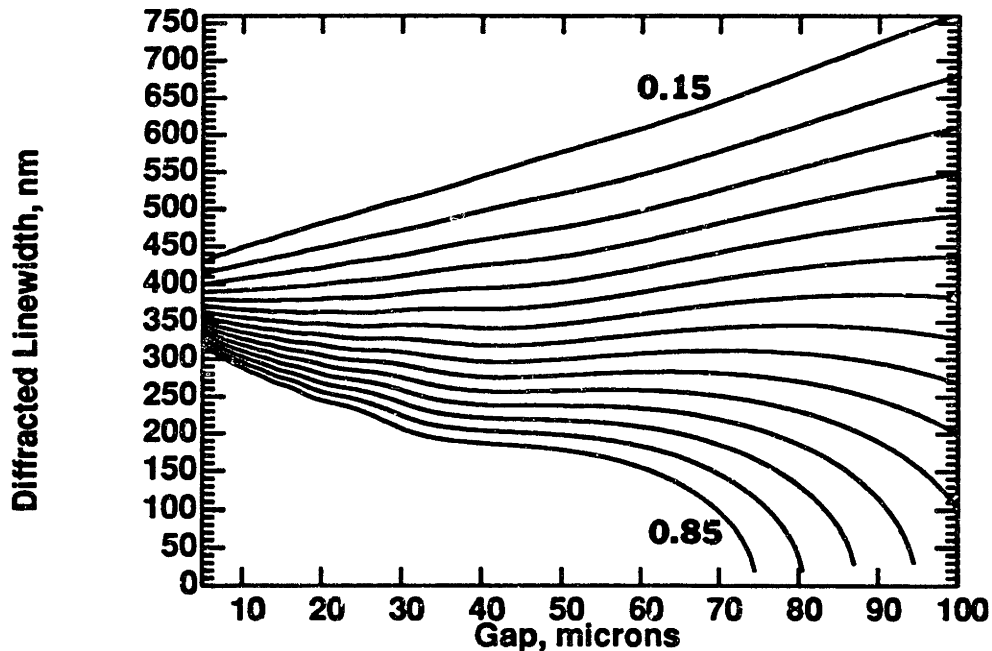
(b)

Figure 5.14: Equi-irradiance curves of the diffracted image of a  $0.42 \mu\text{m}$ -wide line for gaps ranging from 5 to  $100 \mu\text{m}$ . The equi-irradiance curves vary from 0.15 (top curve) to 0.85 (bottom curve) in 0.05 increments. The absorber thickness is  $0.25 \mu\text{m}$  in (a) and  $0.5 \mu\text{m}$  in (b).



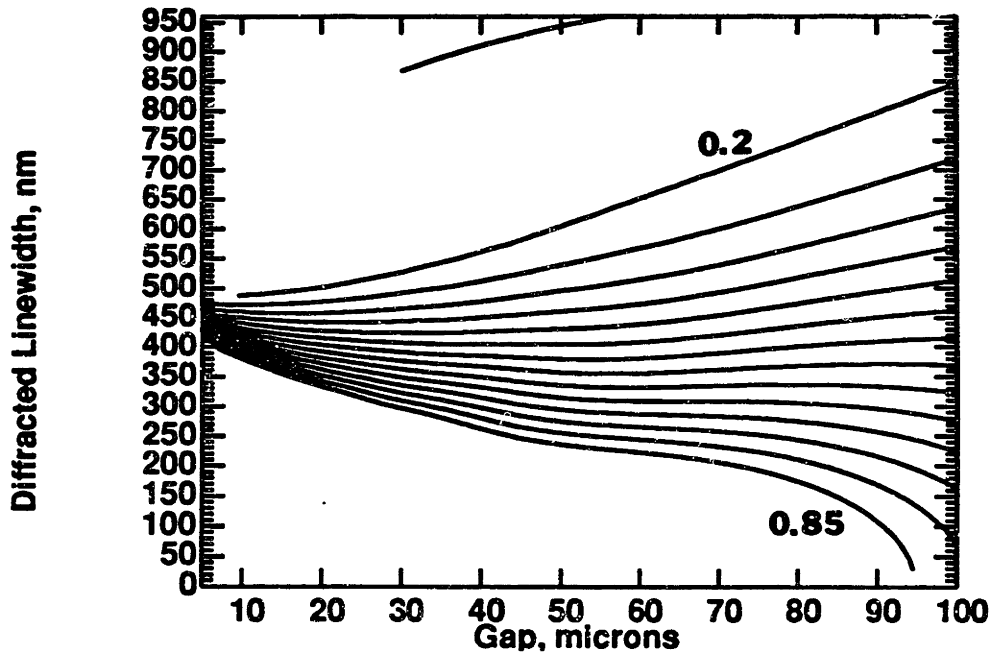


(a)

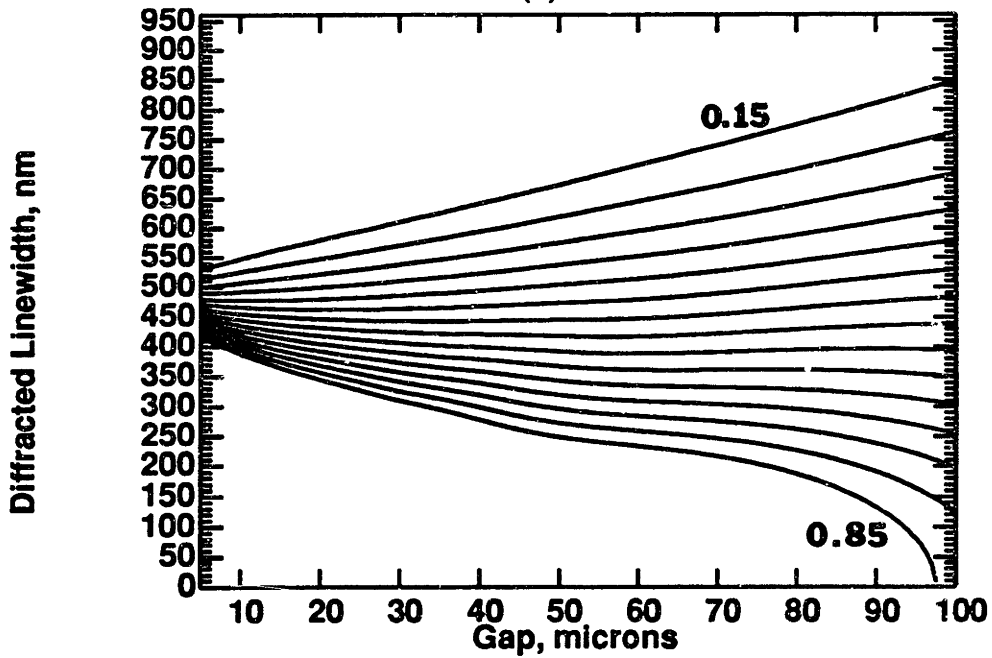


(b)

Figure 5.15: Equi-irradiance curves of the diffracted image of a  $0.8 \mu\text{m}$ -period grating, with  $0.38 \mu\text{m}$ -wide spaces, for gaps ranging from  $5$  to  $100 \mu\text{m}$ . The equi-irradiance curves vary from  $0.15$  (bottom curve) to  $0.85$  (top curve) in  $0.05$  increments. The absorber thickness is  $0.25 \mu\text{m}$  in (a) and  $0.5 \mu\text{m}$  in (b).



(a)



(b)

Figure 5.16: Equi-irradiance curves of the diffracted image of a  $0.48 \mu\text{m}$ -wide slit for gaps ranging from 5 to  $100 \mu\text{m}$ . The equi-irradiance curves vary from 0.15 (bottom curve) to 0.85 (top curve) in 0.05 increments. The absorber thickness is  $0.25 \mu\text{m}$  in (a) and  $0.5 \mu\text{m}$  in (b).

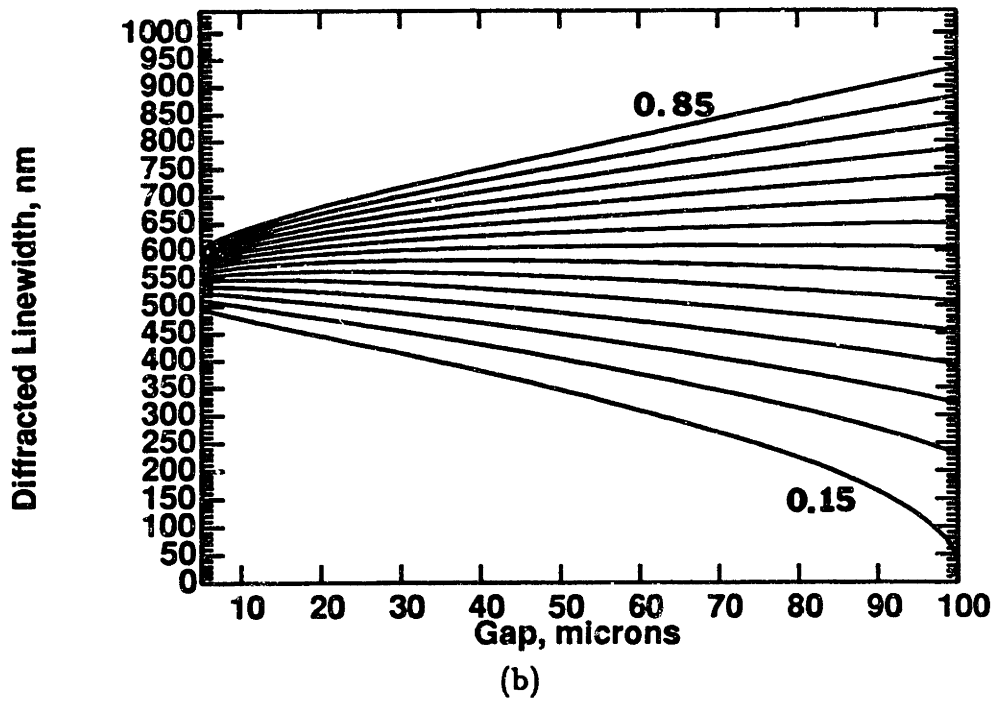
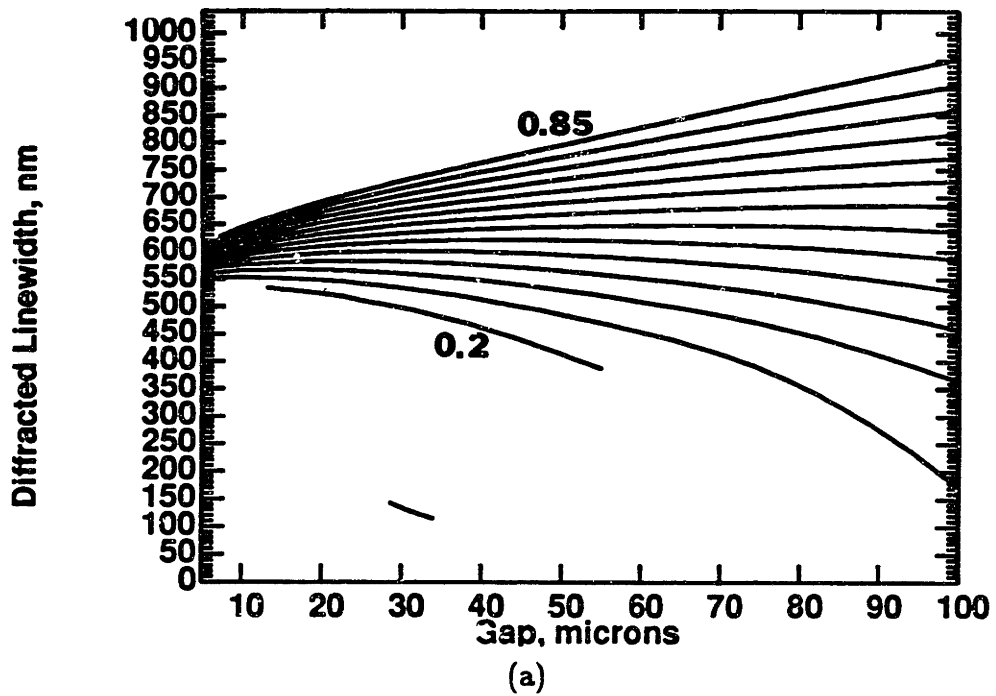
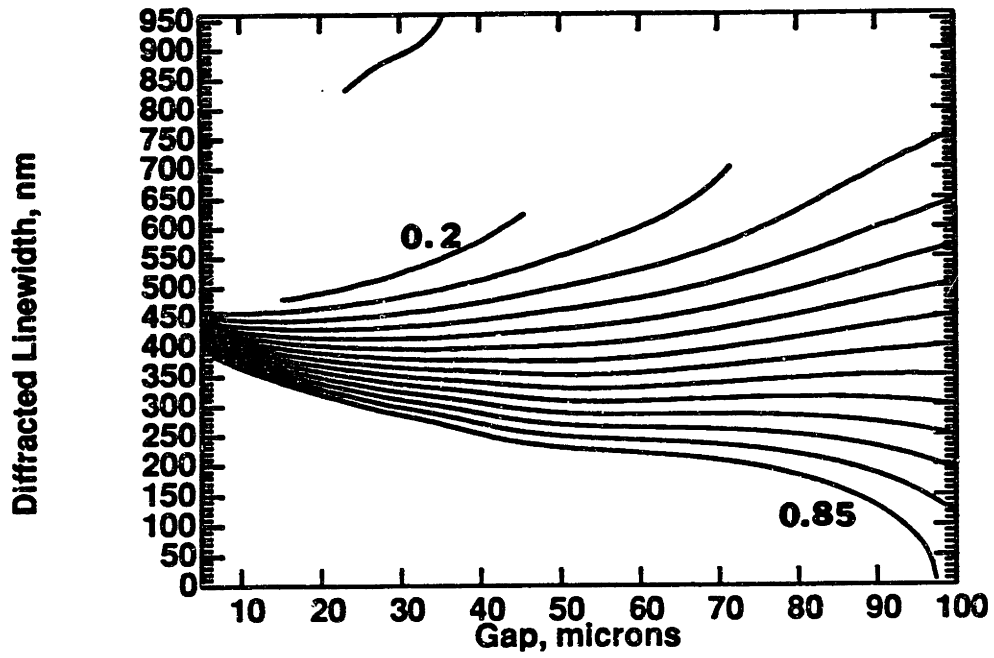
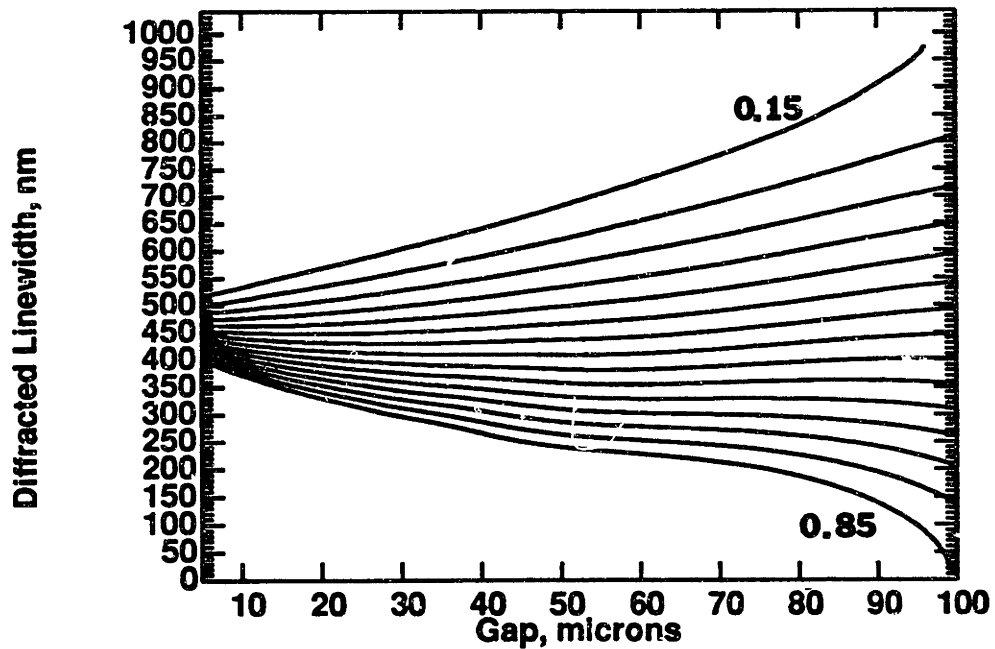


Figure 5.17: Equi-irradiance curves of the diffracted image of a  $0.52 \mu\text{m}$ -wide line for gaps ranging from  $5$  to  $100 \mu\text{m}$ . The equi-irradiance curves vary from  $0.15$  (top curve) to  $0.85$  (bottom curve) in  $0.05$  increments. The absorber thickness is  $0.25 \mu\text{m}$  in (a) and  $0.5 \mu\text{m}$  in (b).



(a)



(b)

Figure 5.18: Equi-irradiance curves of the diffracted image of a  $1.0 \mu\text{m}$ -period grating, with  $0.48 \mu\text{m}$ -wide spaces, for gaps ranging from 5 to  $100 \mu\text{m}$ . The equi-irradiance curves vary from 0.15 (bottom curve) to 0.85 (top curve) in 0.05 increments. The absorber thickness is  $0.25 \mu\text{m}$  in (a) and  $0.5 \mu\text{m}$  in (b).

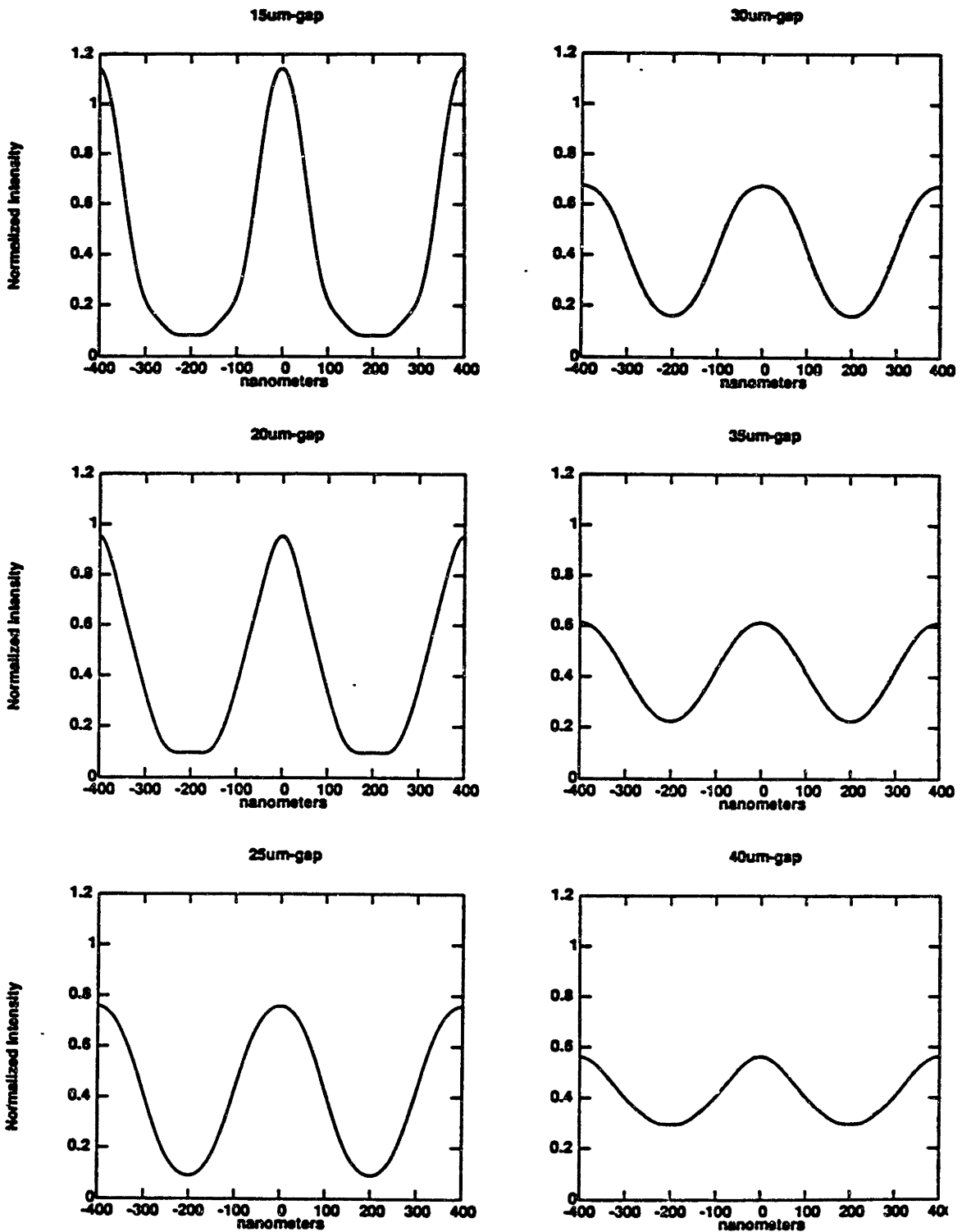


Figure 5.19: Diffraction patterns for a  $0.4 \mu\text{m}$ -period grating with  $0.17 \mu\text{m}$ -wide spaces with  $0.5 \mu\text{m}$ -thick Au absorber.

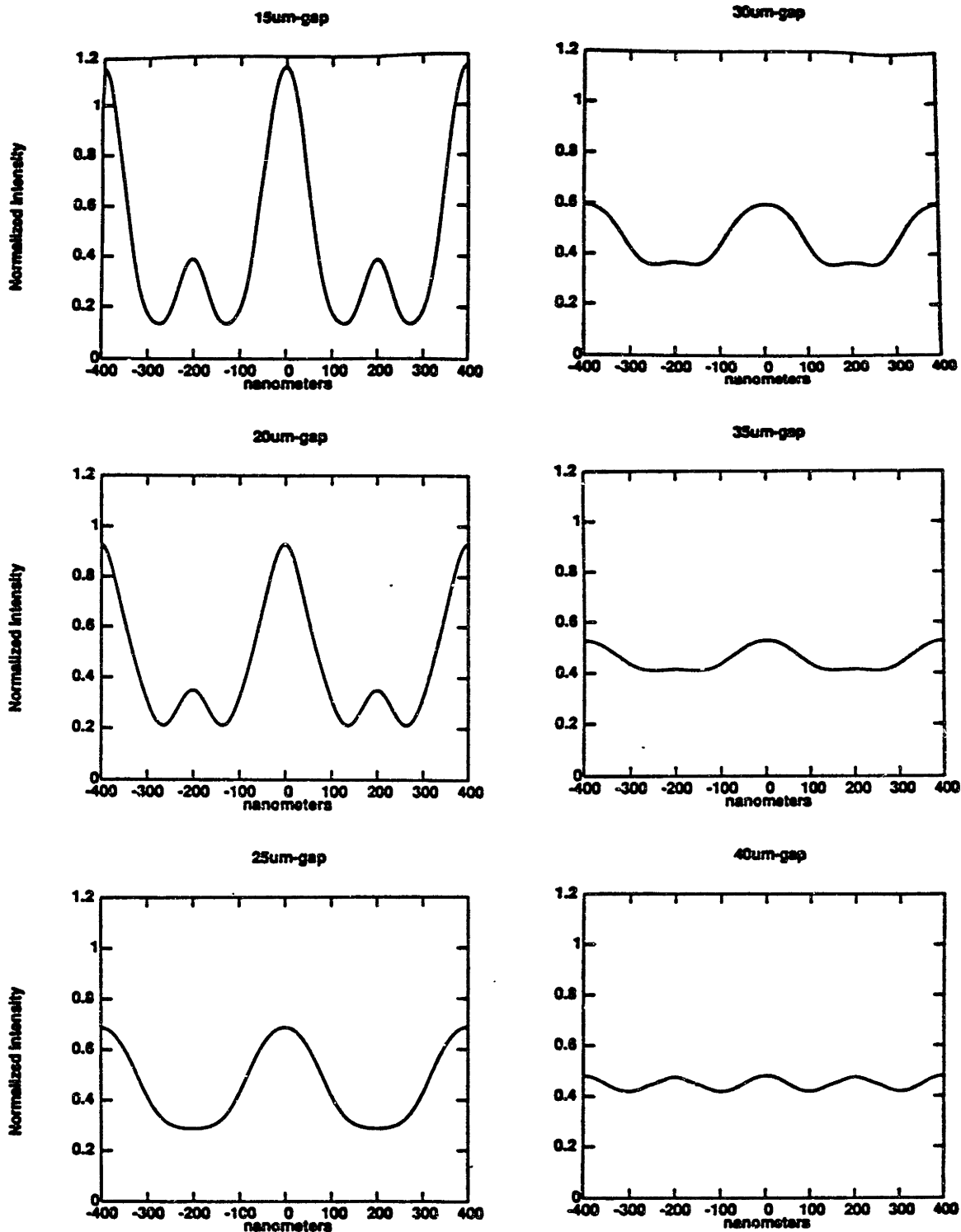


Figure 5.20: Diffraction patterns for a  $0.4 \mu\text{m}$ -period grating with  $0.17 \mu\text{m}$ -wide spaces with  $0.25 \mu\text{m}$ -thick Au absorber.

# Chapter 6

## Diffraction: Experimental

In this chapter, the experimental work in diffraction is detailed. I will review mask fabrication and patterning, methods for varying the gap, the experimental conditions, and the results. The results show qualitative agreement with the simulations from Chapter 5, although some discrepancies were found. The smallest features, the  $0.17\ \mu\text{m}$ -wide spaces are shown to print to gaps as large as  $35\ \mu\text{m}$ , with line quality beginning to significantly deteriorate at  $\sim 18\ \mu\text{m}$ .

### 6.1 Mask Fabrication

The type of mask used in these experiments, called a microgap mask, was invented by Mark Schattenburg et al. [23,27]. The term microgap was coined to denote the small mask-to-substrate separation of  $\sim 5\ \mu\text{m}$ . The microgap is created by six tiny studs on the rim of the mask membrane which separate the mask membrane from the wafer to be exposed. The mask and substrate are clamped together, with the aid of an aluminum ring and two spring arms, on top of an optically-flat pin-chuck as illustrated in Figure 6.1.

X-ray mask fabrication is an evolving art that typically involves the efforts, and creative contributions, of many workers, both students and research staff. Mask

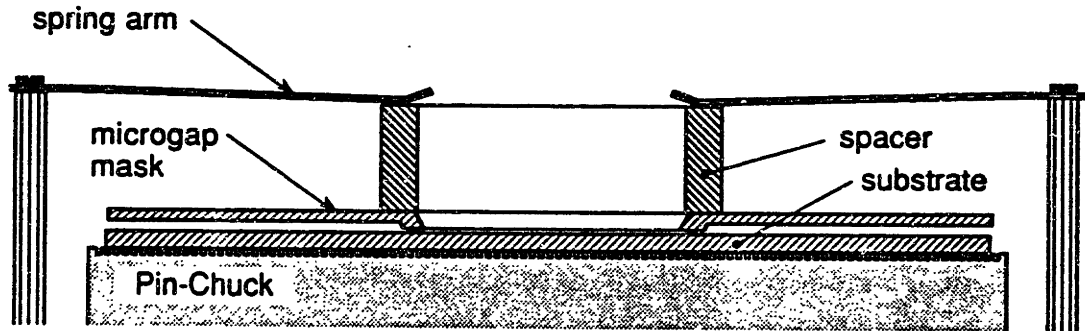


Figure 6.1: The six studs of the microgap mask rest on the resist coated wafer which sits on an optically-flat pin-chuck. An aluminum spacer sits on top of the mask. The assembly is clamped together with two spring arms. During exposure, the mask assemblage is inverted to face the x-ray source which will be below it.

blanks, of the type described here, are processed in lots of 25 with most of the processing being done by UROP students under graduate student supervision.

The fabrication sequence of a microgap mask is depicted in Figure 6.2 [23]. We start with 3 inch diameter (100) silicon wafers that are coated with 1 to 2  $\mu\text{m}$  of low-stress silicon rich silicon nitride. A circle,  $\sim 1$  inch in diameter, is etched through the nitride on the back side of the mask wafer. The substrate is then etched in KOH until the thin mask membrane is exposed. Next, the nitride surrounding the membrane area on the frontside of the mask is removed by reactive-ion-etching (RIE) and the wafer is returned to the KOH to etch away the top 100  $\mu\text{m}$  of silicon. The purpose of this step, called the mesa etch, is to insure that when the mask is in use only the membrane area of the mask wafer will be in close proximity to the substrate which is to be exposed.

During the mesa etch, the membrane defining nitride is undercut at the edges. After the mesa etch, the overhanging nitride must be removed by RIE. The mem-



brane is RCA cleaned and plating base, consisting of 5 nm of nickel-chromium and 10nm of gold, is evaporated. Immediately after evaporation, resist is spun-on the membrane which is now ready to be patterned by e-beam, focused-ion-beam (FIB), holography, or x-ray.

For the masks used in these experiments, the mask writing tool was the FIB, operated by Mark Shepard, in the Technology Research Laboratory (TRL). The pattern consisted of an array of lines, spaces, and gratings of nominal 0.1, 0.2, 0.3, 0.4 and 0.5  $\mu\text{m}$  linewidths. Some two dimensional patterns were also included. After beam writing, I developed the exposed pattern and electroplated the mask. Sample patterns are shown in Figures 6.3 and 6.4.

In all, three masks were successfully written, two of which were used extensively in this thesis. At the time of writing these masks, the focused ion beam system was plagued with high noise levels and with charging problems, which caused beam astigmatism. Consequently, significant unintended biasing of the mask features was introduced, as well as edge roughness, which can be seen in Figure 5.5. On only one mask, KE-FIB-#2, were any 0.1  $\mu\text{m}$  features resolved, and those were mostly the widely spaced features, the isolated lines and posts, and a small grating area. This mask was used in resist characterization work shown in Figures 3.2 through 3.5. For the diffraction work, the mask KE-FIB-#5 was used; its average line and space widths, as measured in the SEM, are listed in Table 5.2.

After electroplating, the resist is stripped in an oxygen plasma. Finally, aluminum studs are stencil-evaporated to define the microgap. The membrane area of the microgap mask is flat to within about 1  $\mu\text{m}$ . A more recent design [89], in which the membrane wafer is anodically bonded to an optically-flat pyrex ring, provides membranes that are flat to within 100 nm. However, this technology was not sufficiently evolved for use at the time of these experiments. The microgaps for both KE-FIB-#2 and KE-FIB-#5 were measured to be  $5 \pm 1 \mu\text{m}$ . In the next section, methods of extending the gap are presented.

## 6.2 Experimental Set-Up

In x-ray proximity printing, gathering experimental diffraction data for a wide variety of gaps has been hampered by the absence of gap control techniques. At present, x-ray steppers are being developed with built-in electromechanical gap control. Alberto Moel is currently building such a system here in the SSL for his dissertation [69,89]. This system is not yet fully operational, so for this thesis, other methods were needed.

To obtain a variety of gaps, two techniques were tried. These are illustrated in Figure 6.5. In (a), the gap is increased by etching a pit in the wafer. The total gap is the sum of the stud height and the etched pit depth. In (b), the substrate has a number of v-grooves etched into its surface; thus, the gap varies with position along the sloped wall of a groove. For the set-up shown in (b), the absorber lines on the mask are oriented perpendicular to the groove as indicated by the directional arrow in the sketch. Fabrication of the two types of substrates, and methods of calibrating the gap, are discussed in Sections 6.2.1 and 6.2.2.

Direct measurements of gap could not be made for the set-ups shown in Figure 6.5. However, many exposures were made prior to these experiments, during the process of resist characterization. For all of those exposures the microgap between mask and substrate, which was set by the stud height, was measured using an angular-fringe measurement technique outlined in reference [27,90]. This technique is illustrated in Figure 6.6. A sodium light is held  $45^\circ$  off an axis normal to the mask membrane surface, the observer places her eye opposite the sodium lamp at  $45^\circ$  from the same normal axis. The eye and sodium lamp are slowly brought together above the mask while counting the number of fringes that pass through the observation point at the intersection of the mask and the measurement axis. This is illustrated in Figure 6.6. Typically, five or six fringes were counted corresponding to a 4 to 5  $\mu\text{m}$  gap. For the experiments presented in this chapter,

the gap is taken to be the depths calibrated from the wafer surface, as outlined in Sections 6.2.1 and 6.2.2,  $\pm 1 \mu\text{m}$ .

### 6.2.1 Etched Pits

The etched pits were formed by anisotropic etching with potassium hydroxide (KOH); thermal oxide was used as the mask material. The etchant was a 40:60 mixture, by weight, of KOH and deionized water (DI) at 60°C. KOH is known to roughen the surface of silicon, but, by using a low temperature and high KOH concentration, surface roughening was minimized. Inspection of the etched pits using a Linnik interferometer showed the roughness to be less than 100nm. This roughening, which is quite visible in the optical microscope, is hardly detectable in the SEM.

The depth of each pit was determined by running a calibrated stylus over the edge of the pit on four sides. For each of the four measurements the recorded depths agreed to within 100nm. The pits were found to be flat to within a single fringe of the Graham (Fizeau) Interferometer.

Spinning resist onto the etched wafers did not present any problems. "Cometing" of the resist was always present beginning from the pit edge and radiating to the wafer edge, but these small resist thickness variations did not affect the gap height. Other than at the perimeter, film coverage inside the pit was as uniform as for an unetched wafer. Interferograms of an etched pit are included in Appendix C.

SEM's from an exposure made using a 20  $\mu\text{m}$ -deep pit, or a gap of approximately 25  $\mu\text{m}$ , are shown in Figure 6.7. At the left are well-resolved 0.3  $\mu\text{m}$ -wide features, and, at the right, nominal 0.2  $\mu\text{m}$ -wide features which are not quite resolved. The resist is Ray-PF, exposed for 6 hours at 8 keV accelerating potential and 600 Watts. The source to substrate distance was 49.4 cm. Following a one hour hold time and a one minute, 70°C P.E.B., the sample was developed in 1:1

AZ developer:DI for 90 seconds.

The etched pit method works well for gap control, but it was not pursued because of the large number of exposures required to get meaningful data. It was felt the the chemically amplified resists have not yet exhibited sufficiently consistent behavior from exposure to exposure to make results meaningful. This left PMMA as the only possible candidate for use with this technique. Because of PMMA's comparative insensitivity, and because of the low x-ray flux of our source, a single exposure, at a source-to-substrate distance of 50 cm, would require in excess of 65 hours. Consequently, the etched pit method was abandoned in favor of the v-groove technique.

### 6.2.2 V-Grooves

Using a 200  $\mu\text{m}$ -period grating and KOH etching,  $\sim 100 \mu\text{m}$ -deep v-grooves were etched in (100) silicon wafers. To provide a reference for measuring gaps in the SEM, a 1  $\mu\text{m}$ -period grating was patterned onto the wafer with the grating lines running parallel to the grooves. This was done using x-ray proximity printing and Au lift-off.

The way the measurement grating is used to calibrate gap is illustrated in Figure 6.8 which shows a cross section of the 1  $\mu\text{m}$ -period mask above a (100) substrate with an exposed (111) sloped wall. Because the wall lies at  $54.7^\circ$  to the wafer surface, each period of the grating, projected onto the wall, corresponds to a change in depth of  $\sqrt{2}p$  where  $p$  is the period. After the grating is exposed in resist, gold is evaporated on the wafer, and the resist is stripped. More resist is then spun-on prior to the final exposure.

During the final exposure, the multifeatured mask is oriented with its absorber lines running perpendicular to this measurement grating as indicated in Figure 6.5 (b). When the exposure is later examined in the SEM, gaps are calibrated by counting the number of periods from the wafer surface to the point of examination,

multiplying by  $\sqrt{2}$ , and adding  $5 \mu\text{m}$  to account for the microgap. A conservative estimate of error in gap calibration using this method is  $\pm 1 \mu\text{m}$  with most of this error associated with microgap uncertainty.

Before patterning the measurement grating, the wafers were coated with a nominal  $1 \mu\text{m}$ -thick layer of Ray-PN. The walls of the v-grooves, which are  $\{111\}$  crystallographic planes, lie at such a steep angle from the wafer surface that resist coverage varied with position. Typically, near the top of the groove, one wall exhibited close to the full resist thickness while on the other wall was only thinly coated for the first few microns of depth; further down the walls, the resist thickness slowly oscillated along the depth of the groove from  $\sim 0.4$  to  $1 \mu\text{m}$ . Cross sections of a v-groove can be seen in Figures 6.9 and 6.10. The resist thickness oscillations are just barely detectable in Figure 6.9 (a). In Figure 6.10, undulations are seen along the grating lines. These occur at jogs in the v-groove wall that were caused by imperfect alignment of the  $200 \mu\text{m}$ -period v-groove mask to the  $\{111\}$  crystallographic planes. In the patterning of the measurement grating, a unique capability of x-ray proximity printing is manifest. This grating could not have been patterned using any other technology because there is no other technology that has both the requisite resolution and depth of field.

After x-ray exposure and development,  $5 \text{ nm}$  of chromium and  $25 \text{ nm}$  of gold were evaporated normal to the wafer surface. The resist was then removed by soaking in AZ 300-T stripper, heated to  $80^\circ \text{C}$ , for 30 minutes. To ensure complete lift-off of any residual Au, the wafers were sprayed with acetone at 60 psi. After RCA cleaning, the wafers were ready to be coated with Ray-PN for the final exposure. Each wafer was coated just prior to loading it into the x-ray chamber. Prior to spinning on the resist, the wafer was dipped in BOE (Buffered Oxide Etch) to remove any native oxide and promote resist adhesion.

## 6.3 Results and Discussion

Ray-PN resist was used for the v-groove diffraction experiment. Resist was spun on at 7 kRPM, for 30 seconds, after which, the wafer received a 1 minute bake on a vacuum-chucked hotplate set to 130°C. The hotplate setting leads to a wafer surface temperature of 120°C. Immediately after the bake, the wafer was loaded into the x-ray head and exposed. After removal from the x-ray head, the sample was baked for 5 minutes at 105°C (a hotplate setting of 115°C) and then developed in 1:1 AZ developer:DI for 5 minutes at 22°C. Two exposures are shown in Figures 6.11 and 6.12. The calculated doses for the two exposures are 24 and 26.4 mJ/cm<sup>2</sup>, respectively. For each exposure the total time in vacuum was 13 hours. In each exposure, a horizontal discontinuity is seen in the line pattern; this was caused by a stitching error in mask pattern writing with the FIB. Close-ups of the nominal 0.2 μm features, for gaps from approximately 5 to 40 μm, are shown in Figures 6.13 through 6.16.

The effects of diffraction, and spatial incoherence, are discernable in these two exposures. In this discussion, lines and spaces refer to *mask* lines and spaces; since a negative resist was used, these appear in the reverse polarity in the micrographs. Observations are enumerated below.

1. With increasing gap, isolated lines tend to broaden and then, as image contrast drops, they narrow, and eventually close. This is most evident in Figure 6.11.
2. In Figure 6.12, isolated spaces print to deeper gaps, gratings and isolated lines cease to print at gaps smaller than those in Figure 6.11. This is consistent with the direction of dose difference in the two exposures.
3. The outermost line in the grating tends to print to a deeper gap, though it does not print to as deep a gap as the the isolated line. This corresponds the

single-sided contribution of diffraction from the other grating lines. This is seen most clearly in groups (a) and (b) of Figure 6.11.

4. Constructive interference effects are seen in that the grating spaces merge together at gaps where the isolated space and the isolated line are still printing.
5. For the nominal  $0.2\ \mu\text{m}$  features, at gaps greater than  $20\ \mu\text{m}$ , spaces print wider and lines print narrower on the gold lines of the  $1\ \mu\text{m}$ -period measurement grating than on silicon. This is a consequence of decreased slope in the diffraction profile and reduced contrast in the diffracted image. Electrons, generated from x-rays absorbed in the gold plating base, contribute to the total energy dose exposing the resist. As the diffracted profile acquires a more shallow slope, the additional energy supplied by the electrons from the plating base kicks the total dose up high enough so that the linewidth is significantly altered. This effect is exhibited weakly in the grating of Figure 6.15 beginning at  $G \geq 15\ \mu\text{m}$  and with rapidly increasing strength for  $G \geq 18\ \mu\text{m}$ . This trend correlates well with the spreading of equi-irradiance curves in Figure 5.8 (a).

Where the diffracted intensity has dropped below the clipping level on silicon, the extra contribution of electrons from the plating base allows a single space to continue printing on the gold for several microns increase in gap. This is seen in Figure 6.14 for  $36 \leq G \leq 42$ , and agrees well with the loss of contrast that can be seen in Figure 5.6 (a).

6. The effect of source incoherence is seen in that the usable gap does not scale with  $\alpha$ . For example, for the lower dose exposure, the  $0.4\ \mu\text{m}$ -period grating is still printing at a  $35\ \mu\text{m}$  gap, albeit poorly; for its space width of  $0.17\ \mu\text{m}$ , this corresponds to  $\alpha = 1.6$ . If gap scaled with alpha, the  $0.6\ \mu\text{m}$ -period grating with  $0.25\ \mu\text{m}$ -wide spaces should print to  $75\ \mu\text{m}$ , but, it only prints

to about 60  $\mu\text{m}$ .

What appears at first glance to be a diffraction induced oscillation in linewidth in Figures 6.11 and 6.12, consisting of a slight broadening for all features at  $\sim 10 \mu\text{m}$  followed by a narrowing at  $\sim 30 \mu\text{m}$  and then a final broadening before closure, is in fact an optical illusion created by an oscillation in resist thickness along the depth of the v-groove wall.

None of the oscillations that are seen in the equi-irradiance contours for the 0.2 and 0.3  $\mu\text{m}$  spaces and gratings, seen in Figures 5.6, 5.8, 5.9, and 5.11, are detectable in the exposures. The oscillations, if present, would be at most 10% of the linewidth which is comparable to the mask feature edge roughness. The oscillations could be further damped out by the chemical amplification mechanism in the resist. It is also possible that the oscillations are really absent in the diffracted image. No conclusion in this issue can be drawn from these results.

In attempting to measure linewidth as a function of gap I was presented with several difficulties: (1) the edge roughness of the mask lines is a considerable fraction of the the linewidth, particularly for the small features which are of the most interest; (2) the SEM is not an ideal metrology tool both because of the angle of the detector relative to the sample surface and because of its tendency to frequently go out of calibration; (3) while counting measurement-grating periods is easy in a macroscopic view, it is difficult to count them while mechanically moving the the SEM stage in a close-up configuration; (4) because cross sections cannot be taken, linewidth must be measured from the aerial image. Ambiguity is introduced by the finite, nonuniform, resist thickness.

This said, line and space widths for the nominal 0.2  $\mu\text{m}$  features were estimated from the SEMs in Figures 6.13 through 6.16; these are plotted along with the equi-irradiance curves from Figures 5.6 through 5.8 in Figures 6.17 through 6.19. Measurements were taken at the base of every grating line and widths were scaled to the 0.4  $\mu\text{m}$ -period grating. Considerable spread is seen in the data, which



is not surprising given the edge roughness of the patterns and the method of measurement. Qualitatively, the images of  $0.17 \mu\text{m}$  spaces begin to lose shape for  $G \geq 15\mu\text{m}$ , although the effect is not severe until  $G \simeq 18\mu\text{m}$ ; this is also where the equi-irradiance contours begin to diverge indicating decreasing slope in the diffraction profile.

Larger features were not measured because of the difficulties stated above, but the trend is clear: Patterns tend to deteriorate with the fanning out of the equi-irradiance contours. The diffraction theory outlined in Chapter 5 seems adequate for modeling these larger features. For the smaller features, the theory, as implemented, is inadequate in that linewidth oscillations are predicted which are not seen in practice.

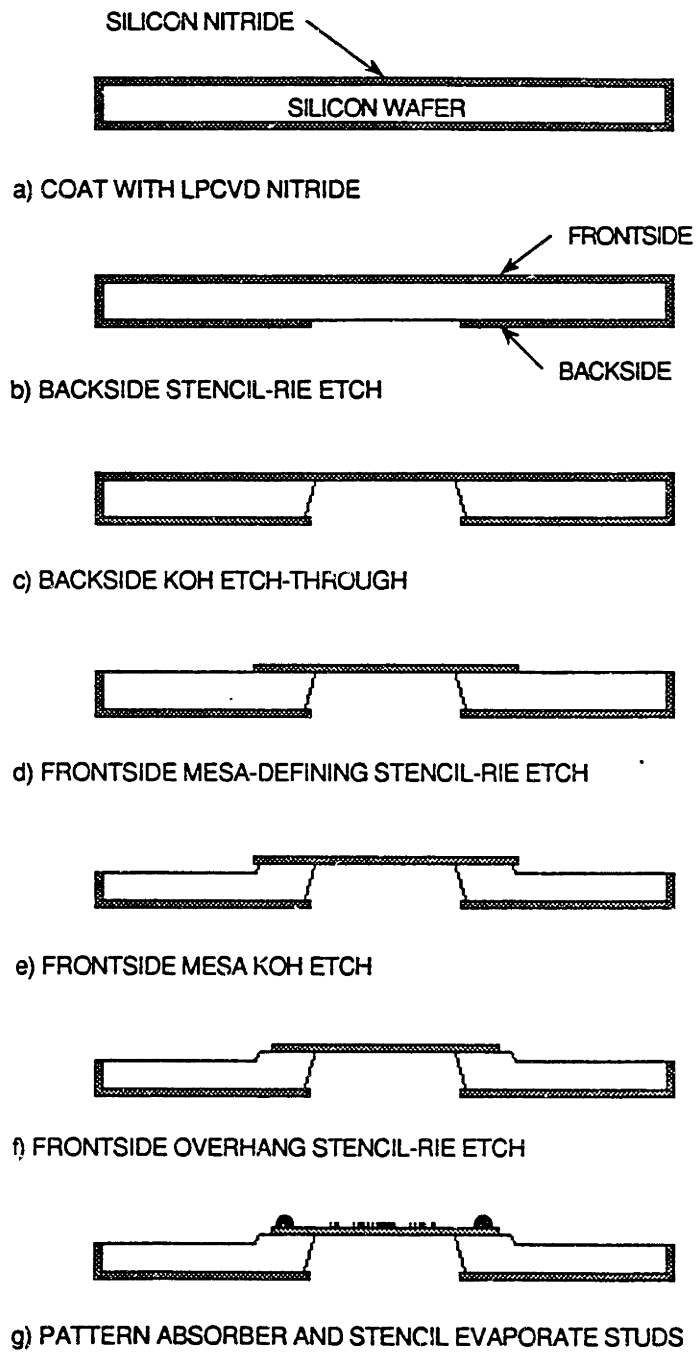
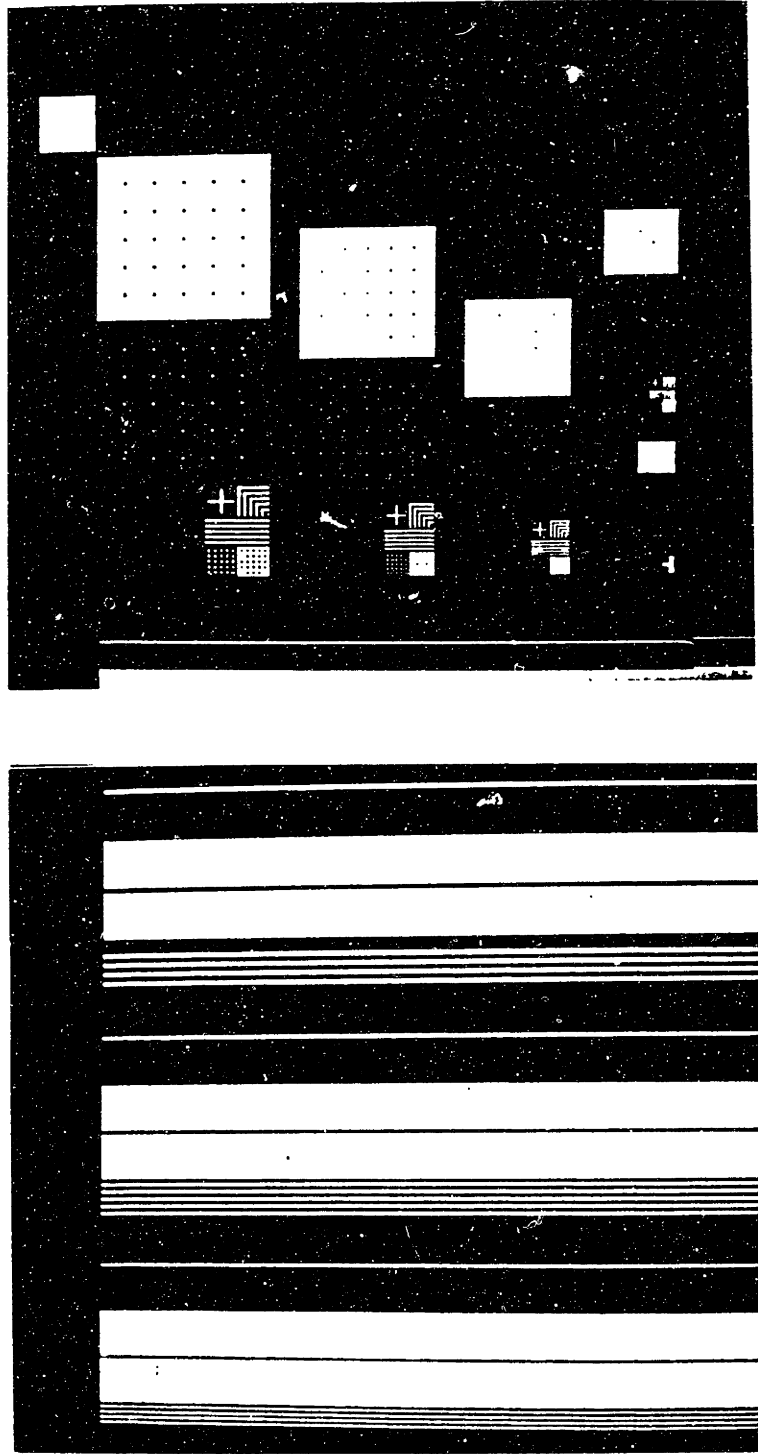


Figure 6.2: Mask Fabrication Sequence

**Figure 6.3: Mask patterns used in the diffraction experiments.**

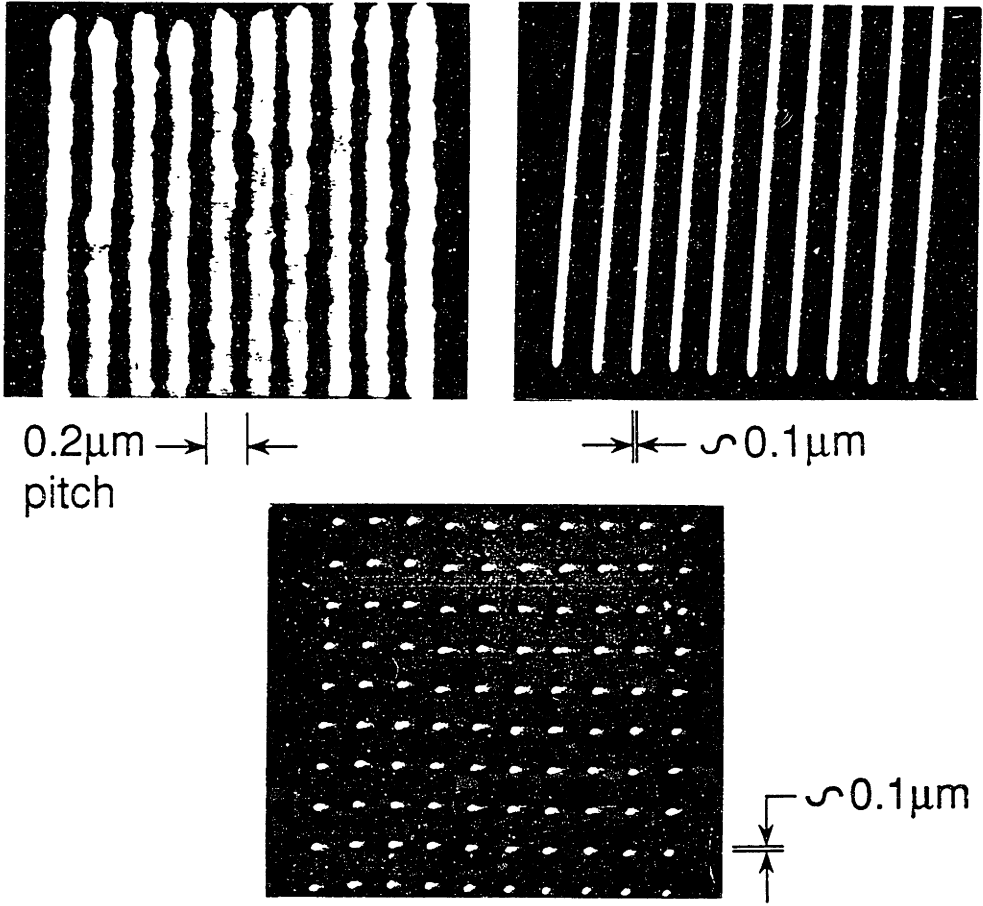
# Focused Ion Beam Mask Patterns



Patterns repeated for 0.5, 0.4, 0.3, & 0.2 $\mu\text{m}$  linewidths.

**Figure 6.4:** The mask patterns shown here were used in the resist characterization work presented in Chapter 3.

# FIB Mask Patterns



**$\sim 0.1\mu\text{m}$  Au Lines and Dots**

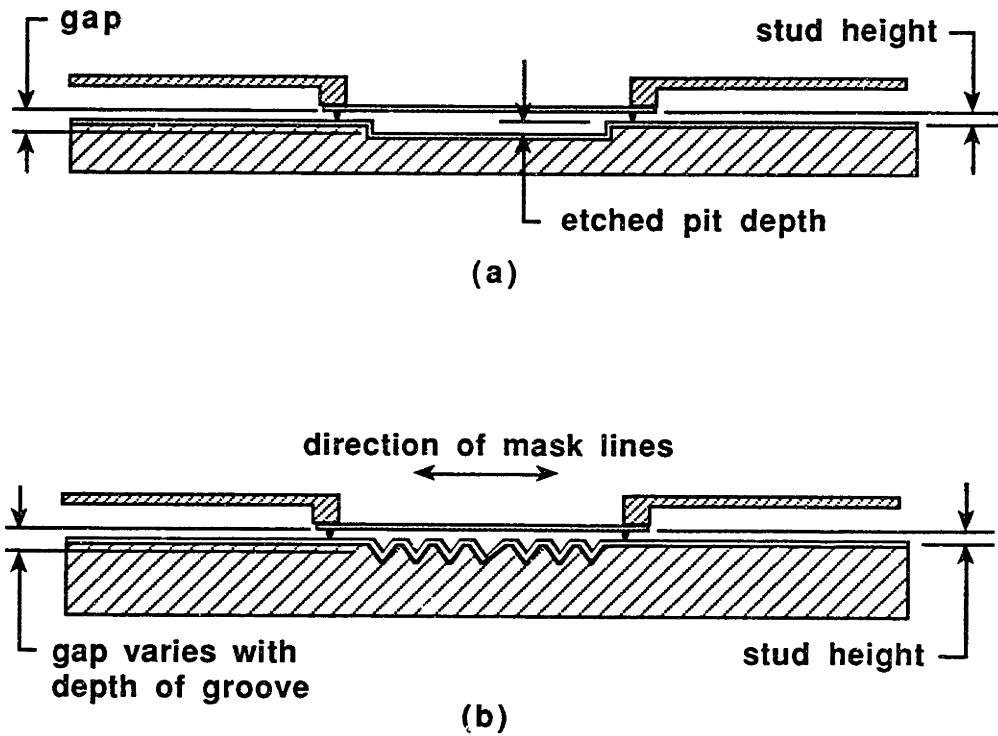
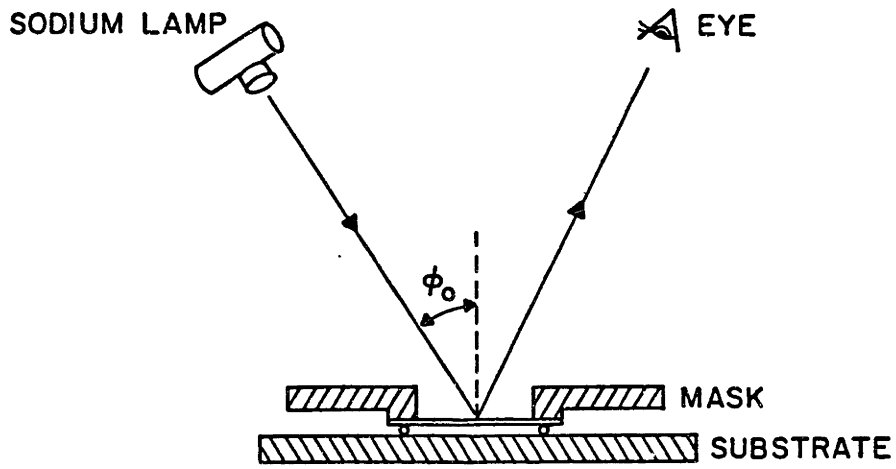
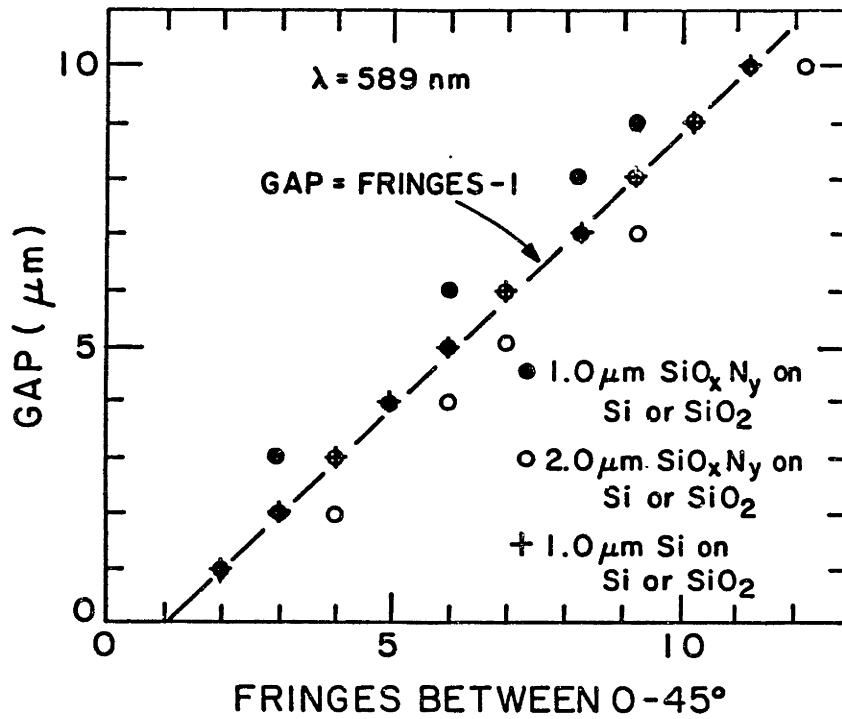


Figure 6.5: Gap-extending methods for diffraction experiments. In (a), a pit is etched in the wafer. In (b), v-grooves, etched into the substrate, provide sloped walls onto which the mask patterns are shadowcast.



(a)



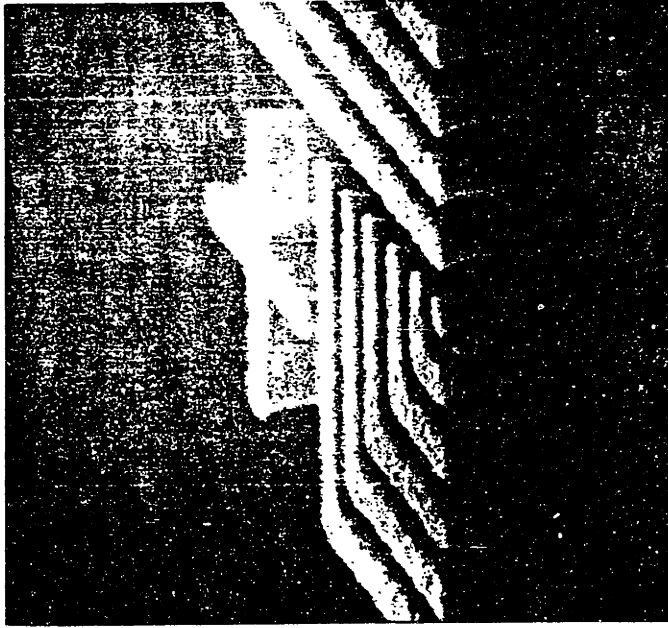
(b)

Figure 6.6: (a) Microgap measurement technique; (b) plot shows the number of fringes expected for a given gap for different membrane materials and thicknesses, from reference [27].

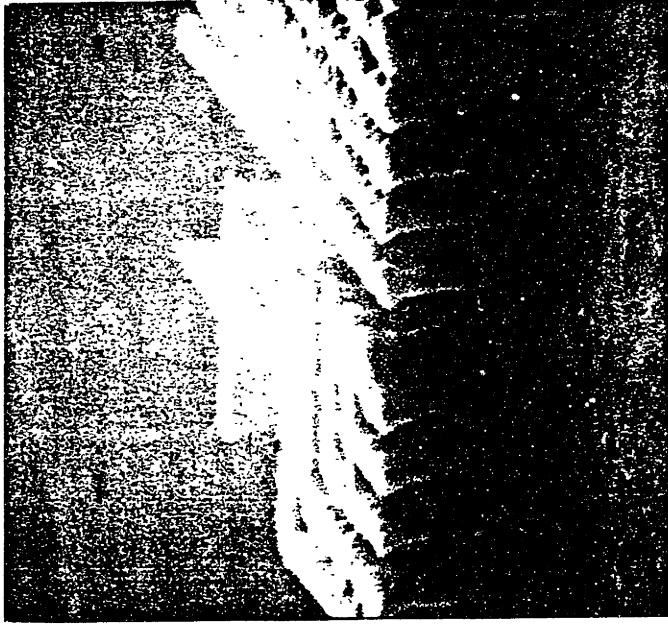


Figure 6.7: Ray-PF resist exposed at a 25  $\mu\text{m}$  gap.

# Features Exposed at 25 $\mu$ m Gap



**0.3 $\mu$ m linewidth**



**0.2 $\mu$ m linewidth**

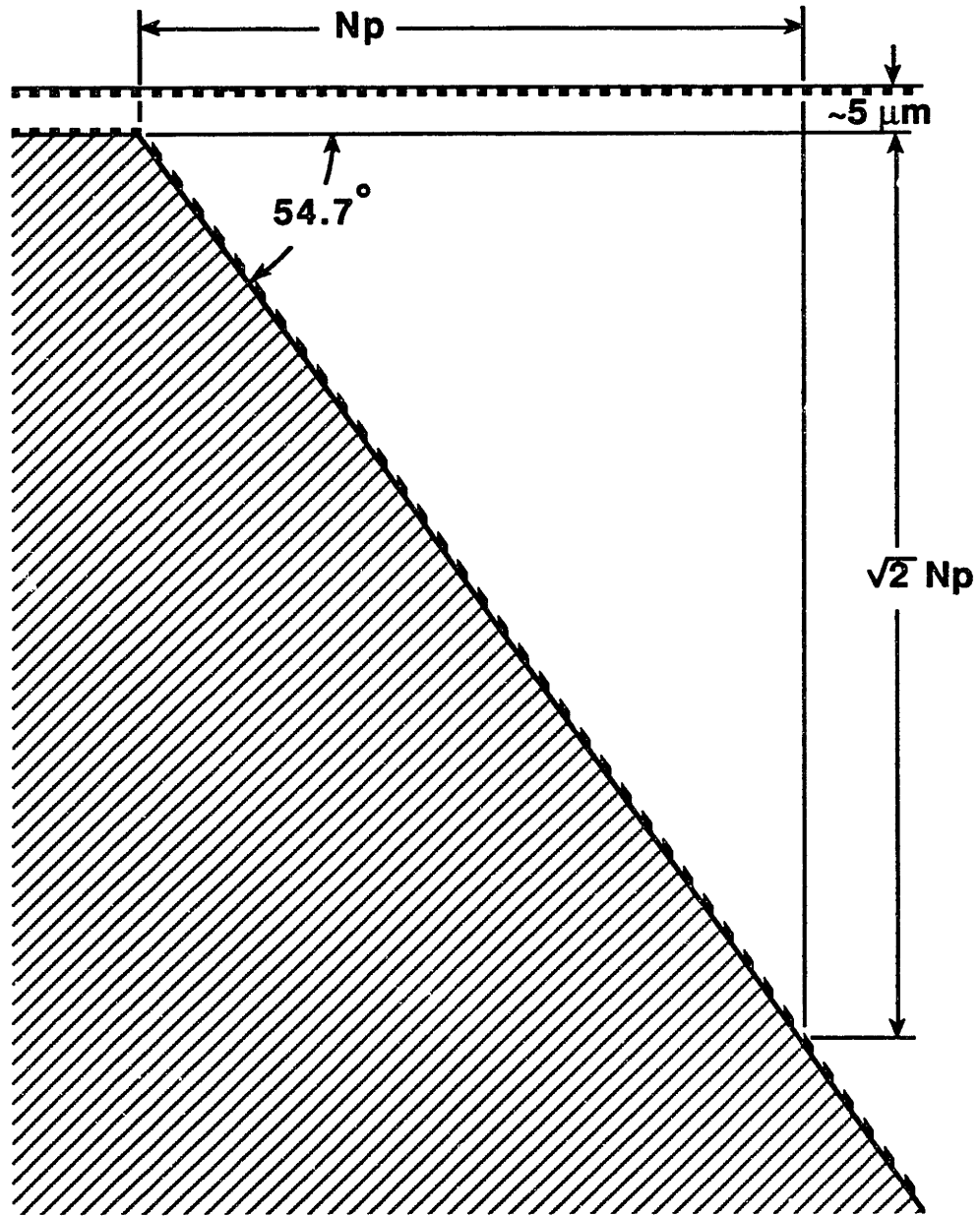
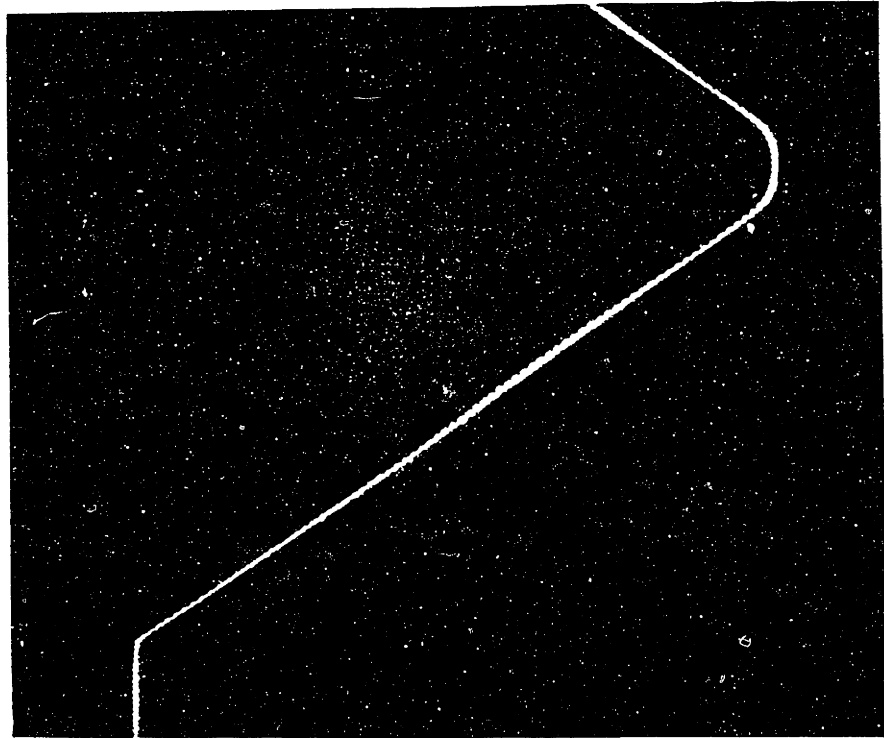


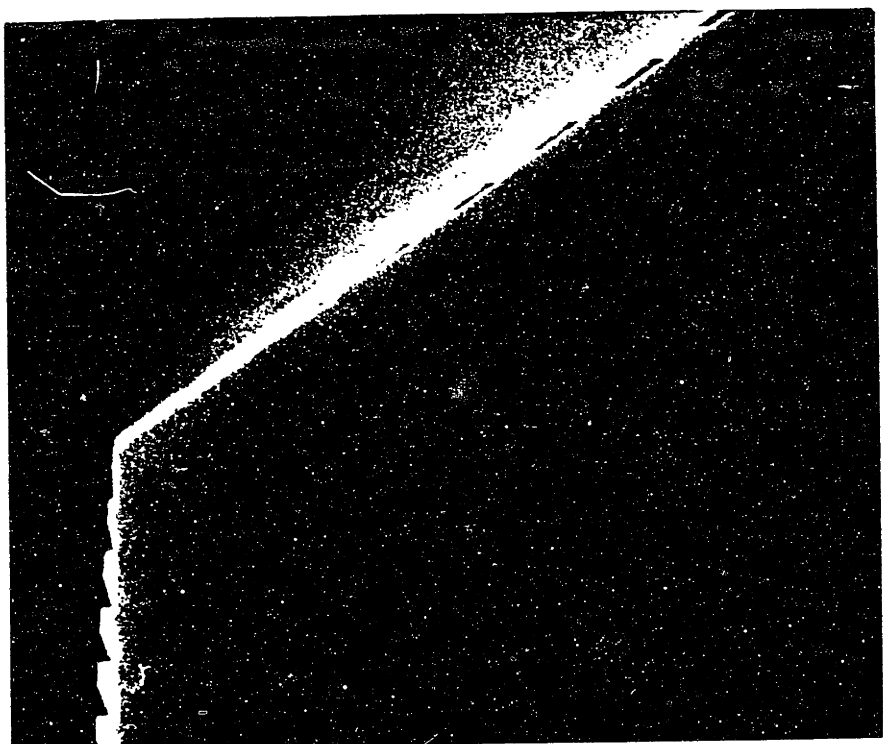
Figure 6.8: In v-groove experiment, gaps were calibrated by means of a grating which has a  $1 \mu\text{m}$ -period in the mask plane. The gap at any measurement point is  $G = (\sqrt{2}N + 5)\mu\text{m}$ .

Figure 6.9: Measurement grating exposure in Ray-PN resist: (a) The grating is resolved over the full depth of  $\sim 100 \mu m$ ; (b) One wall of the v-groove is only thinly coated with resist near the top. Compare this to the opposite wall shown in (b) of Figure 6.10.



50  $\mu\text{m}$

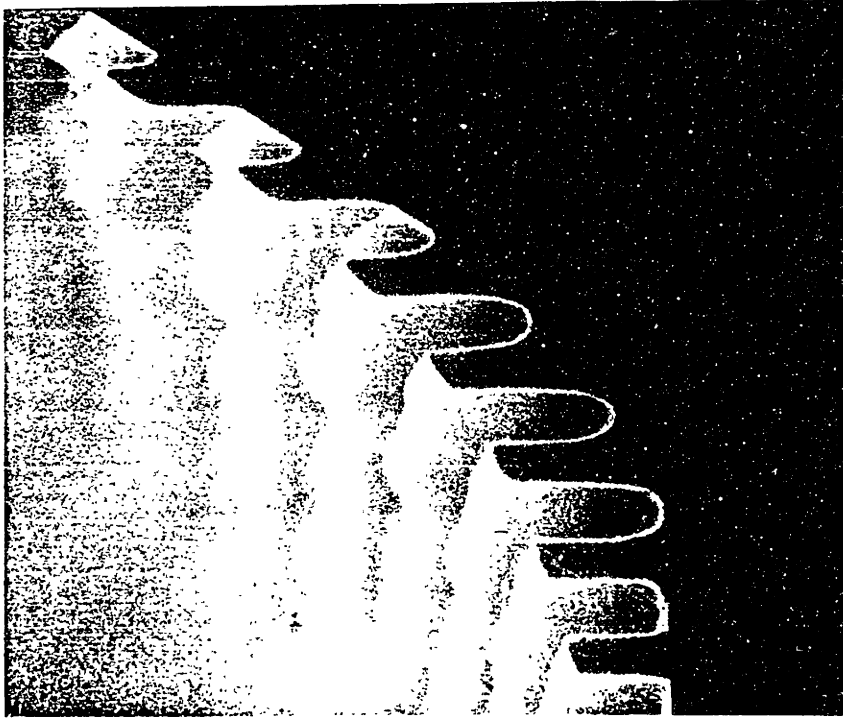
(a)



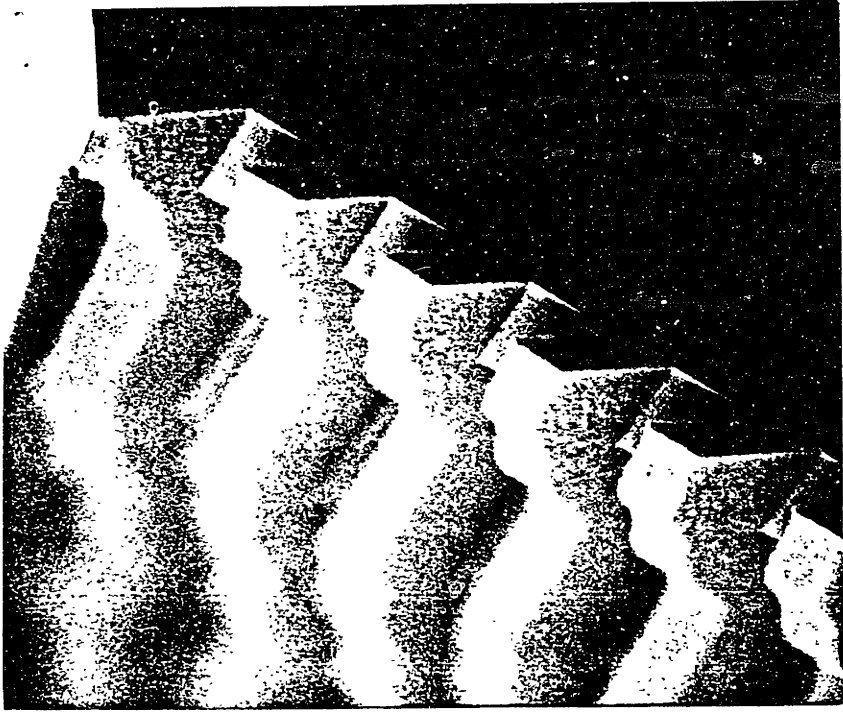
4.3  $\mu\text{m}$

(b)

**Figure 6.10: SEMs of the measurement grating in Ray-PN: (a) At the bottom of the groove; and (b), at the top of the groove.**



(a)



(b)

**Figure 6.11:** Mask pattern imaged, in Ray-PN resist, on a sloped wall. Dose = 24 mJ/cm<sup>2</sup>;  $5 \leq G \leq 100 \mu\text{m}$ . Nominal linewidths are: (a) 0.2; (b) 0.3; (c) 0.4; and (d) 0.5  $\mu\text{m}$ .



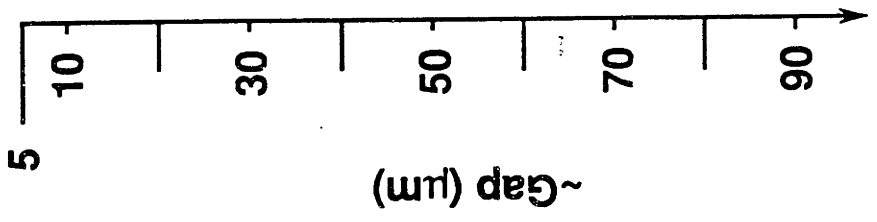
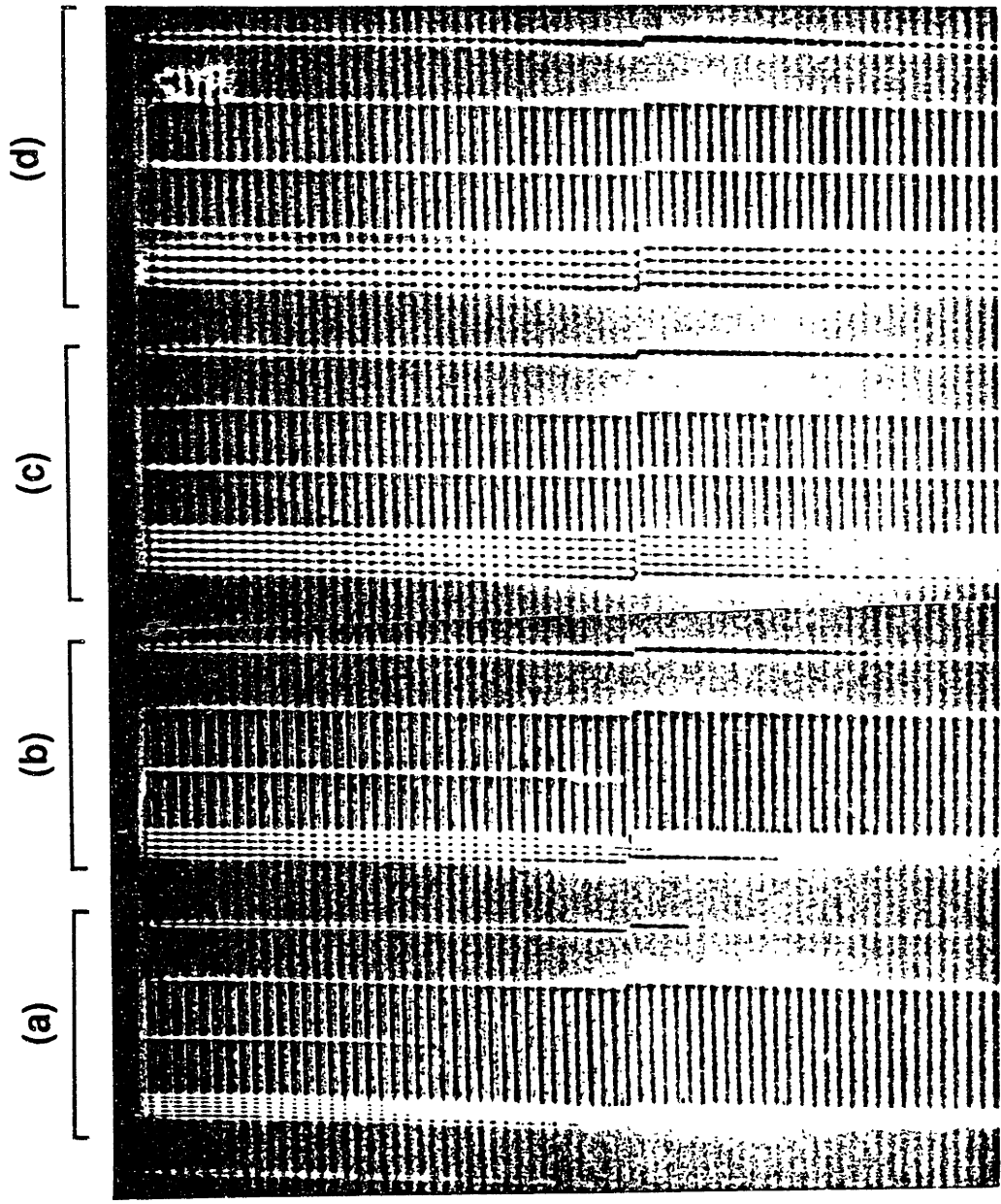


Figure 6.12: Mask pattern imaged, in Ray-PN resist, on a sloped wall. Dose = 26.4 mJ/cm<sup>2</sup>;  $5 \leq G \leq 100 \mu\text{m}$ . Nominal linewidths are: (a) 0.2; (b) 0.3; (c) 0.4; and (d) 0.5  $\mu\text{m}$ .

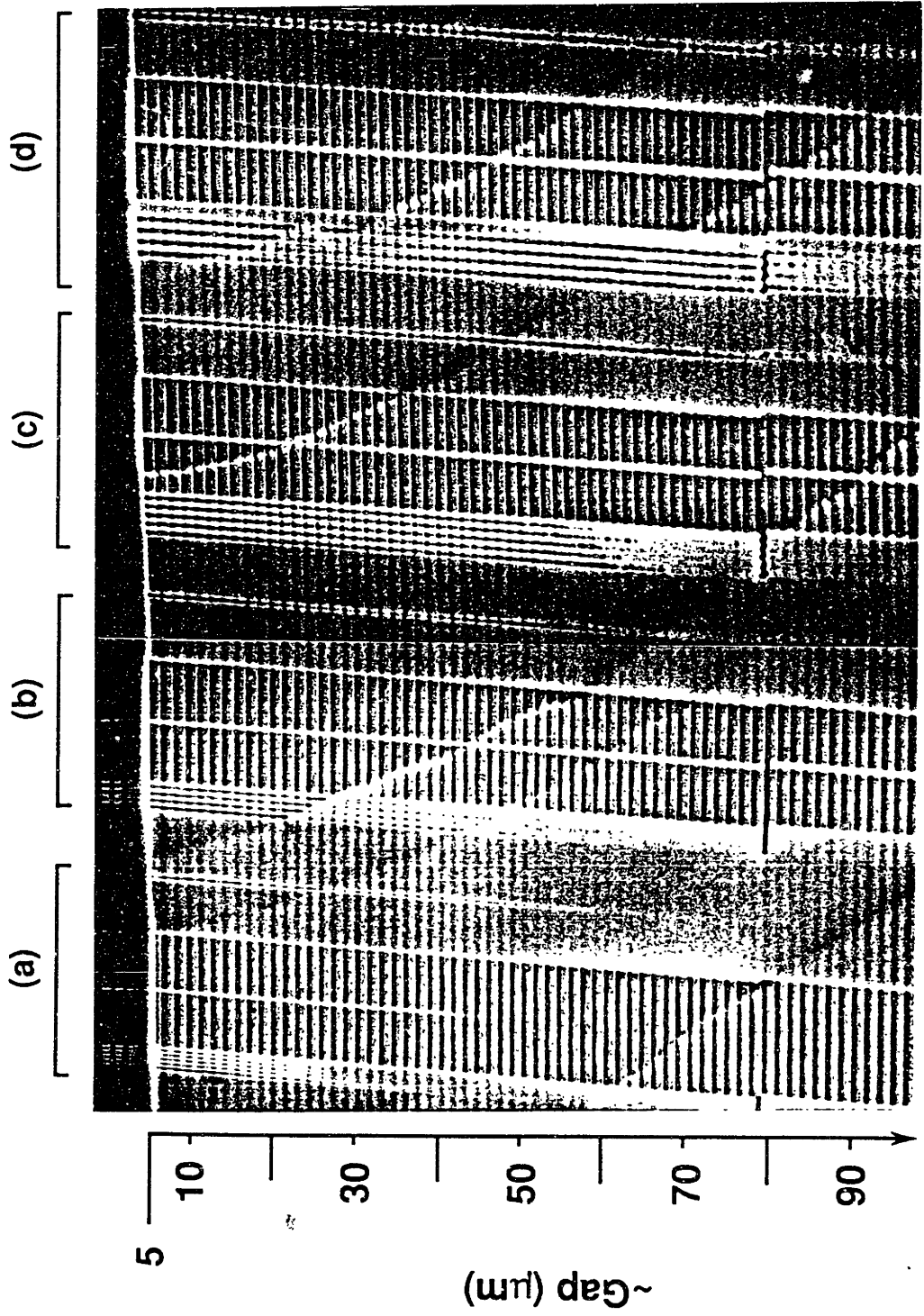


Figure 6.13: Images, on v-groove wall, of: 0.4  $\mu\text{m}$ -period grating with 0.17  $\mu\text{m}$ -wide spaces; a 0.17  $\mu\text{m}$ -wide space; and a 0.23  $\mu\text{m}$ -wide line.  $5 \leq G \leq 22$   $\mu\text{m}$ . Dose = 24  $\text{mJ}/\text{cm}^2$ .

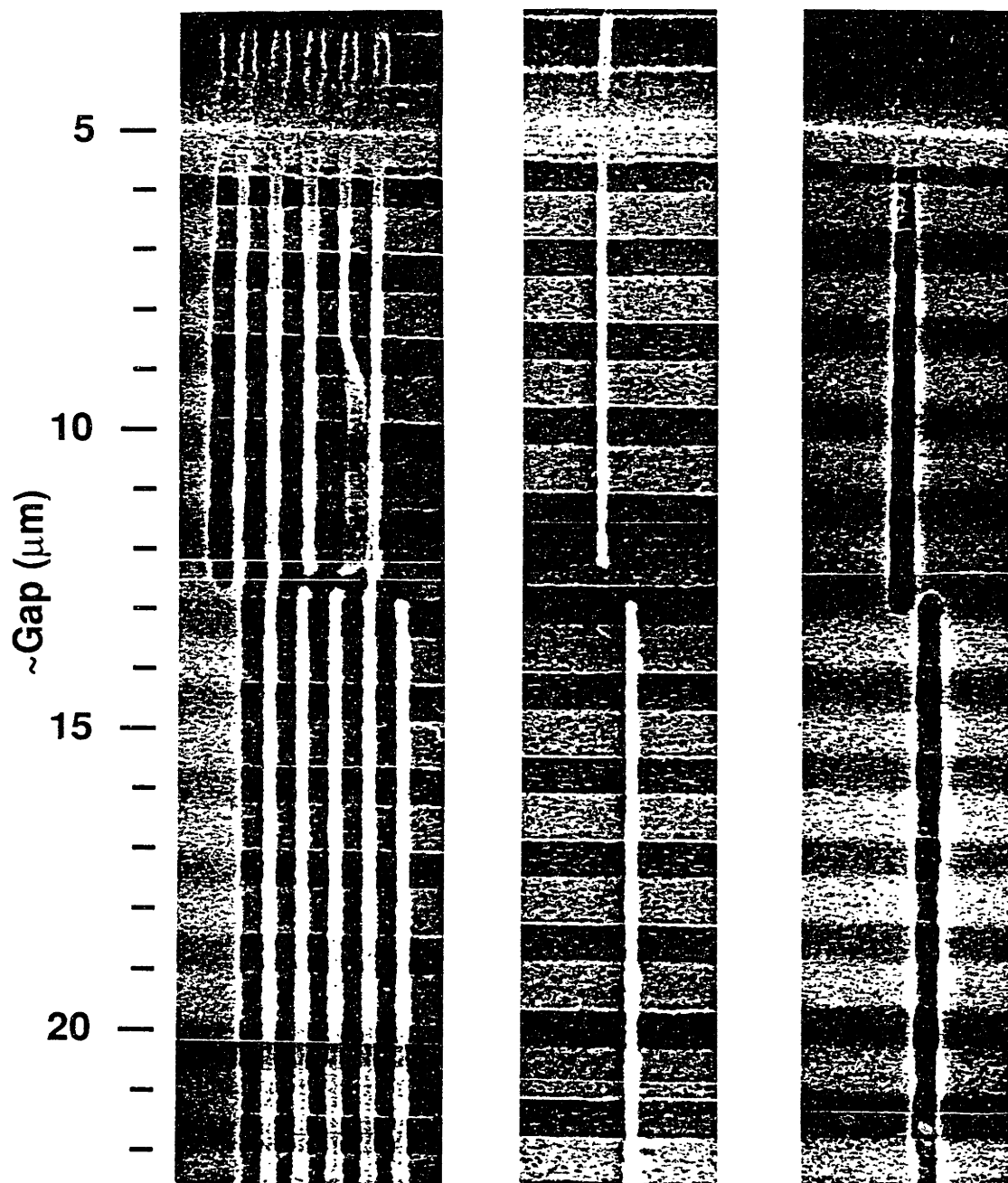


Figure 6.14: Images, on v-groove wall, of: 0.4  $\mu\text{m}$ -period grating with 0.17  $\mu\text{m}$ -wide spaces; a 0.17  $\mu\text{m}$ -wide space; and a 0.23  $\mu\text{m}$ -wide line.  $22 \leq G \leq 42$   $\mu\text{m}$ . Dose = 24 mJ/cm<sup>2</sup>.

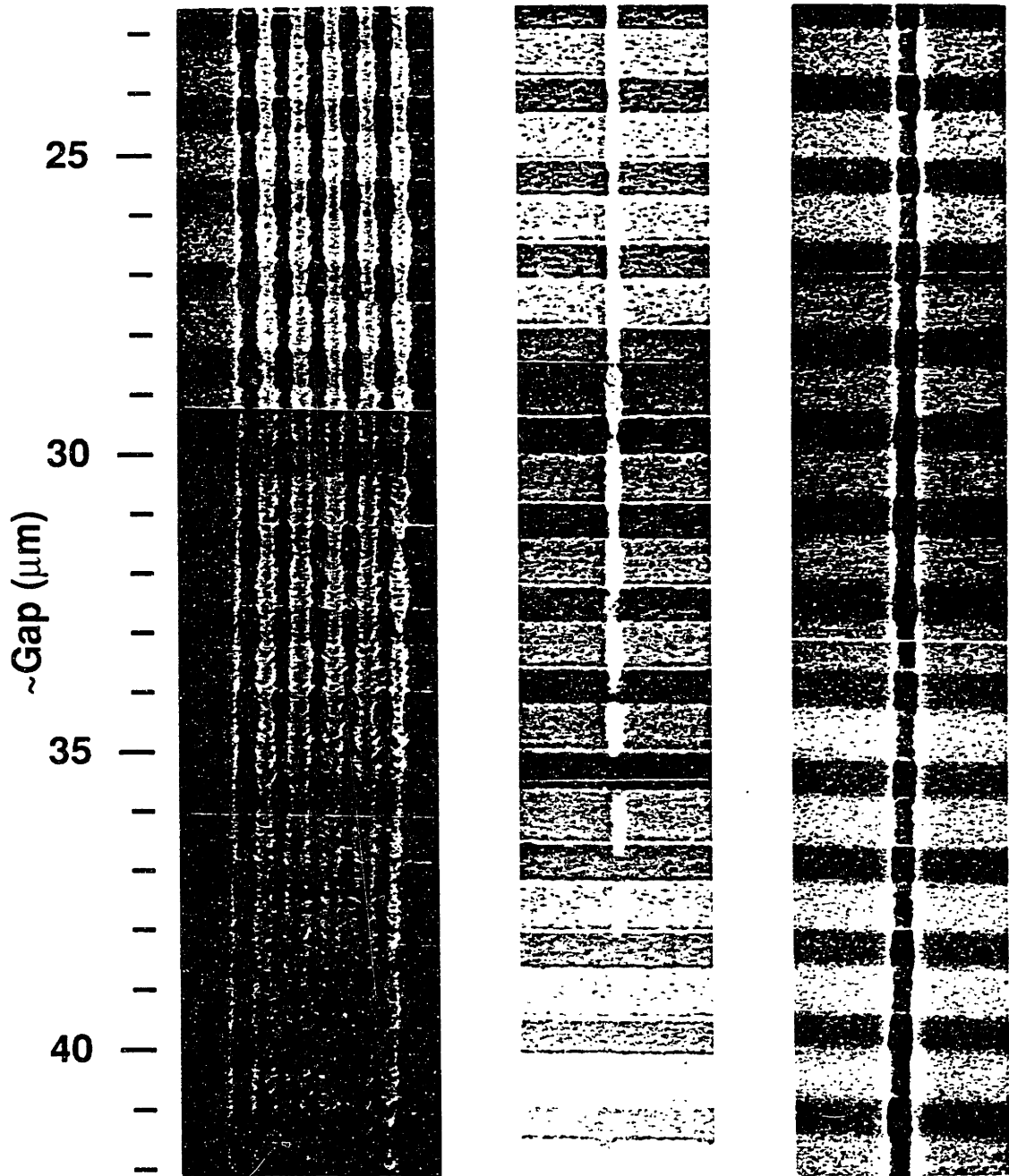


Figure 6.15: Images, on v-groove wall, of: 0.4  $\mu\text{m}$ -period grating with 0.17  $\mu\text{m}$ -wide spaces; a 0.17  $\mu\text{m}$ -wide space; and a 0.23  $\mu\text{m}$ -wide line.  $5 \leq G \leq 20$   $\mu\text{m}$ . Dose = 26.4 mJ/cm<sup>2</sup>.



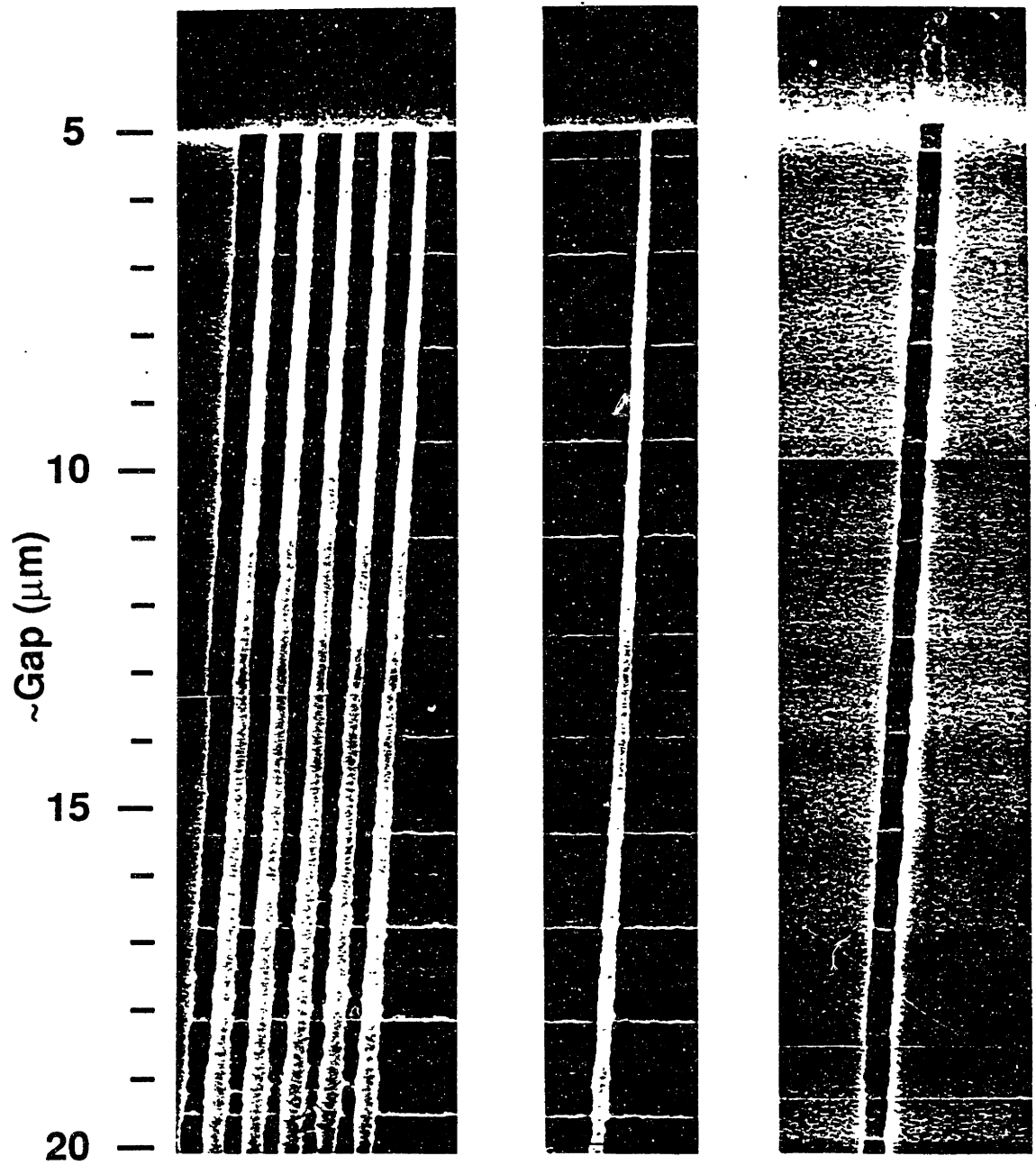
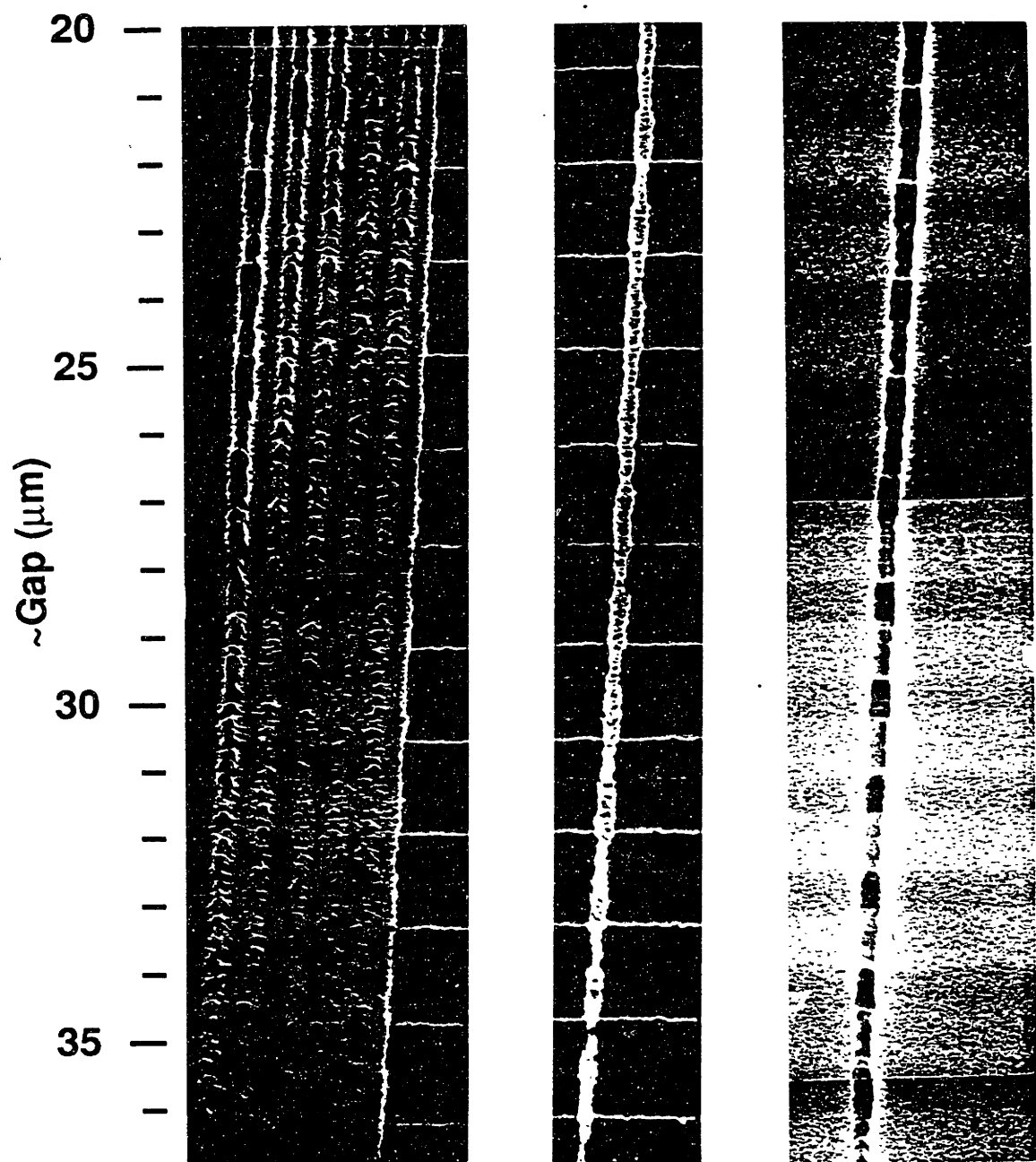


Figure 6.16: Images, on v-groove wall, of: 0.4  $\mu\text{m}$ -period grating with 0.17  $\mu\text{m}$ -wide spaces; a 0.17  $\mu\text{m}$ -wide space; and a 0.23  $\mu\text{m}$ -wide line.  $20 \leq G \leq 37$   $\mu\text{m}$ . Dose = 26.4  $\text{mJ}/\text{cm}^2$ .



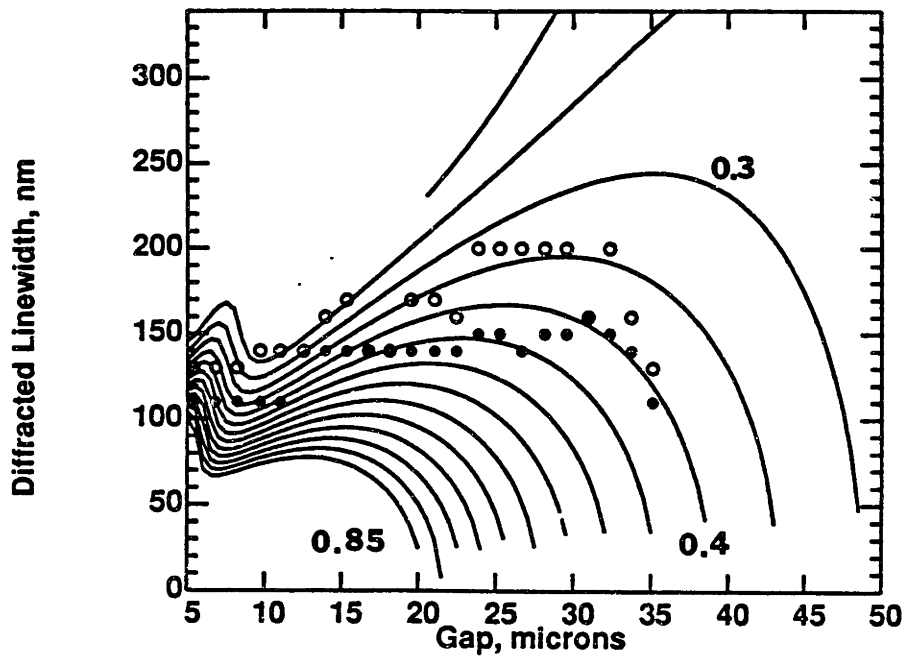


Figure 6.17: Calculated equi-irradiance contours and measured image widths for the  $0.17 \mu\text{m}$ -wide slit. Closed and open circles are for the  $24$  and  $26.4 \text{ mJ}/\text{cm}^2$  doses, respectively.

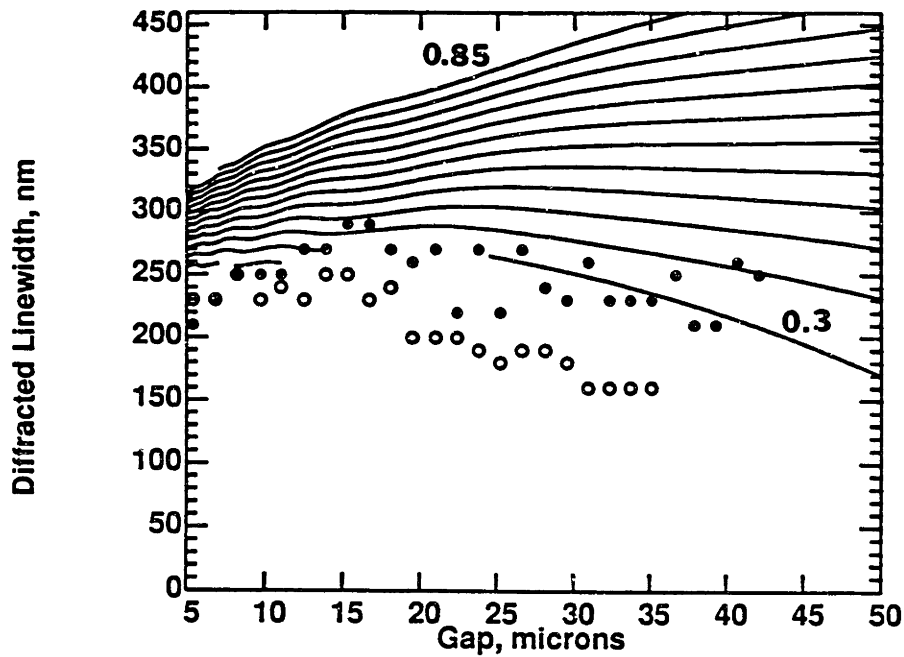


Figure 6.18: Calculated equi-irradiance contours and measured image widths for the  $0.23 \mu\text{m}$ -wide line. Closed and open circles are for the  $24$  and  $26.4 \text{ mJ}/\text{cm}^2$  doses, respectively.

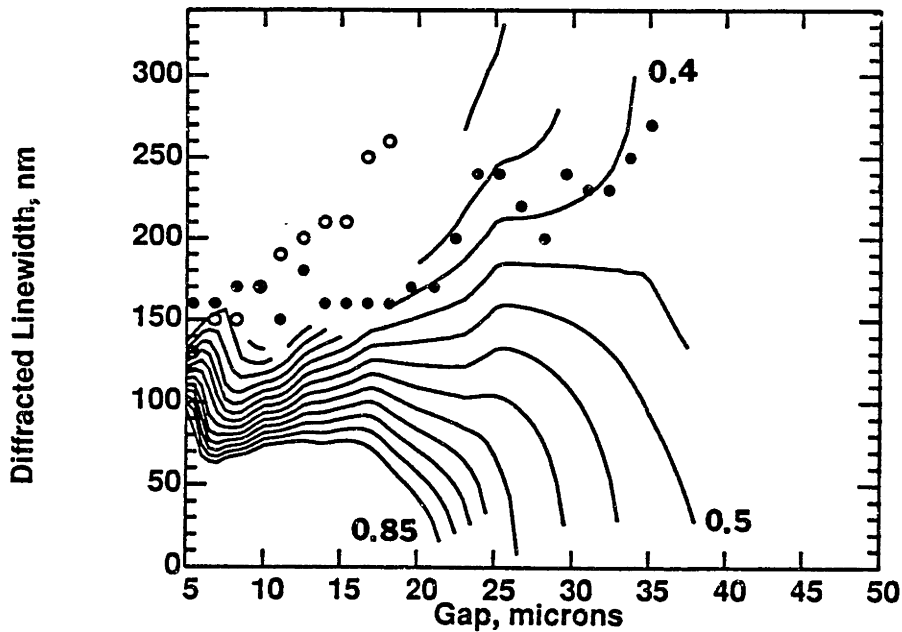


Figure 6.19: Calculated equi-irradiance contours and measured image widths for the  $0.4 \mu\text{m}$ -period grating with  $0.17 \mu\text{m}$ -wide spaces. Closed and open circles are for the  $24$  and  $26.4 \text{ mJ}/\text{cm}^2$  doses, respectively.

# Chapter 7

## Summary and Future Work

The object of this dissertation has been to further our knowledge of resolution limits in x-ray lithography, and a number of contributions in that direction have been made. For the first time, 30 nm-wide lines were imaged using  $Al_K$  radiation thus demonstrating that wavelengths as short as 0.8 nm can be used for sub-100 nm lithography, though wavelengths closer to the  $Cu_L$  lines ( $\lambda = 1.3$  nm) are preferable for reasons of ease of mask fabrication and increased process latitude.

In the work with the new chemically amplified resists, 100 nm-wide lines were resolved for an x-ray dose of only  $5 \text{ mJ/cm}^2$  in a  $1 \mu\text{m}$ -thick film. This low dose corresponds to  $\sim 100$  photons/pixel where the pixel is taken to have 100 nm height and an area equal to the linewidth squared. In 1980, Flanders [8] imaged 17.5 nm-wide lines in PMMA resist at a dose of  $\sim 30,000$  photons/pixel. The Ray-PF exposure in this thesis shows two orders of magnitude decrease in required photon dose and establishes an empirical minimum. Using this minimum, resolution limits for other resist were estimated. The combined effects of shot noise and image contrast were considered and based on these, more conservative resolution limits were recommended for industry.

The most controversial topic in x-ray proximity printing is the maximum acceptable gap at which a given feature size can be printed. Phrased differently, at

what point does diffraction induced image degradation become prohibitive? The answer to this question has been unclear in part because of a lack of sufficient experimental data, and in part because there is no single agreed upon criterion for the meaning of "acceptable."

Lin [72,75] has put forth the criteria of the resolvability of a family of five different features to within  $\pm 10\%$  of the mask dimensions. This seems overly conservative in that, in a manufacturing situation, a single mask level typically contains only a single critical feature. Examples from what are usually the two most critical levels are transistor gate length and contact hole diameter. Also, there is no inherent reason to tie mask feature size to image size; as long as the desired linewidth in the image is obtained, the mask and image dimensions can vary. What cannot be allowed to vary is the imaged linewidth over the area of the chip. Assuming a perfect mask, such variations in the image could be caused by intensity and gap fluctuations across the image field.

In this thesis, a new technique was introduced for obtaining diffraction data for all gaps of interest in a single exposure. A mask image, consisting of gratings, isolated lines, and isolated spaces, was shadow cast onto a sloped wall. This technique has the advantage over multiple exposure experiments of eliminating error due to slight differences in resist processing and exposure conditions. The mask used for this experiment contained features of four different sizes, the smallest of which were  $0.17 \mu\text{m}$ -wide spaces which were shown to print to gaps as large as  $35 \mu\text{m}$  though image quality began to deteriorate significantly at  $\sim 18 \mu\text{m}$ . Change in linewidth appears to be a slowly varying function of gap, and no diffraction induced oscillations in linewidth were detected. A change in dose of  $10\%$  appears to produce as much as  $30\%$  change in linewidth for a gap of  $15 \mu\text{m}$ . Because of the complicated processing of the resist, the linewidth difference cannot, at this point, be unequivocally attributed to diffraction; with such a low source brightness and such long exposure times, the doses may actually have varied by more than the

intended 10%. A critical evaluation of the effect of intensity fluctuations in the mask plane is needed.

Using angular spectrum of plane waves calculations, theoretical linewidth-gap plots were generated where each plot contained a family of equi-irradiance contours of diffracted linewidth as a function of gap. The experimental exposures were compared against these plots, and it was seen that the resist image deterioration correlated well with the divergence of the equi-irradiance contours. This suggests that the edge slope of the diffracted image and the image contrast are the yardsticks by which acceptable gap should be measured, rather than the correlation between mask and image sizes as suggested by Lin.

The results of the diffraction experiment are encouraging, but more work needs to be done in this area with masks of better quality, and with two dimensional patterns. The straightforward one-dimensional diffraction calculations implemented here should be extended to two dimensions. The sloped wall experiment suffered from lack of uniformity in the resist thickness caused by the steep angle of the (111) planes relative to the wafer surface. If (110) substrates were used instead of (100), the angle would be reduced from  $54.7^\circ$  to  $35.3^\circ$ . This would probably significantly improve resist uniformity. This type of experiment generates a tremendous amount of data, but at present no automated linewidth measurement tool of sufficient resolution is available to record the data; such a tool would be of tremendous value.

The large depth of focus exhibited in the diffraction experiments, which is primarily due to the short wavelength, makes it likely that x-ray proximity printing will always have a niche in semiconductor microfabrication. Whether and when x-ray proximity print will take over the role that DUV reduction lithography plays in chip manufacturing is not answerable at present. The continued improvements in mask membrane technology, mask writing capabilities, coupled with automatic gap control and mask alignment techniques are pushing in the direction of industry



wide viability, and for that reason, further evaluation of resolution limits should be undertaken.

# Appendix A

## Ray-PF and Ray-PN Processing

Ray-PF and Ray-PN, the chemically amplified resists (CARs) used in this thesis, are manufactured by the Electronic Products Division of Hoechst Celanese Corporation. These resists have a shelf life of about six months if refrigerated. Process flow schematics for the two resists are shown in Figure A.1.

Wafer preparation and processing are done as follows:

1. Clean wafers are dehydration baked on a hotplate at a low setting.
2. Hexamethyldisilazane (HMDS) is spun-on at a few kRPM for twenty seconds. The wafers are then oven-baked for 30 minutes at 80°C. The purpose of this bake is to drive off the ammonia that is a byproduct of the hydrophobisation reaction of HMDS with the OH groups; ammonia, if present in the exposed film, can inhibit development of the bottom layer of the resist [63]. For good adhesion, CAR should be spun onto a chemically neutral, acid free surface [63]. Acid present at the interface can cause “exposure” of the resist; a base can prevent “exposure.” Because we spin on HMDS, rather than vapor priming the surface, ammonium salts may be left behind even after the oven bake. If this happens then the use of HMDS will actually prevent good adhesion of Ray-PN and will cause a scum to remain at the wafer/resist

# Process Flow

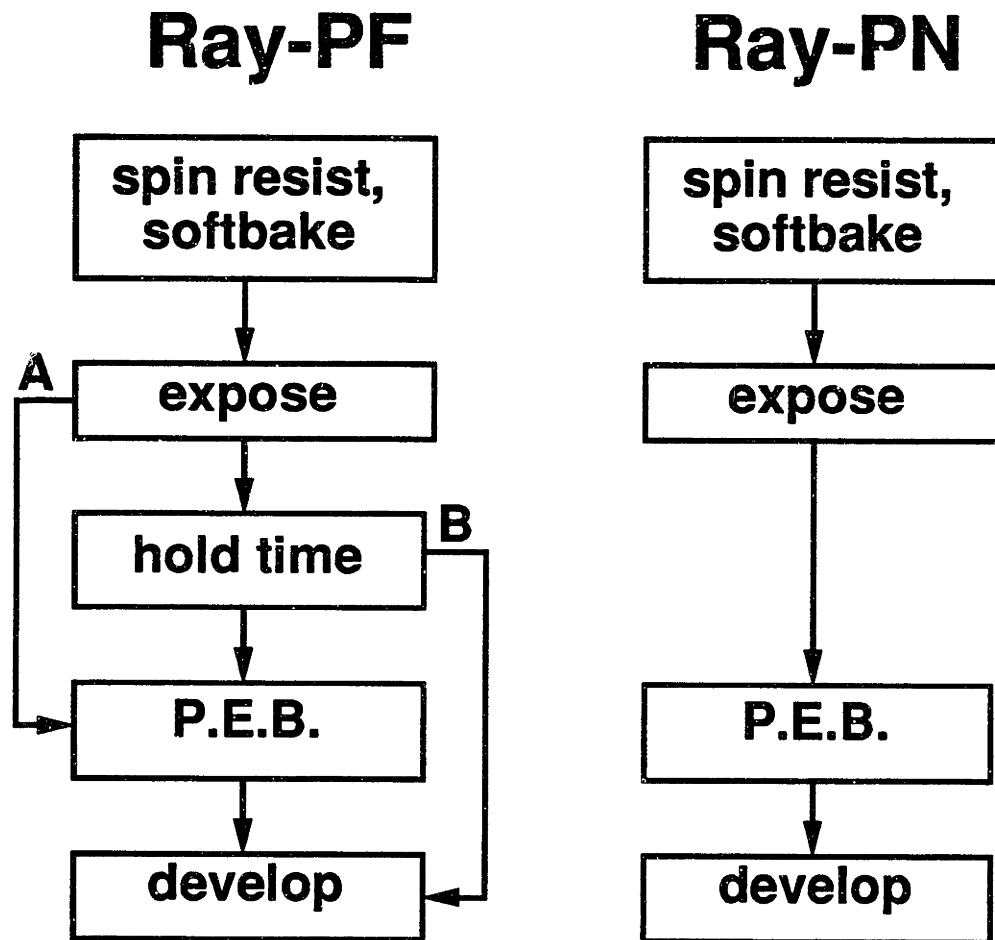


Figure A.1: Process flow for Ray-PF and Ray-PN. In the Ray-PF diagram, branch A corresponds to the case of short vacuum time where the hold time can be set to zero; branch B indicates that the PEB is not strictly required for Ray-PF provided the hold time is sufficiently long (at least on hour). For Ray-PN no hold time is required the PEB is mandatory because the acid catalyzed reaction does not go forward at room temperature.

interface after development of Ray-PF.

3. A puddle of resist, about the size of a half-dollar, is deposited at the wafer center and the resist is spun for 30 seconds. For Ray-PF and Ray-PN, a 1  $\mu\text{m}$ -thick film is obtained at 5 and 7kRPM respectively. Films in the 0.25 to 0.5  $\mu\text{m}$ -thickness range can be obtained by diluting the resist with AZ Thinner or Shipley Type A Thinner. Spin curves for various thicknesses and dilutions are shown in Figures A.2 and A.3.
4. Immediately following spinning each wafer, the sample is baked for one or two minutes on a vacuum-chucked hotplate to drive-off solvents. For consistent results, the time and temperature must be kept constant to within a couple of seconds and a couple of degrees. A variation of 5 to 10°C will significantly alter the sensitivity of the film. Good results have been obtained for a one minute bake time and a hotplate setting of 130°C. At this hotplate temperature, the thermocouple at the center of the aluminum vacuum-chuck block typically reads  $122 \pm 1^\circ\text{C}$ . A two minute bake will reduce the resist sensitivity and should only be considered in the case of adhesion problems that cannot be solved any other way. At present, only the chucked hotplate temperature is controlled; the room temperature can vary by several degrees from day to day and this may influence the resist sensitivity.

For films of 0.4  $\mu\text{m}$ -thickness or less, the sample can be oven baked at 80°C for 30 minutes. Films baked in this manner may be more sensitive. For thicker films this method will not completely drive-off the solvents.

5. At this point the wafers are ready for exposure. For a 1.0  $\mu\text{m}$ -thick film exposed with 1.3nm x-rays, typical doses are of the order of 5  $\text{mJ}/\text{cm}^2$  for Ray-PF and 20 $\text{mJ}/\text{cm}^2$  for Ray-PN. Ray-PF has been shown to lose sensitivity in vacuum at the rate of about 4% per hour [63].
6. Post-exposure processing of Ray-PF and Ray-PN differ. In either case a

“dark reaction,” during which chemical amplification occurs, must take place prior to resist development. Upon absorption of x-ray photons, a catalytic acid is generated in the resist. During the dark reaction, in the presence of the catalyst, the dissolution inhibitor (enhancer) is converted to a substance dissolvable (indissolvable) in the developer [57-60].

For Ray-PF, the dark reaction takes place at room temperature. Typically, after removal from the x-ray system, an exposed wafer is allowed to sit in air at room temperature for an hour. After this hold time, the wafer is baked on the vacuum-chuck hotplate for one minute at a hotplate setting of 70°C. The purpose of the post-exposure-bake (PEB) is to ensure that the reaction is driven to completion. The hour wait time is required prior to the bake only for long exposure times in vacuum. During the hold time the resist reabsorbs moisture, necessary to the catalytic reaction, from the room air.

For Ray-PN, energy must be added to the system for the reaction to go forward. The PEB in this case is five minutes at a hotplate setting of 115°C. The thermocouple in the vacuum-chuck will read ~ 110°C.

7. The sample is next immersion-developed in AZ developer diluted with deionized water at a ratio of 1:1 or 1:2. In the SSL, best results to date have been obtained with developer:DI ratio of 1:1. Typical development times are from 1.5 to 3 minutes for Ray-PF and 2.5 to 8 minutes for Ray-PN.

For Ray-PF, a higher x-ray dose will lead to a shorter development time. However, samples that develop out in 90 seconds usually show undercutting or hourglassing of the resist profile. This hourglassing causes 0.1  $\mu\text{m}$  posts to pinch apart at the center. Vertical profiles are obtained for samples that develop out in 2.5 minutes.

For Ray-PN, development times of 2.5 to 5 minutes give good results for 1  $\mu\text{m}$ -thick films. Note that when a negative resist is used in conjunction with

a 10db-attenuating x-ray mask, an overly long exposure time reduces the contrast of the resist. This happens because the background dose generates enough acid to lead to some crosslinking of the areas to be developed away. Thus the relative solubility of exposed and unexposed regions decreases.

Because the development times are long, spray development is not practical. For either resist, immersion development with fairly vigorous agitation is recommended, especially during the first minute to aid in breaking through the surface layer of the resist. Examination of the developing sample with a fiber light shining through the side of the beaker facilitates endpoint detection. During development, the surface regions where resist is developing away becomes grainy and mottled. Development is complete when the smooth shiny wafer surface appears in those regions.

The process-flow presented in this appendix was developed by testing and following procedures outlined in references [41,57-61,63]. Reference [60] contains additional information on UV hardening of Ray-PF for purposes of electroplating and on resist sensitivity to exposure with DUV and e-beam. In addition to their good resolution and high sensitivity and contrast, these resists have the excellent etch resistance associated with novolak resists.

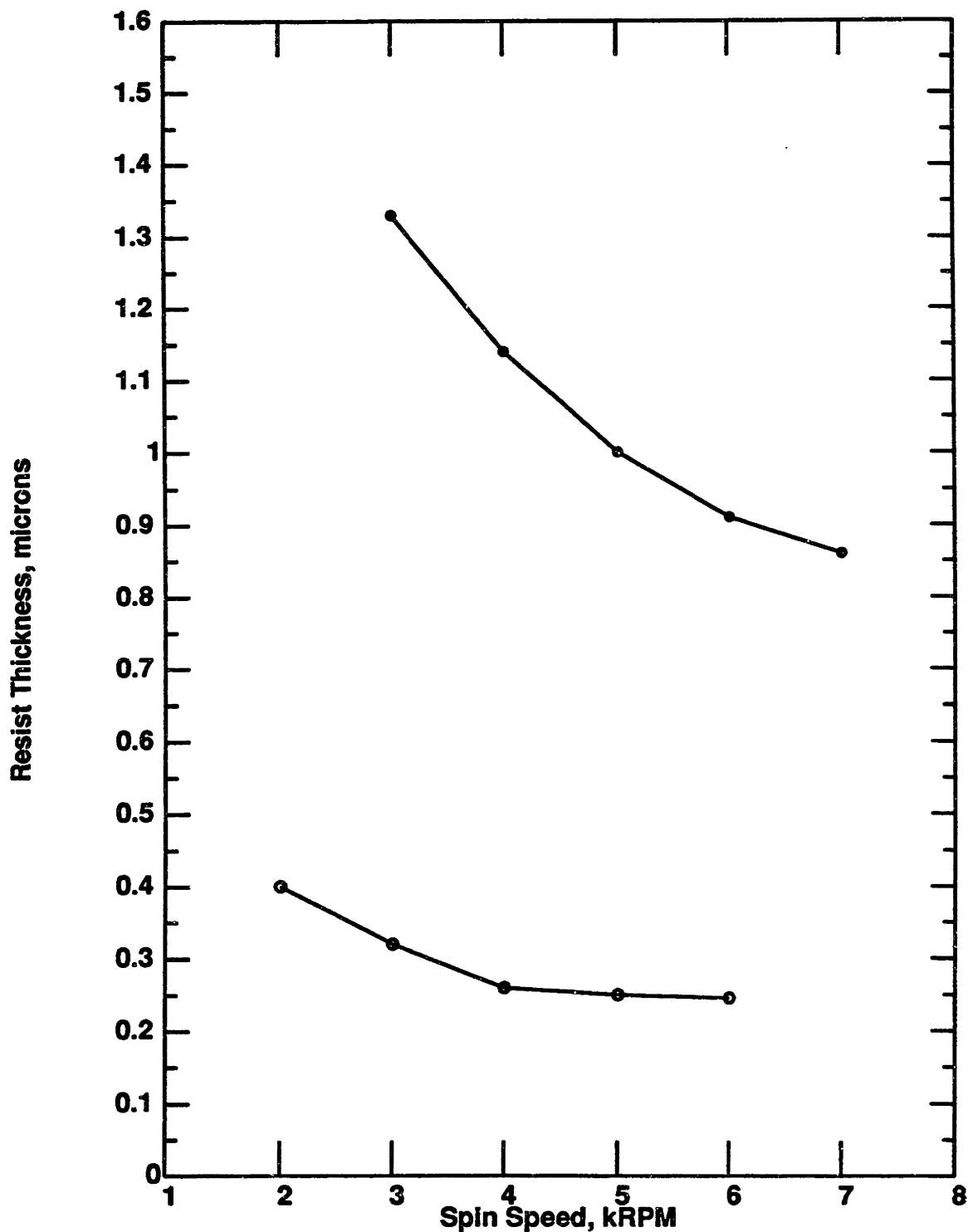


Figure A.2: Spin curves for Ray-PF. Thicknesses were measured after solvent drive-off bake. Bottom curve is for resist diluted 1:1 with Type A Thinner.

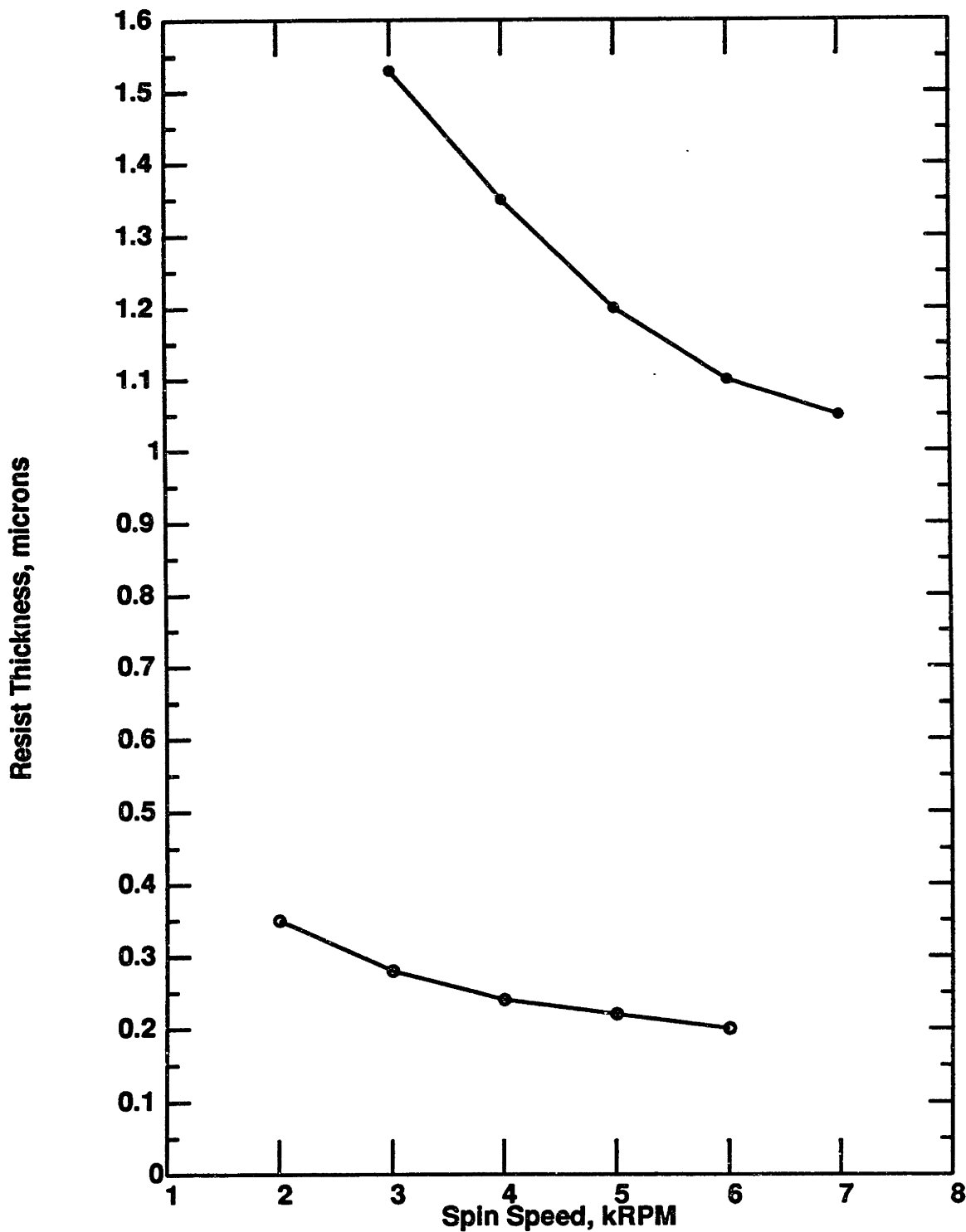


Figure A.3: Spin curves for Ray-PN. Thicknesses were measured after solvent drive-off bake. Bottom curve is for resist diluted 1:1 with Type A Thinner.



# Appendix B

## Polyimide Maskmaking

The following is a description of how to make polyimide contact masks of the type used in the photoelectron range experiment [6,36] as well as the type in which both sides of the mask membrane are patterned [37,91,92]. The second type was fabricated in collaboration with Gee Rittenhouse for patterning a resonant tunneling device [91,92]. In either case, fine lines on the mask are produced by sidewall shadowing of a grating which is formed using a (110) silicon wafer for the mold; if both sides of the mask are patterned, the gross geometry of the devices is formed through optical lithography and lift-off on the reverse side of the mask membrane. Mask making steps are given below:

1. Begin with (110) wafers coated with 30 nm of thermal  $\text{Si}_3\text{N}_4$ . It is best to start a mask run with six wafers because of the potential for losing one or more during fabrication.
2. Prime wafers with HMDS. Spin-on 0.25 – 0.5  $\mu\text{m}$  of Shipley resist; softbake for 25 minutes at 90°C.
3. Pattern wafers using a grating of appropriate period. This can be done using either a flex-mask under the Tamarac in the SSL, or with a glass mask under the Karl Suss in TRL. In either case the grating lines must be aligned

parallel to either of the sets of (111) planes which are perpendicular to the wafer surface. Manufacturers will place the wafer flat either along one of these sets of planes, or at the angle bisecting the two sets of perpendicular planes.

4. Spray-develop using Shipley 351 developer diluted 1:5 with DI for 45 seconds; rinse with DI for 45 seconds.
5. Plasma etch the nitride in the SSL RIE with  $\text{CHF}_3$ . Typical process parameters are: 15sccm, 10 mTorr, 600  $V_{\text{DC}}$ , 1.0  $V_{\text{pp}}$ , 75 Watts, 70 seconds etch time. It is best to run a monitor prior to etching. Incomplete nitride etching will ruin the run; excess nitride etching can cause gouging of the silicon near the nitride step edge.
6. Strip the resist with  $\text{O}_2$  in the plasma asher or the RIE (Figure B.1 (a)).

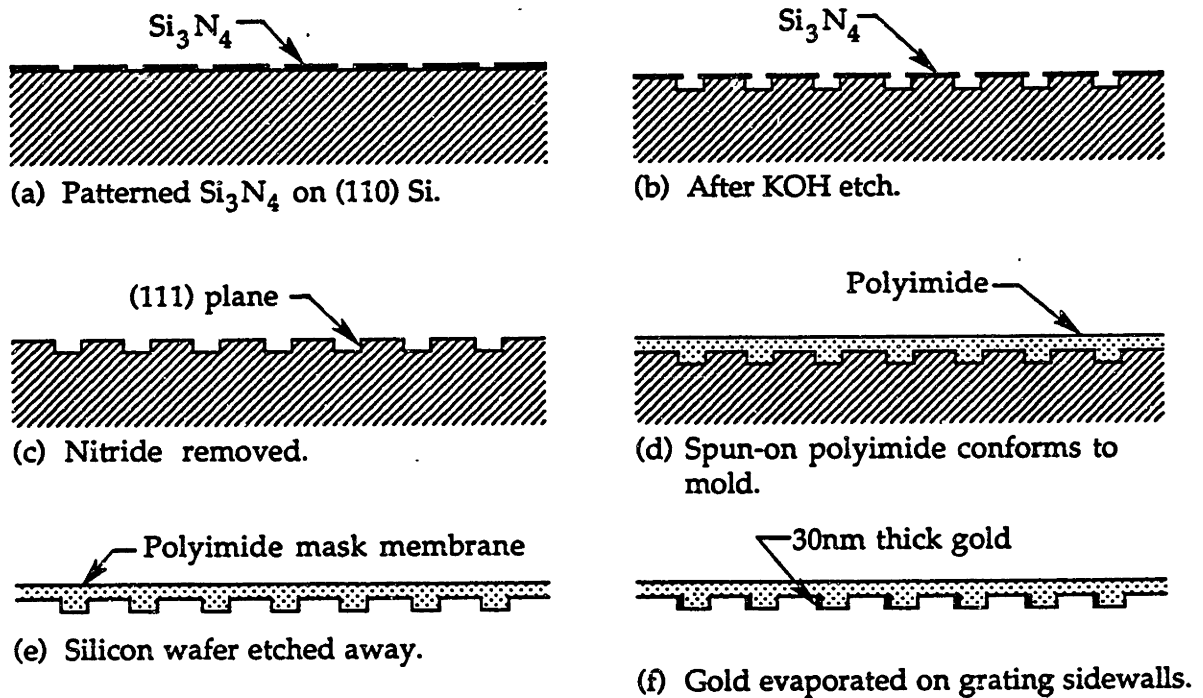


Figure B.1: Mask fabrication steps.

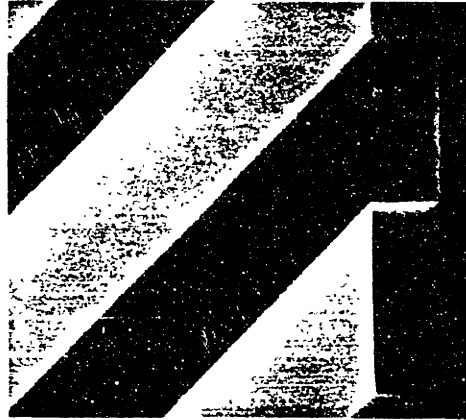
7. Dip the wafers in BOE for 15 seconds and rinse with DI.
8. Etch the wafers at 60°C in a solution consisting of 40% KOH and 60% DI which is then saturated with IPA. Dissolution of KOH pellets in DI is a highly exothermic reaction; the solution temperature will reach 90°C almost instantaneously and then gradually cool. For KOH mixing and etching wear an apron, face shield, and orange latex acid resistant gloves. Use a water bath to surround the KOH beaker and do not turn on the hotplate until the solution is completely mixed. Mixing of KOH pellets with heated DI will cause a violent reaction.  
  
The etch rate is typically ~ 120 nm/minute. Etch depth can be monitored with the Tencor profilometer. The etched silicon is shown schematically in Figure B.1 (b) and an SEM appears at the left in Figure B.2.
9. Strip the nitride in Transetch-N (phosphoric acid) heated to 180°C (Figure B.1 (c), also Figure B.2, center).
10. RCA clean the wafers (organic clean only).
11. Spin-on 1  $\mu\text{m}$  on Du Pont Pyralin LX PI-2610D polyimide. Softbake at 130°C for 30 minutes. Cure for one hour in the TRL polyimide furnace at 400°C (Figure B.1 (d)). If the mask is to be patterned on only one side skip steps 12 and 13.
12. Wafers are now ready for second level patterning. Plasma ash the polyimide for 6 seconds at 300 mTorr and 200 Watts in O<sub>2</sub>. Spin-on about 0.5  $\mu\text{m}$  of Shipley resist. Align second level mask, expose, and develop. If this is done in TRL with the Karl Suss aligner, hard contact should be used and the wafers should be slightly overexposed. The desired resist profile is vertical or, preferably, undercut. Evaporate 5 nm of chromium or NCr followed by 0.25  $\mu\text{m}$  gold at normal incidence.

**Figure B.2: Three stages in fabrication of polyimide mask making: At left, a (110), KOH etched wafer with masking nitride still in place. At center, the same sample after removal of the nitride. Note smoothness of the vertical sidewalls. At right, polyimide mask membrane made from silicon mold.**

# Anisotropic Etch of (110) Si and Mold of Polyimide Mask



Polyimide mask  
membrane made  
from silicon  
mold.



3.0 $\mu$ m

Etched grating  
after  $\text{Si}_3\text{N}_4$  has  
been removed.  
The grating  
sidewalls are  
perpendicular to  
the wafer surface.



Etched grating  
before removal of  
 $\text{Si}_3\text{N}_4$  mask. The  
grating sidewalls  
are the nearly  
atomically  
smooth  $\{111\}$  planes.

13. Lift-off of the resist is done using acetone in a 60 psi spray. This is done in the outer lab with the hood opening largely masked off with a plastic sheet. This prevents fumes and gold particulates from filling the lab. To facilitate lift-off, first soak the wafers in acetone. Once wafers are wet, do not allow acetone to dry until lift-off is complete. When using spray gun, the nozzle should be brought as close as possible to the wafer surface without touching it. If the nozzle touches the wafer surface the polyimide will be torn thus ruining the mask. When all the resist has been removed, rinse wafers with methanol, followed by DI, and blow dry.
14. Bond wafer to PVC pipe with black wax. This is done by painting one end of the PVC pipe with black wax and then pressing the wax coated surface against the polyimide coated wafer surface. The PVC pipe has two small holes drilled through diametrically opposing sides about a half inch from one end of the pipe. The *other* end of the pipe is the one to be coated with black wax. Allow the wafer/pipe bond to dry. Paint the wafer edges on both sides with wax; extend the wax up the side of the pipe about 3/8 of an inch. The idea is to create a water-tight seal so that the etchant cannot leak into the pipe. See Figure 14. Allow the wax to dry for a few hours.
15. Slide a 6" cotton-tipped applicator (Q-Tip) through the small holes in the pipe. This will provide a suspension bar for hanging the wafer in the etchant.
16. Assemble the etching apparatus and mix the etchant. Place a teflon runner in the sink. On this place a hotplate; this will be used for spinning only, no heating is used. Place a large glass dish for the DI bath on the hotplate. In this place a 1000 ml teflon beaker. As a safety precaution, keep the city water running in the sink. The set-up is illustrated in Figure B.4.
17. Before mixing etchant, don a plastic apron, face shield, arm shields, and orange latex acid resistant gloves. Pour 500 ml of 49% HF into the teflon

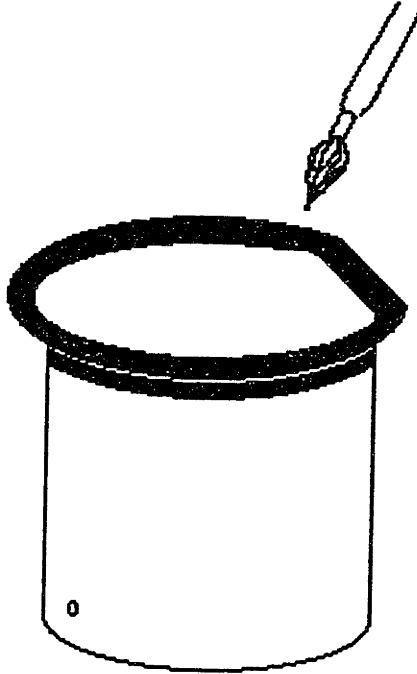


Figure B.3: PVC pipe with mask wafer: The membrane side faces the pipe. Black wax is painted to completely coat the edges of the wafer, extending about 1/4 inch in from the edge and about 3/8 inch up the side of the pipe. The wax creates a leak-tight seal that will prevent the etchant from entering the pipe.

beaker. To this add 15 ml of nitric acid; this is measured in a plastic graduated cylinder. Start magnetic spin bar.

18. When solution is well mixed, lower wafer/pipe assembly into beaker. The pipe will hang from the applicator stick. The wafer should just skim the etchant surface. If the wafer is submerged in the etchant carefully pour enough of the etchant out so that the just-skim-the-surface condition is met. Tilt the wafer/pipe assembly slightly to allow bubbles to escape as etching evolves. Place a wafer carrier cover over the top of the pipe to prevent fumes from filling the pipe. See Figure 18. The HF:nitric will eat through 300  $\mu\text{m}$  of silicon in about 10 minutes. A batch of etchant will be good for three wafers at most.

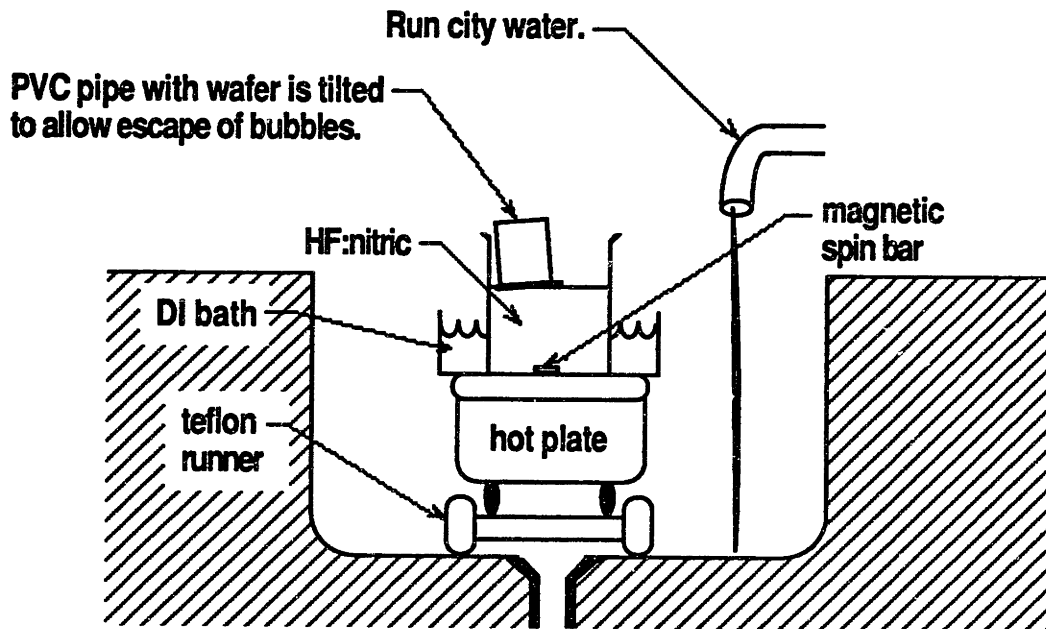
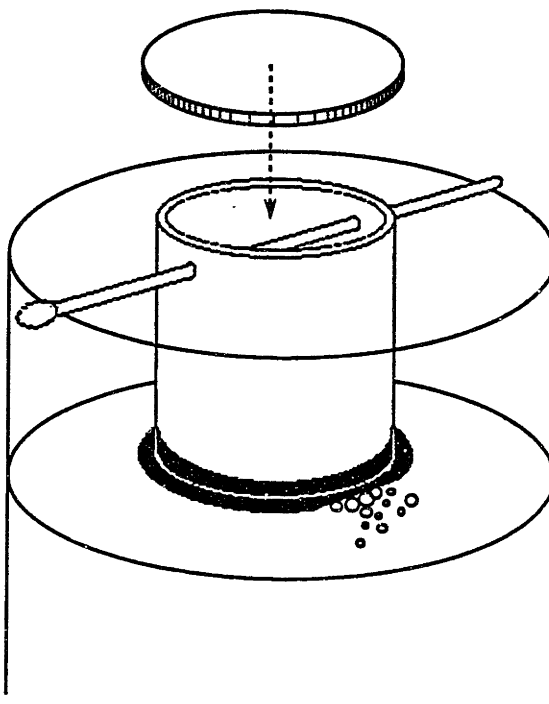


Figure B.4: Membrane etching is carried out under a well ventilated hood.

19. When etching is done, all of the wafer that was not protected by black wax will be gone, only the polyimide membrane will remain (Figure B.1 (e), also Figure B.2, right). Lift the pipe, hold it horizontally with the wafer vertical. Carefully rinse the membrane, the wafer and the portion of the pipe exposed to etchant with DI from a squirt bottle. Next rinse the membrane with IPA; this has a drying effect. Using very low pressure, blow-dry the membrane with nitrogen. Allow membranes to dry under the hood for a few hours, or, preferably, overnight.
20. Polyimide mask frames can be prepared at any point that is convenient. These are machined washers, made of polyimide, approximately  $3/32''$  thick, with the outer diameter beveled on one side. The beveled side will be bonded to the membrane. The bevel allows for easy removal of the mask from a wafer after exposure. The nonbeveled side can be inscribed with initials and





**Figure B.5:** The PVC pipe hangs over the etchant from a 6 inch cotton-tipped applicator. The wafer should just skim the surface of the etchant. The pipe is tilted slightly to allow bubbles to escape as etching evolves. A wafer carrier cover is place over the pipe to prevent fumes from filling the pipe.

some sort of mask identification using a diamond or carbide scribe. After inscribing, clean the frames with trichloroethane, followed by acetone, and then methanol. The frames come is three sizes: 0.5, 1.0, 1.25 inch diameters. If the mask is patterned on only one side, or if the gross pattern side does not provide continuous conductive paths across the membrane, skip step 21.

21. Because the finished mask will held in electrostatic contact during exposure, the mask frame must have a conductive film over it. This is accomplished by shadow evaporation of 30 nm of aluminum on the frames at a 45° angle. Use the special holders made to hold the mask rings. The nonbeveled side is the side that is to receive the aluminum. The best possible vacuum should be obtained, the chamber should be chromium-gettered before aluminum

evaporation, and the second shutter on the evaporator should be used.

Note that the membrane must also have a conductive film on the back side to act as one plate of a parallel plate capacitor. For Gee Rittenhouse's device mask, the second level patterning on the back side of the mask creates a gold grid structure which serves also as the conducting film. If no second level pattern is used, or if the second level pattern is discontinuous, the mask frame should be bonded to the membrane before aluminum deposition. The 30 nm of aluminum is then deposited simultaneously on the back of the membrane and on the mask frame.

22. The mask frames can now be bonded to the membranes. During this process, each mask frame is lightly held to a glass bottle which is used simply to facilitate bonding. The glass bottle is epoxy-bonded to a glass slide. Invert the bottle so that it is sitting on the glass slide. Place four small strips of double-sided masking tape equally spaced about the diameter of the bottle bottom. Place a mask frame, beveled side up, on the bottle bottom so that it is held by the tape. Use the noncotton end of a Q-Tip, coat the exposed mask frame surface with a thin layer of Bipax Tra-Duct BA-2915 epoxy.
23. Set the pipe with etched membrane, membrane side down, in an individual teflon wafer carrier. Invert the bottle with the mask frame and lower it into the pipe until the mask frame is sitting on the membrane which will stretch slightly under its weight. This is most easily accomplished with the aid of a mechanical third hand. The third hand has a rack and pinion that allows easy lowering of the frame. See Figure B.6. Allow the epoxy to cure for a minimum of 24 hours, 48 hours is better.
24. After the epoxy has cured, hold the bottle in one hand and the pipe in the other. Invert the assembly. The mask can now be cut away from the wafer using a single edged razor blade. After trimming the outer edges, gently

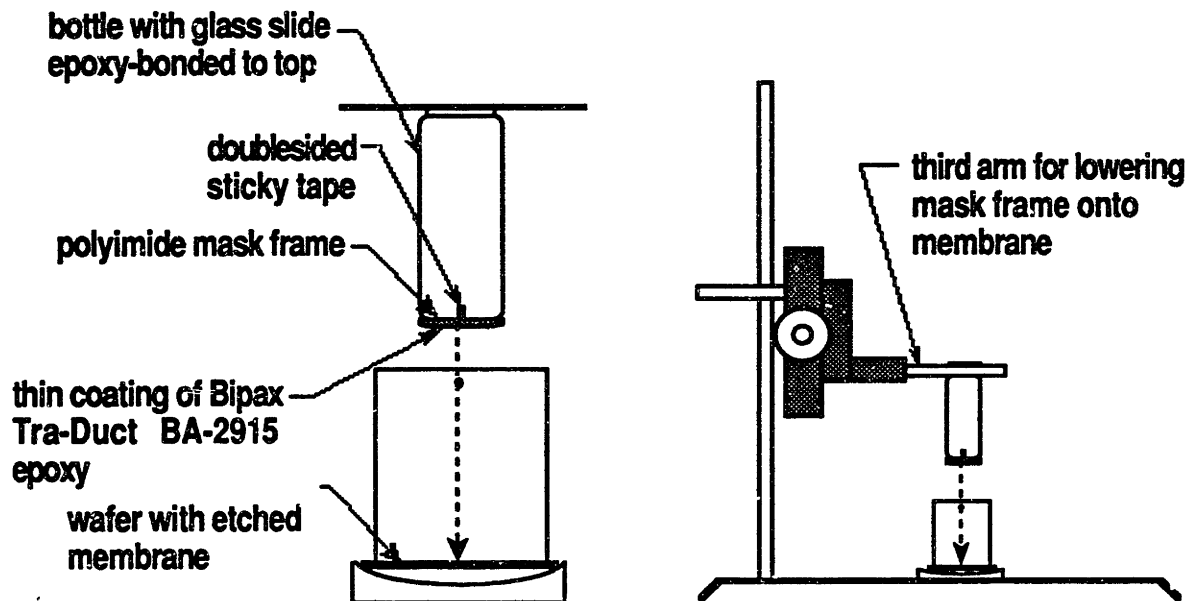


Figure B.6: Mask-frame-to-membrane bonding: The pipe is place wafer side down in a teflon wafer carrier. The epoxy-coated mask frame is lightly held to the bottle/slide assembly by double sided masking tape. A third arm is used to carefully lower the frame onto the membrane. The bottle serves as a weight to press the frame against the membrane while the epoxy cures.

remove the mask from the bottle. Store in a wafer carrier. If the mask was patterned on both sides, skip step 25.

25. Because the finished mask will held in electrostatic contact during exposure, the back side of the mask must have a conductive film over it. This is accomplished by shadow evaporation of 30 nm of aluminum on the mask at a 45° angle. Use the special holders made to hold the mask rings. The grating side of the mask faces away from the evaporation source. The best possible vacuum should be obtained, the chamber should be chromium-gettered before aluminum evaporation, and the second shutter on the evaporator should be used.

26. The penultimate step is shadow evaporation of gold on the grating sidewall (Figure B.1 (f)). Load the mask in the 45° mask holder, grating side up. Orient the mask so that the grating is parallel to the plate or counter on which the mask holder sits. The grating lines must be normal to the direction of evaporation for this step to work. Use the fiber light as an aid. Diffraction from the grating must be parallel to the direction of evaporation (i.e. normal to the floor). Mount the mask holder to the evaporator angle plate. Adjust to the calculated steep angle for the grating used (usually between 5° and 10°). Evaporate 5 nm of chromium, or NiCr, for adhesion, then evaporate the desired thickness of gold.
27. Electrical connection must now be made between the mask membrane and the mask frame. Mix some Bipax Tra-Con BA-2902 silver epoxy. Break a Q-Tip, and using the broken end, connect the mask frame inner diameter to the gold (or aluminum) coated membrane back surface with a thin string of epoxy. Be careful not to puncture the membrane. Try to keep the epoxy area on the membrane to a bare minimum as it causes distortion and weakens the mask locally. A TEM grid can be epoxied to the outer diameter of the mask frame so that it overhangs the outer diameter. The TEM grid is useful for determining whether the x-ray source was properly focused during exposure. If desired, a mask handle can be fabricated from a slender strip of thin brass that is bent to an appropriate shape and epoxy-bonded to the mask frame. Allow the epoxy to cure overnight. The mask is now ready to use.

# Appendix C

## KOH Etching

Anisotropic etching with potassium hydroxide (KOH) is widely exploited in the semiconductor industry and in research. Work done as part of this thesis required KOH etching of both (100) and (110) silicon. For diffraction exposures, a gap of the desired depth was obtained by etching a 3/4 inch diameter pit in the center of a three inch (100) wafer. In the photoelectron range experiment, the polyimide mask was fabricated using an anisotropically etched, 2 inch diameter, (110) wafer as a mold.

In addition, masks were built and work was done to obtain sub-0.1  $\mu\text{m}$ -thick vertical walls of silicon in (110) material for resonant tunneling devices for Gee Rittenhouse's thesis [91,92]. As part of this work, a novel etched geometry was designed that produced a sub-10 nm-thick vertical membrane. This membrane is most probably the thinnest ever fabricated from single crystal silicon.

Finally, an electrochemically etched membrane,  $\sim 1 \mu\text{m}$ -thick and 3/4 inch in diameter was fabricated from a (100) wafer. This membrane was ultimately not useful for x-ray lithography, but its fabrication added to our store of knowledge on KOH etching, and details of its fabrication are included for that reason.

In all these etching applications a common requirement was minimizing roughness of the silicon planes uncovered by the etch. The etch rates for the three

crystallographic orientations differ from each other markedly. The most rapidly etching is {110}, followed by {100}; {111} etches almost imperceptibly. Rate ratios as high as 200:400:1 have been measured for {100}:{110}:{111} [93,94]. Etch rates for a single orientation vary with temperature, KOH concentration, and with the addition of isopropyl alcohol (IPA).

The etch results described in this appendix were essentially determined by initial conditions and boundary conditions. The boundary condition was always the interaction between the etchant and the silicon; the initial conditions were the quality of the silicon surface prior to etching and, for some problems, the exactness of alignment of the masking material to the desired crystallographic plane.

## C.1 Etching of (100) Silicon

In (100) silicon, both for the etched pits and for the electrochemically etched membrane, the exposed orientation of interest at the termination of the etch was (100). The etch was merely to remove layer after layer of (100) silicon while keeping the uncovered surface as smooth as possible.

The initial condition, the starting surface, is critical; a smooth etched (100) surface is only obtained only by beginning the etch from a smooth surface. An unpolished nominal (100) surface may typically have surface roughness of the order of 10  $\mu\text{m}$ . As it etches, macroscopic lateral surface texture changes, but the the peak-to-valley surface roughness remains constant. The next section explores the ability of an electrochemical etch stop to smooth out surface roughness.

### C.1.1 Electrochemical Etch Stop Experiment

In an electrochemical etch stop, a wafer with a reverse biased  $pn$  junction is placed in the etchant (KOH) and biased such that the  $n$ -type material is held at a potential positive of the oxide forming potential (OFP); the  $p$ -type material is floated, or

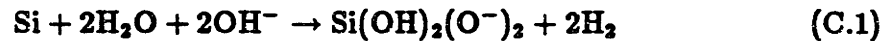
biased, at the open circuit potential (OCP) [95,96]. (A full description of the electrical circuit and current monitoring can be found in the cited references. Here I am presenting information on membrane surface quality that cannot be found in the references.) The wafer is protected everywhere by either oxide or nitride except in the membrane area. The exposed *p*-type material is etched away to expose the positively biased *n*-type membrane which oxidizes thus terminating the etch. It is the thickness of the *n*-type layer that determines the membrane thickness.

In the case of an etch that begins on unpolished silicon, the local peak-to-valley maximum surface roughness of the *p*-type material can be as much as 10  $\mu\text{m}$  just prior to passivation. The emergence of the underlying *n*-type material will not be uniform. The extreme peaks in the *p*-type silicon will take significant time to etch away. Meanwhile, the oxide on the passivated surface is slowly etching away (3.6 nm/minute for 40% KOH at 60°C [95]). This corresponds to a slow consumption of *n*-type material. When the *p*-type peaks completely etch away, the overall *n*-type passivated surface will be uneven even though the roughness will be significantly reduced from the peak just prior to passivation. Additional roughness can result from leakage currents that can force the potential of the *p*-type silicon immediately adjacent to the junction to a voltage positive of the OFP thus causing it to passivate prematurely.

By applying a bias to the *p*-type region to prevent premature passivation, Kloek et al. [95] have etched 10  $\mu\text{m}$ -thick square membranes, 2mm on a side, from unpolished silicon to a final surface roughness of  $\sim \pm 0.1 \mu\text{m}$ . But for an x-ray membrane even this degree of roughness is prohibitive. The only way to obtain an etch stop surface with smoothness approaching that of polished silicon is to begin with a smooth surface and have all the *p*-type surface etch through at approximately the same time.

While a smooth starting surface is a necessary condition, it is not a sufficient

condition to insure a smooth terminating surface. The etch rate is also crucial. A high etch rate leads to a rough etched surface. The equation describing the chemical reaction at the surface is believed to be [93,97]:



As can be seen from the right side of Equation C.1, hydrogen gas is a byproduct of the reaction. As hydrogen evolves, bubbles appear on the surface of the etching silicon. The higher the etch rate, the more rapidly hydrogen is produced. This leads to the formation of comparatively large size bubbles that cling to the silicon surface. For low etch rates the bubbles that form are small; they leave the wafer surface almost as soon as formed. Surface roughening appears to be caused by a difference in etch rate between the silicon underneath and outside the bubbles; the longer the bubbles cling the rougher the surface.

KOH etch rate drops with increase in KOH concentration and with decrease in temperature. Etch rate, and surface roughness, is maximized at  $\sim 1.5 \mu\text{m}/\text{minute}$  for 22:78 KOH:DI at  $80^\circ\text{C}$ . A comparatively smooth surface is obtained for 40:60 KOH:DI at  $60^\circ\text{C}$  with the etch rate dropping to  $\sim 0.12 \mu\text{m}$ .

Figure C.1 illustrates the effect of KOH etching under various conditions. Figure C.1 (a) and (b) are  $200 \mu\text{m}$ -deep pits etched in the same (100) wafer, one is etched from the smooth front surface, the other from the rough back surface. The back surface texture appears to be made of hills with polygonal boundaries; actually, they are valleys, some as deep as  $8 \mu\text{m}$ , with maximum lateral dimensions of  $\sim 500 \mu\text{m}$ . The surface etched from polished silicon has surface roughness of  $\pm 0.1 \mu\text{m}$ . Figure C.1 (c) is an optical micrograph of a  $80 \mu\text{m}$ -deep pit etched in polished silicon using a KOH solution saturated with IPA. The addition of IPA, for (100) etches, does not increase the smoothness of the etched surface; rather, it etches so as to expose the intersection of (111) and (110) planes with the surface. Why this happens is not understood.



Figure C.2 (a) shows the electrochemically etched membrane imaged in a Fizeau interferometer. This membrane was made from a double-side polished, *p*-type, (100) wafer; the *pn*-junction was formed by phosphorus diffusion to a depth of  $\sim 1 \mu\text{m}$ . Note the two sets of fringes. The parabolic fringes are due to stress, caused in part by the 100 nm-thick nitride which still coats the front side of the membrane. The roughly round set of fringes is due to nonuniformity in membrane thickness. This nonuniformity may be due to gouging of the silicon during the reactive ion etching of the masking nitride. The black spot near the wafer flat is where the electrode was bonded to the *n*-type material. Stacking faults are visible as crosses in the membrane area; other imperfections in the membrane surface appear as snakelike lines at an angle to the stacking faults. These lines correspond to areas where bubbles were seen clinging to the wafer surface during etching. Presumably some imperfection of the original silicon surface caused the bubbles to nucleate. Figure C.2 (c) and (d) are micrographs of a portion of the membrane that contained these defects. View (c) was taken midway through membrane passivation and (d) was taken after completion of passivation. Stacking faults appeared first in the bubble areas. The conclusion is that, since these areas passivated first, the areas beneath the bubbles etched more rapidly than the surrounding silicon. Figure C.2 (b) is a Linnik interferogram of the etched membrane surface showing that, aside from stacking faults, the membrane surface is smooth.

This experiment illustrates the unsuitability of electrochemical etch stop for fabrication of x-ray membranes. The membrane thickness uniformity could be improved by replacing the nitride RIE step with a wet etch. The stacking faults might be eliminated by using a more lightly doped junction, preferably epitaxially grown. Three major drawbacks remain: (1) the sensitivity of the final surface to the starting surface; (2) the requirement of a low etch rate and hence a long etch time to obtain a smooth surface; and (3) the difficulties inherent in electrically

contacting and etching batches of wafers.

### **C.1.2 Etch Pits for Diffraction Experiment**

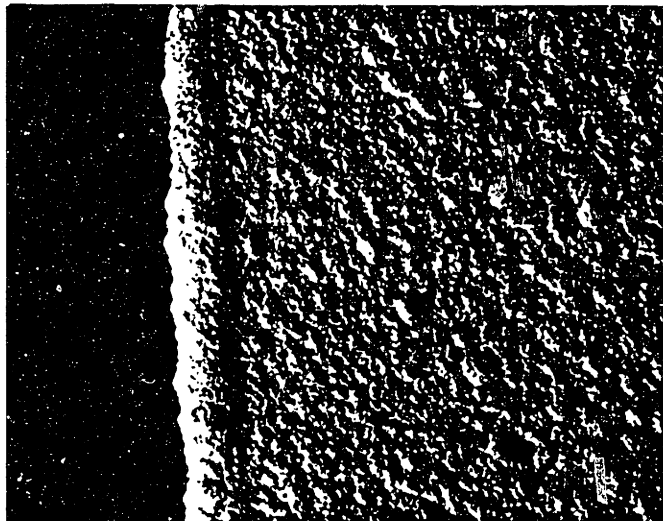
The etched pits for the diffraction experiment were fabricated as follows:

1. Thermal SiO<sub>2</sub>, 1 μm-thick, was grown on 3 inch diameter wafers.
2. These were then resist coated and the resist was patterned to expose a 3/4 inch diameter hole at the wafer center.
3. The wafers were soaked in BOE for 7 minutes to pattern the oxide.
4. The resist was stripped with acetone, rinsed with methanol, and then cleaned in an O<sub>2</sub> plasma for 30 seconds.
5. Immediately prior to KOH etching, each wafer was again dipped in BOE for 15 seconds and rinsed with DI. The purpose of this etch was to remove the oxide that formed in the plasma asher. KOH etches oxide slowly. Without the BOE rinse, any nonuniformity in the native oxide on the wafer surface would be magnified in the etched silicon surface.
6. The wafers were etched in 40%, by weight, KOH and 60% DI at 60°C. The etch rate and depth were monitored using the Tencor surface profilometer.
7. Once the desired depth plus 1 μm was reached, the masking oxide was removed by again soaking them in BOE for 7 minutes.
8. After RCA cleaning the wafers are ready for resist processing.

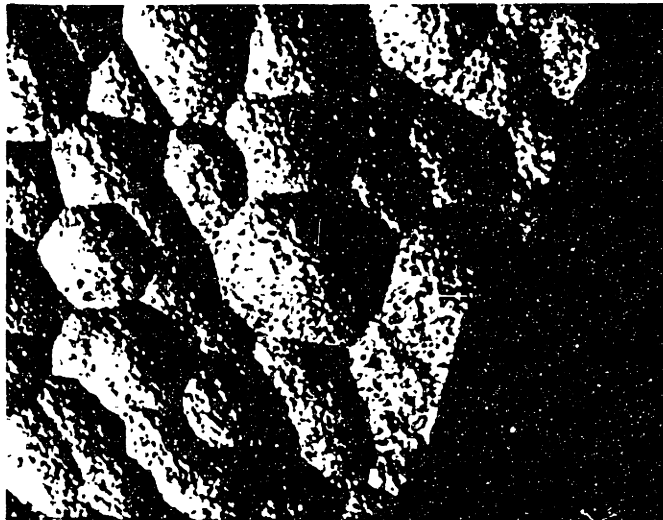
As can be seen from Figure C.3 (a), the etched pit, in this case 20 μm-deep, is essentially parallel to the wafer surface and is flat to within a fringe or two. The interferogram of the silicon surface in the pit shown in Figure C.3 (b) was taken with a Linnik interferometer. The fringes are undistorted confirming the

**essential smoothness of the surface; a very slight roughening, 100 nm. at most, can be detected in the noisiness of the fringes.**

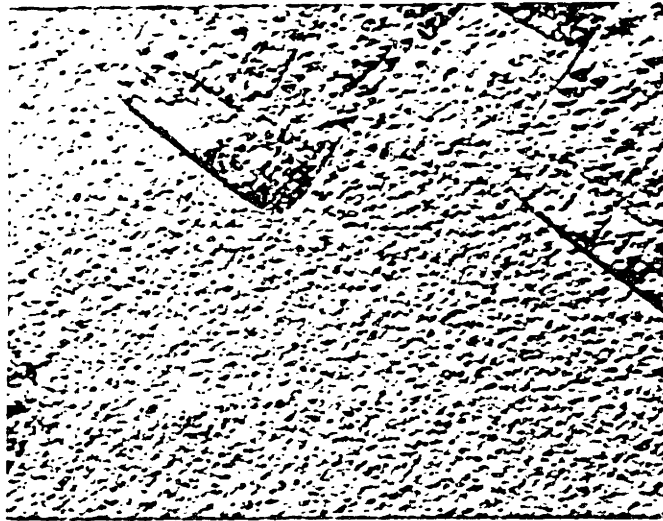
**Figure C.1: (100) Silicon etched in 40% KOH, 60% DI at 60°: (a) was etched from the front and (b) from the back surface of the same wafer; (c) was etched from the front of the wafer with the addition of IPA to saturate the solution.**



(a)

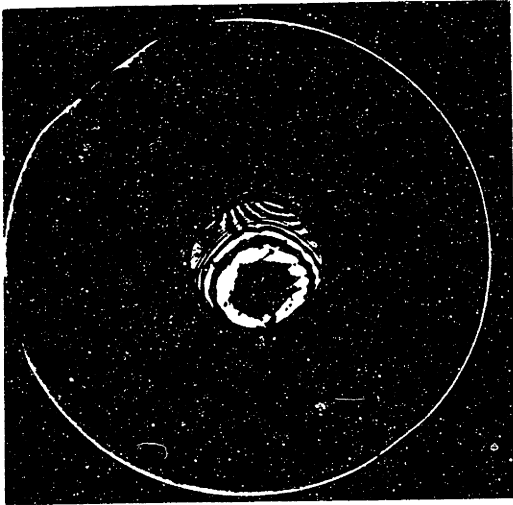


(b)

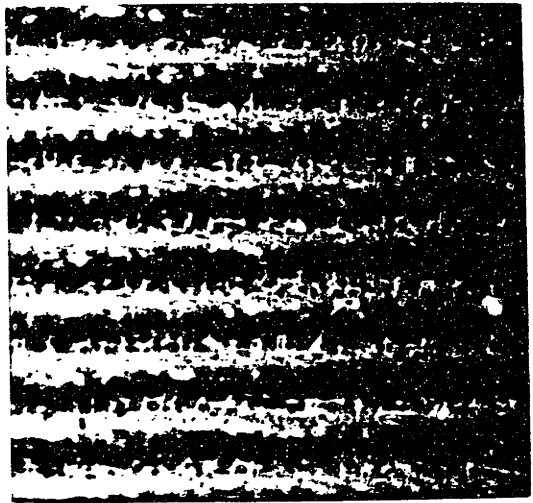


(c)

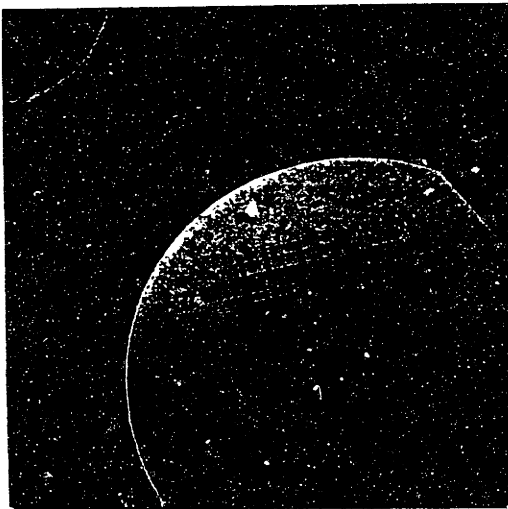
**Figure C.2: An electrochemically etched membrane fabricated from a double side polished wafer: (a) a Fizeau interferogram of the membrane; (b) a Linnik interferogram of the etched membrane; (c) the membrane has begun to passivate first in the bubble areas; (d) the membrane is completely passivated.**



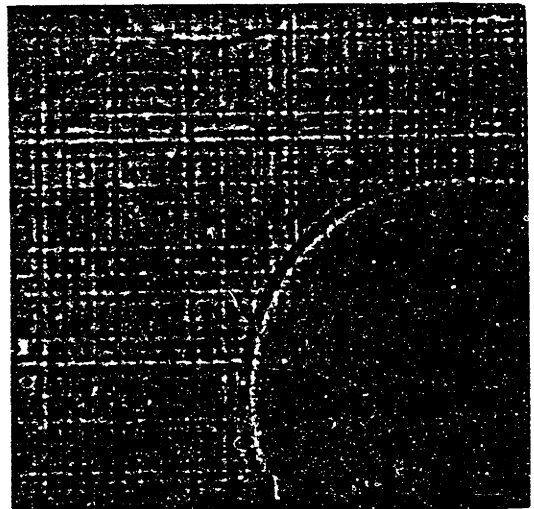
(a)



(b)



(c)

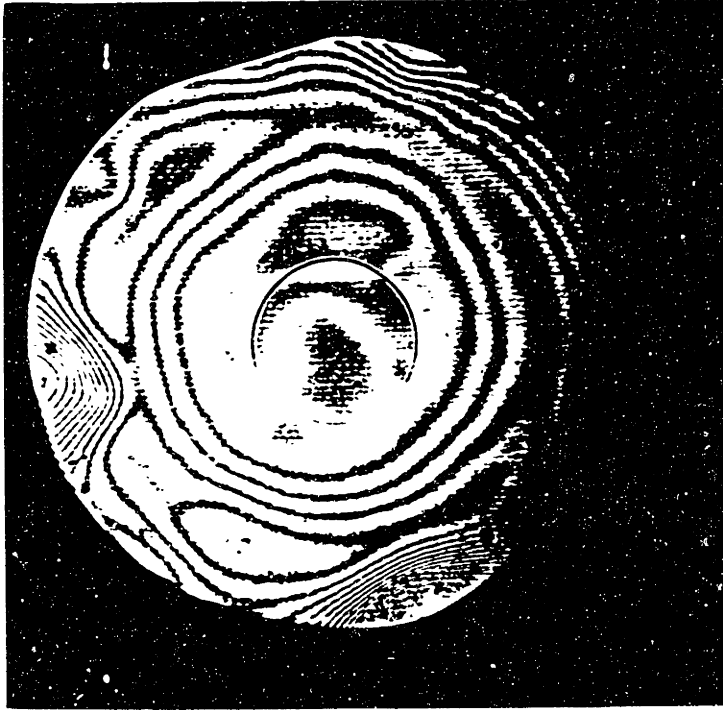


(d)

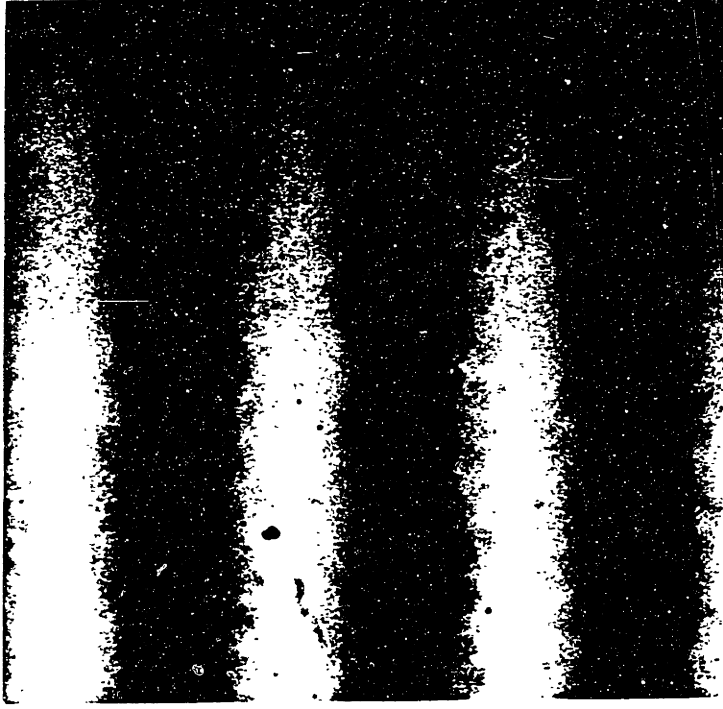
**Figure C.3: (a) A Fizeau interferogram of a 20  $\mu\text{m}$ -deep pit etched in a 4-inch (100) wafer; most of the pit lies within a single fringe. (b) A Linnik interferogram indicates that the etched surface is smooth to within 100nm.**



# 20 $\mu$ m-Deep Etched Pit



(a)



(b)

## C.2 Anisotropic Etching of (110) Silicon

In etching (110) silicon, one is interested in exposing the perpendicular (111) planes. Therefore precise alignment of the masking material to the intersection of these planes with the wafer surface is desirable. In addition, the uncovered (110) surface must be kept as smooth and flat as possible.

Typically,  $\text{Si}_3\text{N}_4$  is used as the masking material. When patterning the nitride in the reactive ion etcher (using  $\text{CF}_4$  or  $\text{CHF}_3$ ) it is important to avoid overetching. Fringing fields will cause the silicon immediately adjacent to the nitride to etch faster than elsewhere. The resulting gouging of the silicon is not removed in the KOH etch step.

As with (100) silicon, the best etch solution has been found to be 40% KOH and 60% DI to which IPA is added to saturate; a layer of 0.5 inch of IPA floating on the surface is usually sufficient to insure that the IPA does not all evaporate during the etch. The etch is carried out at 60°C. With IPA added to the etchant, adequate smoothness and flatness can be obtained using lower KOH concentrations and higher temperatures; but usually one is not interested in etching much deeper than a micron. The slower etch rate allows for more control over the precision of etch depth. In addition, selectivity of the various crystallographic planes increases with increasing KOH concentration. The higher concentration insures verticality of the exposed (111) planes.

Because (111) silicon etches extraordinarily slowly in KOH, the smoothness of these planes is largely unaffected by the etch concentration and temperature. However, failure to correctly align the mask to the (111) plane will cause jogs along the surface as illustrated in Figure C.4. For the mask in the photoelectron experiment this was not a problem because it only effected the straightness of the line, not it's ultimate width which was determined by the gold evaporated on the mask.

If the goal is a quantum effect device with a sub- $0.1\mu\text{m}$ -thick,  $0.6\mu\text{m}$ -high, and  $250\mu\text{m}$ -long wall, accurate alignment is imperative. Without near perfect alignment the wall will be destroyed as the etchant attacks the jogs in the wall surface. Not only must the mask to device wafer alignment be perfect, but, the mask lines must be straight for at least the  $250\mu\text{m}$  gate width. Using the procedure outlined in Appendix B, masks were built for such a device. With difficulty, the mask-to-substrate alignment was accomplished.

The trick used was to align striations on the mask, caused by the KOH etching of the mold wafer, with striations in an alignment pit etched in the center of the device wafer. The striations, examples of which can be seen in Figure B.2, lie at  $54.7^\circ$  from the vertical (111) planes and thus provide an accurate reference. The difficulty with the alignment is that the striation are faint, the mask and substrate striations lie in two different planes, and the plastic polyimide mask membrane is prone to in-plane distortion. In spite of these problem, the mask can be aligned, repeatedly, so that devices are obtained over at least some portion of the mask area. One such device is shown in Figure C.6.

If the single long wall of silicon is replaced by a number of small triangular walls, the requirement of perfect alignment can be relaxed. This is done by utilizing the two sets of (111) planes which lie at  $\pm 35.3^\circ$  from the (110) surface as etch barriers. Figure C.5 schematically illustrates this novel geometry. If the fine line is not perfectly aligned to the crystallographic plane any jogs in the wall will continue to etch until they reach a sloped (111) surface at which point the etch effectively terminates.

To demonstrate this concept, a (110) wafer was masked with a  $4\mu\text{m}$ -period, 50% duty-cycle grating aligned to the (111) planes that lie at  $\pm 35.3^\circ$  to the (110) surface and with 30nm-wide lines, spaced  $4\mu\text{m}$  apart, aligned to one set of perpendicular (111) planes. Parallelograms, formed by the intersection of these two gratings, were then opened in the  $\text{Si}_3\text{N}_4$ . The wafer was etched in KOH and the nitride was

stripped in Transetch-N (phosphoric acid) at 180°. Figure C.7 is an SEM of one of the resulting triangular membranes. The membrane is thinner than 10nm and presumably has near-atomically smooth surfaces. The wafer was left in the KOH solution for one hour, far longer than the ~ 5 minutes required to fully expose the (111) terminating surfaces.

This technique, of using the nonperpendicular (111) planes as etch barriers, is completely general and can be used in any situation in which a single silicon wall can be replaced by a number of smaller walls.

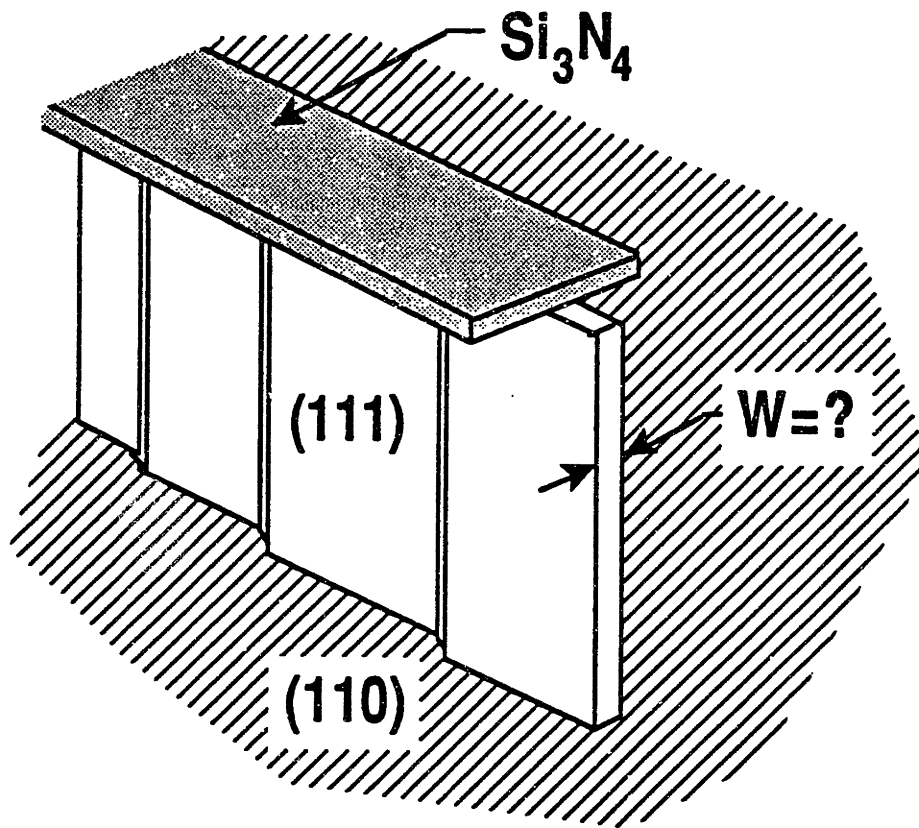


Figure C.4: Misalignment to the crystallographic plane causes jogs in the (111) wall.

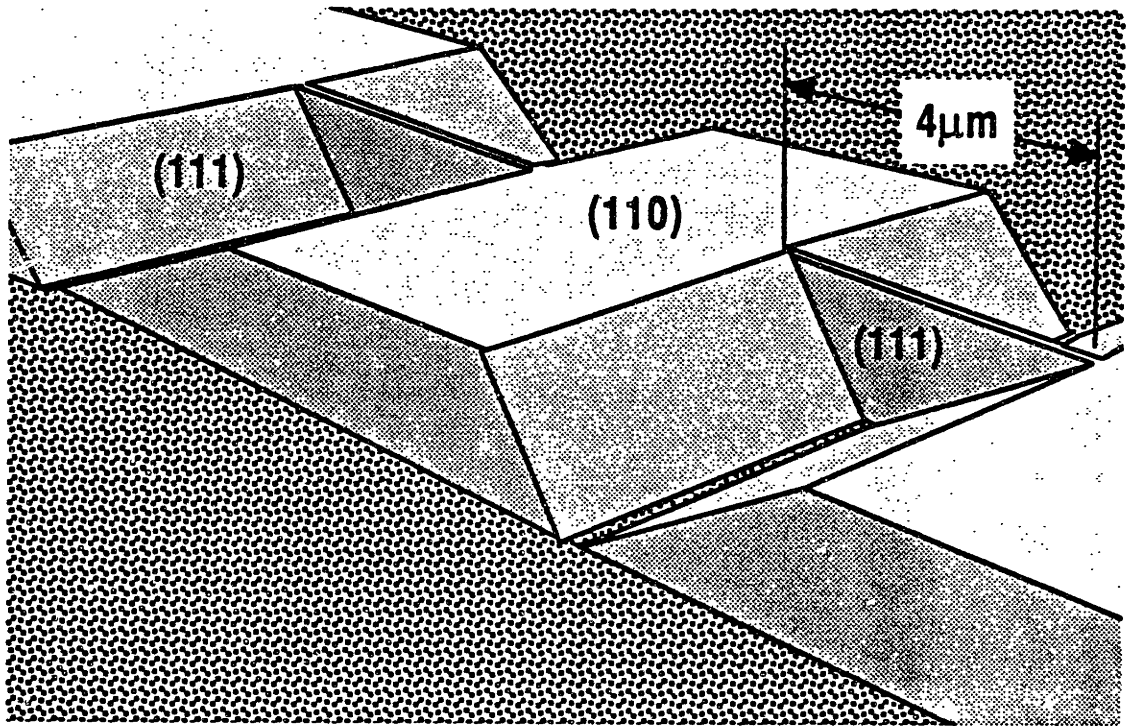
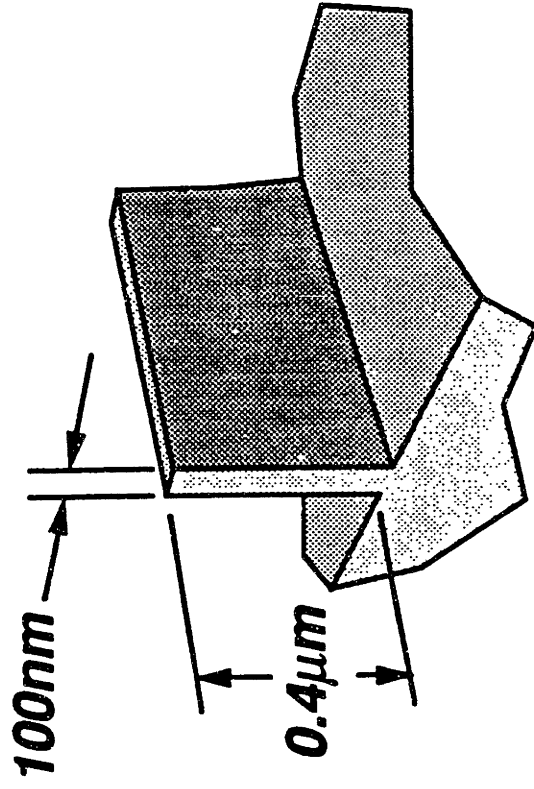
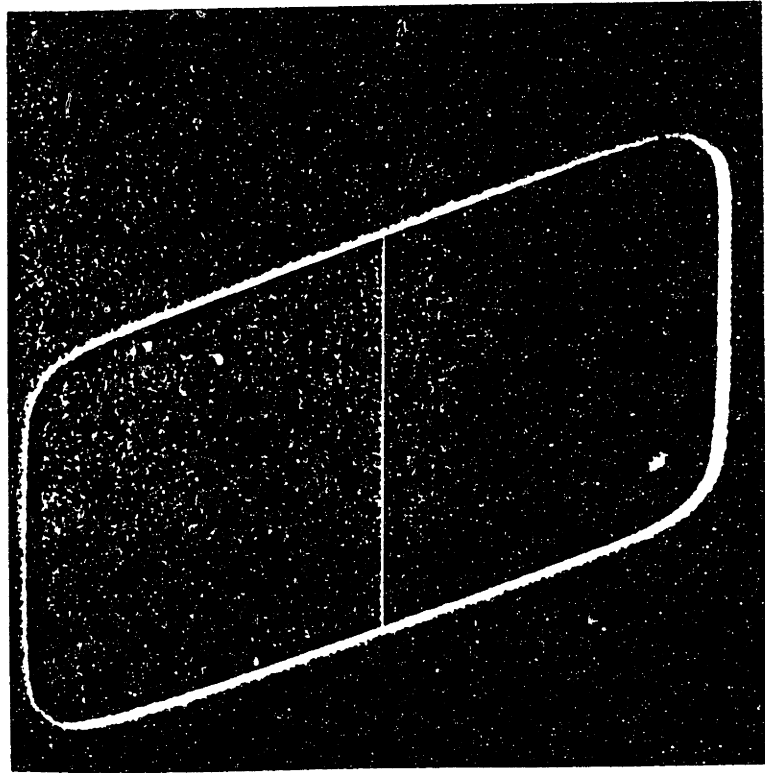


Figure C.5: Schematic illustration of triangular walls, or membranes, that can be formed by utilizing the nonperpendicular (111) planes as etch barriers.

**Figure C.6: First level patterning of a resonant tunneling device [91,92]. The “gate” of the device is a wall of silicon defined by vertical (111) planes.**

# RT Device in Anisotropically Etched (110) Silicon





**Figure C.7: A triangular membrane, thinner than 10 nm, that was etched in (110) silicon. The etch has terminated everywhere on {111} planes.**

# KOH Etched Silicon Nanostructure



1.5 $\mu$ m

- *Membrane thickness < 10nm*
- *Etch terminates on  $\{111\}$  surfaces.*

# Bibliography

- [1] W. Shockley, "How we invented the transistor," *New Scientist*, vol. 21, p. 689, Dec 1972.
- [2] R. M. Warner Jr. and B. L. Grung, *Transistors: Fundamentals for the integrated-circuit engineer*, ch. 1, pp. 1–91. Wiley-Interscience, 1983.
- [3] W. Arden and K. Müller, "Light vs x-rays: How fine can we get?," *Semiconductor International*, vol. , pp. 12–15, Sep 1989.
- [4] B. J. Lin, "Partially coherent imaging in two dimensions and the theoretical limits of projection printing in microfabrication," *IEEE Transactions on Electron Devices*, vol. ED-27, pp. 931–938, May 1980.
- [5] D. L. Spears and H. I. Smith, "High-resolution pattern replication using soft x rays," *Electronics Letters*, vol. 8, pp. 102–104, Feb 1972.
- [6] K. Early, M. L. Schattenburg, and H. I. Smith, "Absence of resolution degradation in x-ray lithography for  $\lambda$  from 4.5nm to 0.83nm," *Microelectronic Engineering*, vol. 11, pp. 317–321, Nov 1989.
- [7] A. Yen, R. A. Ghanbari, Y. Ku, W. Chu, M. L. Schattenburg, J. M. Carter, and H. I. Smith, "X-ray masks with large-area 100nm-period gratings for quantum-effect device applications," . To be published in *Microelectronic Engineering* as part of the Proceedings of the International Conference on Microlithography, *Microcircuit Engineering 90*, Leuven, Belgium, 18-20 September 1990.
- [8] D. C. Flanders, "Replication of 175-Å lines and spaces in polymethylmethacrylate using x-ray lithography," *Appl. Phys. Lett.*, vol. 36, pp. 93–96, Jan 1980.
- [9] S. Wittekoek, M. von den Brink, H. Linder, J. Stoeldrayer, J. W. D. Martens, and D. Ritchie, "Deep UV wafer stepper with through the lens wafer to reticle alignment," in *Optical/Laser Microlithography III*, (V. Pol, ed.), pp. 534–547, 1990.

- [10] S. G. Olson and C. Sparkes, "Advances in deep UV lithography," in *Optical/Laser Microlithography III*, (V. Pol, ed.), pp. 486–493, 1990.
- [11] J. W. Thackeray, J. F. Bohland, E. K. Pavelchek, G. W. Orsula, and A. W. McCullough, "Silylated acid hardened resist [SAHR] technology: positive, dry developable deep UV resists," in *Dry Processing for Submicrometer Lithography*, (J. Bondur and A. R. Reinberg, eds.), pp. 2–11, 1990.
- [12] M. Op de Beeck, N. Samarakone, K. H. Baik, L. Van den hove, and D. Ritchie, "Sub-half micron deep UV lithography using wet and dry developable resist schemes," in *Advances in Resist Technology and Processing VII*, pp. 139–150, 1990.
- [13] H. Fukuda, A. Imai, T. Terasawa, and S. Okazaki, "New approach to resolution limit and advanced image formation techniques in optical lithography," *IEEE Transactions on Electron Devices*, vol. 38, pp. 67–75, Jan 1991.
- [14] R. Brandt, J. B. Levine, R. D. Hof, J. Carey, and O. Port, "The future of silicon valley," *Business Week*, vol. , pp. 54–60, Feb 1990.
- [15] A. D. Wilson, "X-ray lithography into the 1990s," Invited talk, International Conference on Microlithography, Microcircuits Engineering 89, 26-28 Sept 1989, Cambridge, England.
- [16] A. Yoshikawa, T. Horiuchi, K. Deguchi, M. Mikake, E. Yamamoto, Y. Sakakibara, and T. Kitayama, "Synchrotron radiation lithography applied to fabrication of deep-submicrometer NMOS devices at all exposure levels," *Microelectronic Engineering*, vol. 11, pp. 233–236, Nov 1989.
- [17] A. M. Hawryluk and L. G. Seppala, "Soft x-ray projection lithography using an x-ray reduction camera," *J. Vac. Sci. Technol. B*, vol. 6, pp. 2162–2166, Nov/Dec 1988.
- [18] N. M. Ceglio, A. M. Hawryluk, D. G. Stearns, D. P. Gaines, and R. S. Rosen, "Soft x-ray projection lithography," *J. Vac. Sci. Technol. B*, vol. 8, pp. 1325–1328, Nov/Dec 1990.
- [19] J. E. Bjorkholm, J. Boker, L. Eichner, R. R. Freeman, J. Gregus, T. E. Jewell, W. M. Mansfield, A. A. MacDowell, E. L. Raab, W. T. Silfvast, L. H. Szeto, D. M. Tennant, W. K. Waskiewicz, D. L. White, D. L. Windt, O. R. Wood II, and J. H. Bruning, "Reduction imaging at 140nm using multilayer-coated optics: printing features smaller than 0.1 $\mu$ m," *J. Vac. Sci. Technol. B*, vol. 8, pp. 1509–1513, Nov/Dec 1990.
- [20] T. E. Jewell, "Reflective systems design study for soft x-ray projection lithography," *J. Vac. Sci. Technol. B*, vol. 8, pp. 1519–1523, Nov/Dec 1990.

- [21] R. E. Burge, M. T. Browne, and P. Charalambous, "An x-ray projection method using zone plates for mask preparation with sub-micron sizes," *Microelectronic Engineering*, vol. 6, pp. 227–232, 1987.
- [22] A. G. Michette, *Optical Systems for Soft X Rays*, ch. 1, pp. 7–27. Plenum Press, 1986.
- [23] M. L. Schattenburg, K. Early, Y. Ku, M. I. Shepard, S. The, and H. I. Smith, "Fabrication and testing of 0.1 $\mu$ m-linewidth x-ray masks," *Journal of Vacuum Science and Technology B*, vol. 8, pp. 1604–1608, Nov/Dec 1990.
- [24] D. L. Spears, H. I. Smith, and E. Stern, "X-ray replication of scanning electron microscope generated patterns," in *Proceedings of the Fifth International Conference on Electron and Ion Beam Science and Technology*, (E. S. Inc., ed.), 1972.
- [25] R. Feder, E. Spiller, and J. Topalian, "Replication of 0.1 $\mu$ m geometries with x-ray lithography," *Journal of Vacuum Science and Technology*, vol. 12, pp. 1332–1334, Nov/Dec 1975.
- [26] H. K. O. and Manfred Weiss, R. Dammel, and J. Theis, "Percolation theory and resist development in x-ray lithography," *Microcircuits Engineering*, vol. 11, pp. 267–270, 1989.
- [27] M. L. Schattenburg, I. Tanaka, and H. I. Smith, "Microgap x-ray nanolithography," *Microelectronic Engineering*, vol. 6, pp. 273–279, 1987.
- [28] S. A. Rishton, S. P. Beaumont, and C. D. W. Wilkenson, "Exposure range of low energy electrons in PMMA," in *Proc. 10th Int. Conf. Electron Ion Beam Sci. Technol.*, (E. S. Inc., ed.), 1983.
- [29] K. Deguchi, H. Namatsu, K. Komatsu, and A. Yoshikawa, "Effects of photoelectrons ejected from the substrate on patterning characteristics in x-ray lithography," *Journal of Vacuum Science and Technology*, vol. B5, pp. 551–554, Mar/Apr 1987.
- [30] T. E. Everhart and P. H. Hoff, "Determination of kilovolt electron energy dissipation vs penetration distance in solid materials," *Journal of Applied Physics*, vol. 42, pp. 5837–5846, Dec 1971.
- [31] K. Murata, M. Kotera, K. Nagami, and S. Namba, "Monte carlo modeling of the photo and auger electron production in x-ray lithography with synchrotron radiation," *IEEE Transactions on Electron Devices*, vol. ED-32, pp. 1694–1703, Sep 1985.

- [32] K. Murata, "Theoretical studies of the electron scattering effect on developed pattern profiles in x-ray lithography," *Journal of Applied Physics*, vol. 57, pp. 575-580, Jan 1985.
- [33] K. Murata, M. Tanaka, and H. Kawata, "Theoretical study of energy absorption on x-ray lithography with monochromatic x-rays," *Optik*, vol. 84, pp. 163-168, 1990.
- [34] B. D. Henke, J. A. Smith, and D. T. Attwood, "0.1-10-keV x-ray-induced electron emissions from solids—models and secondary electron measurements," *Journal of Applied Physics*, vol. 48, pp. 1852-1866, May 1977.
- [35] D. F. Kyser, "Spatial resolution limits on electron beam nanolithography," *J. Vac. Sci. Technol. B.*, vol. 1, pp. 1391-1397, Oct-Dec 1983.
- [36] N. Tsumita, J. Melngailis, A. M. Hawryluk, and H. I. Smith, "Fabrication of x-ray masks using anisotropic etching of (110) Si and shadowing techniques," *J. Vac. Sci. Technol.*, vol. 19, p. 1211, Nov-Dec 1981.
- [37] S. Y. Chou, H. I. Smith, and D. A. Antoniadis, "X-ray lithography for sub-100nm-channel-length transistors fabricated with conventional photolithography, anisotropic etching, and oblique shadowing," *J. Vac. Sci. Technol. B*, vol. 3, pp. 1587-1589, Nov-Dec 1985.
- [38] "KTI Chemicals, Inc., Sunnyvale, CA 94086,".
- [39] B. L. Henke and M. A. Tester, *Advances in X-ray Analysis*, ch. 18, p. 76. Plenum Press, 1975.
- [40] D. C. Flanders, H. I. Smith, H. W. Lehmann, R. Widmer, and D. C. Shaver, "Surface relief structures with linewidths below 2000Å," *Applied Physics Letters*, vol. 32, pp. 112-114, Jan 1978.
- [41] J. Lingnau, R. Dammel, and J. Theis, "Recent trends in x-ray resists: part I," *Solid State Technology*, pp. 105-112, Sep 1989.
- [42] R. J. Hawryluk, H. I. Smith, A. Soares, and A. M. Hawryluk, "Energy dissipation in a thin polymer film by electron beam scattering: experiment," *Journal of Applied Physics*, vol. 46, pp. 2528-2537, Jun 1975.
- [43] S. E. Bernacki and H. I. Smith, "X-ray lithography applied to silicon device fabrication," in *Proc. Sixth Int. Conf. Electron Ion Beam Sci. Technol.*, (R. Bakish, ed.), 1974.
- [44] M. L. Schattenburg, K. Li, R. T. Shin, J. A. Kong, and H. I. Smith, "Electromagnetic calculation of soft x-ray diffraction from nanometer-scale gold structures,". To be presented at the 35th International Symposium on Electron, Ion, and Photon Beams, May 26-31, 1991, Seattle, WA.

- [45] E. Hundt and P. Tischer, "Influence of photoelectrons on the exposure of resists by x rays," *Journal of Vacuum Science and Technology*, vol. 15, pp. 1009–1011, May/June 1978.
- [46] J. R. Maldonado, G. A. Coquin, D. Maydan, and S. Somekh, "Spurious effects caused by the continuous radiation and ejected electrons in x-ray lithography," *Journal of Vacuum Science and Technology*, vol. 12, pp. 1329–1331, Nov/Dec 1975.
- [47] Y. Saitoh, H. Yoshihara, and I. Wananabe, "Effects of photoelectrons and auger electrons on contrast and resolution in x-ray lithography," *Japanese Journal of Applied Physics Part II*, vol. 21, pp. L52–L54, Jan 1982.
- [48] K. Okada and J. Matsui, "Effects of electrons ejected from the substrate on PGMA negative resist cross-linking in x-ray lithography," *Japanese Journal of Applied Physics Part II*, vol. 22, pp. L810–L812, Dec 1983.
- [49] I. Haller, M. Hatzakis, and R. Srinivasan, "High-resolution positive resists for electron-beam exposure," *IBM Journal of Research and Development*, vol. 12, pp. 251–256, May 1968.
- [50] A. C. Ouano, "Dependence of dissolution rate on processing and molecular parameters of resists," in *Polymers in Electronics*, (T. Davidson, ed.), ACS Symposium Series 242, 1984.
- [51] R. B. Seymour and C. E. Carraher, Jr., *Polymer Chemistry An Introduction*, ch. 9, p. 300. Marcel Dekker, Inc., 1981.
- [52] A. C. Ouano, "A study on the dissolution rate of irradiated poly(methyl methacrylate)," *Polymer Engineering and Science*, vol. 18, pp. 306–313, Mar 1978.
- [53] . SSL Laboratory Procedures, M.I.T.
- [54] J. S. Greeneich, "Solubility rate of poly-(methyl methacrylate), pmma, electron resist," *J. Electrochem. Soc.*, vol. 122, pp. 1669–1671, Dec 1975.
- [55] H. Hiraoka, "Radiation chemistry of poly(methacrylates)," *IBM J. Res. Develop.*, vol. 21, pp. 121–130, Mar 1977.
- [56] . Hoechst Celanese Corporation, Electronic Products Division, Somerville, NJ 08876.
- [57] R. Dammel, K. Dössel, J. Lingnau, J. Theis, H. Huber, H. Oertel, and J. Trube, "Negative-tone high-resolution photocatalytic resist for x-ray lithography," *Microelectronic Engineering*, vol. 9, pp. 575–578, Nov 1989.

- [58] R. Dammel, K. F. Dössel, J. Lingnau, J. Theis, H. L. Huber, and H. Oertel, "Photocatalytic novolak-based positive resist for x-ray lithography – kinetics and simulation," *Microelectronic Engineering*, vol. 6, pp. 503–509, Jun 1987.
- [59] A. Menschig, A. Forchel, R. Dammel, J. Lingnau, U. Scheunemann, J. Theis, and S. Pongratz, "High sensitivity positive tone x-ray resist: Ray-PF-performance under e-beam exposure," *Microelectronic Engineering*, vol. 9, pp. 571–574, Sep 1989.
- [60] S. Pongratz, R. Demmeler, C. Ehrlich, K. Kohlmann, K. Reimer, R. Dammel, W. Hessamer, J. Lingnau, U. Scheunemann, and J. Theis, "E-beam applications of highly sensitive positive and negative-tone resists for x-ray mask making," in *Electron-Beam, X-Ray, and Ion-Beam Technology: Submicron Lithographies VIII*, (A. W. Yanof, ed.), pp. 303–316, 1989. Proc. SPIE 1089.
- [61] J. Lingnau, R. Dammel, and J. Theis, "Recent trends in x-ray resists: part II," *Solid State Technology*, pp. 107–111, Oct 1989.
- [62] R. Dammel, ",". Private Communication.
- [63] R. Ballhorn, R. Dammel, H. H. David, C. Eckes, A. Fricke-Damm, K. Kreuer, G. Pawlowski, and K. Przybilla, "Performance optimization of the chemically amplified resist RAY-PF,". To be published in *Microelectronic Engineering* as part of the Proceedings of the International Conference on Microlithography, *Microcircuit Engineering 90*, Leuven, Belgium, 18-20 September 1990, also the appendix to that paper which may not be included in the published version.
- [64] R. Eisberg and R. Resnick, *Quantum Physics of Atoms, Molecules, Solids, Nuclei, and Particles*, ch. 3, p. 63. John Wiley & Sons, Inc., 1985.
- [65] H. I. Smith, "A model for comparing process latitude in ultraviolet, deep-ultraviolet, and x-ray lithography," *J. Vac. Sci. Technol. B*, vol. 6, p. 346, Jan/Feb 1988.
- [66] H. I. Smith, "Submicron structures technology,". Lecture Notes for Course 6.781, M.I.T., ©Henry I. Smith, 1986.
- [67] W. G. Oldham, "Contrast studies in high-performance projection optics," *IEEE Transactions on Electron Devices*, vol. ED-30, pp. 1474–1479, Nov 1983.
- [68] A. C. Warren, I. Plotnik, E. H. Anderson, M. L. Schatttenburg, and D. A. Antoniadis, "Fabrication of sub-100nm linewidth period structures for study of quantum effects from interference and confinement in Si inversion layers," *Journal of Vacuum Science and Technology B*, vol. 4, pp. 365–368, Jan/Feb 1986.



- [69] A. Moel, M. L. Schattenburg, J. M. Carter, and H. I. Smith, "Microgap control in x-ray nanolithography," *J. Vac. Sci. Technol. B*, vol. 7, pp. 1692-1695, Nov-Dec 1989.
- [70] N. Atoda, H. Kawakatsu, H. Tanino, S. Ichimura, M. Hirata, and K. Hoh, "Diffraction effects on pattern replication with synchrotron radiation," *J. Vac. Soc. Technol. B*, vol. 1, pp. 1267-1270, Oct-Dec 1983.
- [71] H. I. Smith, "A review of submicron lithography," *Superlattices and Microstructures*, vol. 2, no. 2, pp. 129-141, 1986.
- [72] B. J. Lin, "A new perspective on proximity printing: from ultraviolet to x ray," *J. Vac. Sci. Technol. B*, vol. 8, pp. 1539-1546, Nov/Dec 1990.
- [73] J. Z. Y. Guo, G. Chen, V. White, P. Anderson, and F. Cerrina, "Aerial image formation in synchrotron-radiation-based x-ray lithography: the whole picture," *J. Vac. Sci. Technol. B*, vol. 8, pp. 1551-1556, Nov/Dec 1990.
- [74] J. Z. Guo and F. Cerrina, "Comparison of plasma source with synchrotron source in xrl," To be published as part of the proceedings of the SPIE 1991 Symposium on Microlithography, March 8, 1991.
- [75] B. J. Lin, "A comparison of projection and proximity printings - from UV to x-ray," *Microelectronic Engineering*, vol. 11, pp. 137-145, Nov 1989.
- [76] B. J. Lin, "Computer simulation study of images in contact and near-contact printing," *Polymer Engineering and Science*, vol. 14, pp. 498-508, Jul 1974.
- [77] K. Heinrich, H. Betz, and S. Pongratz, "Computer simulations of resist profiles in x-ray lithography," *Journal of Vacuum Science and Technology*, vol. 19, pp. 1254-1258, Nov/Dec 1981.
- [78] H. Betz, K. Heinrich, K. Heuberger, H. Huber, and H. Oertel, "Resolution limits in x-ray lithography calculated by means of x-ray lithography simulator XMAS," *Journal of Vacuum Science and Technology*, vol. B4, pp. 248-252, Jan/Feb 1986.
- [79] J. W. Goodman, *Introduction to Fourier Optics*, ch. 3, pp. 30-56. McGraw-Hill, 1968.
- [80] J. A. Ratcliffe, "Some aspects of diffraction theory and their application to the ionosphere," in *Reports on Progress, Vol. XIX*, (A. C. Strickland, ed.), The Physical Society, London, 1956.
- [81] S. Silver, "Microwave aperture antennas and diffraction theory," *Journal of the Optical Society of America*, vol. 52, pp. 131-139, Feb 1962.

- [82] K. Siegbahn, "Electron spectroscopy for atoms, molecules, and condensed matter," *Reviews of Modern Physics*, vol. 54, pp. 709–728, Jul 1982.
- [83] K. Siegbahn, C. Nordling, A. Fahlman, R. Nordberg, K. Hamrin, J. Hedman, G. Johansson, T. Bergmark, S. Karlsson, I. Lindgren, and B. Lindberg, "ESCA atomic, molecular and solid state structure studied by means of electron spectroscopy," *Nova Acta Regiae Societatis Scientiarum Upsaliensis*, vol. IV, no. 20, pp. 38–39, 1967. Presented to the Royal Society of Sciences of Uppsala, Dec. 3, 1965.
- [84] J. W. Goodman, *Statistical Optics*, ch. 5, pp. 157–229. John Wiley & Sons, 1985.
- [85] E. P. Bertin, *Principles and Practices of X-Ray Spectrometric Analysis*, ch. 1, p. 30. Plenum Press, 1975.
- [86] J. A. Bearden, "X-ray wavelengths," *Reviews of Modern Physics*, vol. 39, pp. 78–124, Jan 1967.
- [87] W. H. Press, B. P. Flannery, S. A. Teukolsky, and W. T. Vetterling, *Numerical Recipes in C*, ch. 12, pp. 398–467. Cambridge University Press, 1988.
- [88] Y. Ku, E. H. Anderson, M. L. Shattenburg, and H. I. Smith, "Use of a pi-phase shifting x-ray mask to increase the intensity slope at feature edges," *Journal of Vacuum Science Technology B*, vol. 6, pp. 150–153, Jan/Feb 1988.
- [89] A. Moel, W. Chu, K. Early, E. E. Moon, M. L. Schattenburg, J. M. Bauer, F. Tsai, F. W. Griffith, L. E. Haas, C. D. Fung, and H. I. Smith, "Fabrication and characterization of high-flatness mesa-etched silicon nitride x-ray masks," To be presented at the 35th International Symposium on Electron, Ion, and Photon Beams, May 26-31, 1991, Seattle, WA.
- [90] R. M. A. Azzam and N. M. Bashara, *Ellipsometry and Polarized Light*, ch. 4, pp. 283–288. North-Holland, 1977.
- [91] G. E. Rittenhouse, "A three-terminal quantum well superconducting transistor," PhD Thesis Proposal, submitted Sept, 1990.
- [92] G. E. Rittenhouse, K. Early, and J. Graybeal, "A novel structure for a three-terminal superconducting resonant tunneling device," *Bulletin of the American Physical Society*, vol. 36, p. 1025, Mar 1991. Presented at APS meeting, Cincinnati, Ohio, 18-22 Mar. 1991.
- [93] D. L. Kendall, "A new theory for the anisotropic etching of silicon and some underdeveloped chemical micromachining concepts," *J. Vac. Sci. Technol. A*, vol. 8, pp. 3598–3605, Jul/Aug 1990.

- [94] D. L. Kendall, "On etching very narrow grooves in silicon," *Applied Physics Letters*, vol. 26, pp. 195–198, Feb 1975.
- [95] R. L. Smith, "The potential dependence of silicon anisotropic etching in KOH at 60°C," *J. Electroanal. Chem.*, vol. 238, pp. 103–113, 1987.
- [96] B. Kloeck, S. D. Collins, N. F. De Rooij, and R. L. Smith, "Study of electrochemical etch-stop for high-precision thickness control of silicon membranes," *IEEE Transactions on Electron Devices*, vol. 36, pp. 663–669, Apr 1989.
- [97] H. Seidel, L. Crepregi, A. Heuberger, and H. Baumgärtel, "Anisotropic etching of crystalline silicon in alkaline solutions," *J. Electrochemical Soc.*, vol. 137, pp. 3612–3626, Nov 1990.